AN EVALUATION OF THE SUBSTRATE EFFECT ON THE PERFORMANCE OF
YSZ EB-PVD THERMAL BARRIER COATINGS

by

Igor Steven Garcia

BS, University of Rhode Island, 2001

Submitted to the Graduate Faculty of

School of Engineering in partial fulfillment

of the requirements for the degree of

Master of Science

University of Pittsburgh

2004

UNIVERSITY OF PITTSBURGH

SCHOOL OF ENGINEERING

This thesis was presented

by

Igor Steven Garcia

It was defended on

July 20, 2004

and approved by

John A. Barnard, Department Chair and Professor, Material Science and Engineering
Department

William A. Soffa, Professor, Material Science and Engineering Department

Thesis Co-Advisor: Frederick S. Pettit, Professor, Material Science and Engineering
Department

Thesis Co-Advisor: Gerald H. Merier, Professor, Material Science and Engineering
Department

AN EVALUATION OF THE SUBSTRATE EFFECT ON THE PERFORMANCE OF
YSZ EB-PVD THERMAL BARRIER COATINGS

Igor Steven Garcia, M.S.

University of Pittsburgh, 2004

The cyclic oxidation failure of thermal barrier coatings on eight different nickel

base superalloys was studied. Substrates include six third generation superalloys, one

second generation superalloy, and the alloy IN738. The thermal barrier coatings include

yttria stabilized zirconia (YSZ) deposited by electron beam physical vapor deposition

(EB-PVD), a (Ni,Pt) Al underlayer deposited by chemical vapor deposition (CVD) and

grit blasted to provide a rough surface. The study conducted included the cyclic exposure

of the specimens between 1100 ºC and room temperature. During the cyclic heat

exposure, a thermally grown oxide (TGO) grew. After failure, the specimens were

categorized according to the number of cycles obtained before failure. Later, specimens

were examined by macroscopic and microscopic methods and chemical analysis was

obtained by energy dispersive spectrometry (EDS). All specimens failed by ratcheting

along the YSZ/TGO interface showing little or no effect of the substrate compositions.

Nevertheless, large differences in the cyclic lives existed among the third generation

superalloys and between third and second generation superalloys, and single crystal vs.

polycrystalline superalloys. Phase transformations were observed in the bond coat.

Substrate elements such as Ta, Cr, and Co appear to play a role in the transformation of

these phases. Bond coat deformation is attributed to the phase transformation, and the

bond coat phase properties are attributed to chemical content. Carbon and tantalum play

a role in the cyclic failure of the specimens.

TABLE OF CONTENTS

LIST OF TABLES

LIST OF FIGURES

xiii

1.0   INTRODUCTION

Nickel-base superalloys have been the materials of choice in a power driven society such as ours for decades now. Nevertheless, numerous attempts are made continually in order to improve these already superb alloys and to take them to a different level of performance never before seen. The nickel alloy began as a substitute for cobalt alloys in a cobalt deficient era, to completely replace these cobalt alloys. Wrought nickel alloys served the purpose for a good while until more challenging environments emerged. The invention of vacuum melting and solidification was a great step, followed by directional solidification, which yielded both columnar and single crystal superalloys. Today, single crystals are the main type of alloys, and even these are categorized into different generations; hence delineating a distinction from each other. For the most severe conditions, polycrystalline alloys also have numerous applications in other sections of the turbine.

These distinctions in nickel-base superalloys stem mainly from their melting temperatures, solidus temperatures, and alloy compositions. Today most of these alloys can perform at temperatures close to 1100 ºC. It is on the technology of such

compositions that the world relies to fly hundreds of passengers from London to Monroevia, or to produce enough energy to light up the great city of New York.

However, deleterious environments have always posed a great problem to superalloys, mainly oxidation and corrosion. Thermal barrier coatings emerged in the 50s as frit enamels as an answer to these deleterious environments for the oxidation problem of metals. Today, the thermal barrier coating is a complex system which consists of four different layers and can decrease the temperature of the load bearing substrate by as much as 200ºC. Figure 1.1 is a schematic diagram of the nickel superalloy specimens coated with the thermal barrier coatings. The first layer is a low thermal conductive layer usually Yttria Stabilized Zirconia (YSZ). The second layer is the thermally grown oxide; a layer that grows as a result of the high temperatures and selective oxidation of particular metals and serves as the protective layer to the substrate from oxidation and/or hot corrosion. The third layer is called a bond coat and is responsible for maintaining a steady supply of the metal to be selectively oxidized. The fourth layer is the substrate. Nevertheless, numerous problems exist which range from the manufacturing process of this film to the interaction between the substrate and films. Such problems include the adherence of the YSZ, the depletion of the element to be selectively oxidized, the adherence of the oxide layer to the bond coat, the effect of substrate elements on either of the films, etc. As a result, more studies need to be conducted that explain the behavior of this film in relation to substrates.
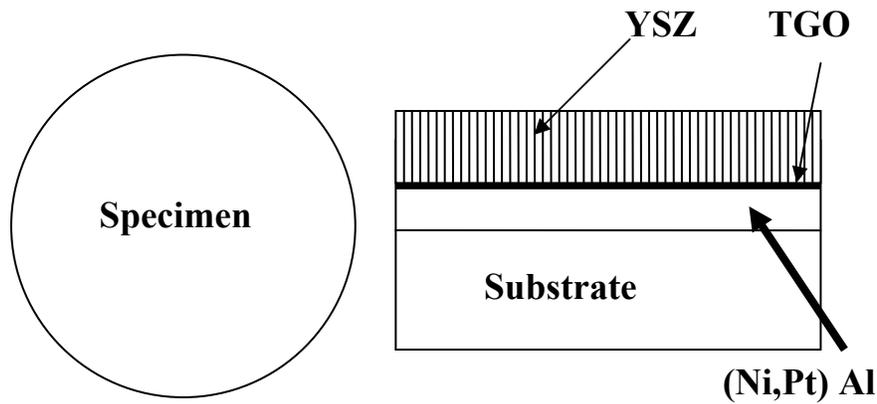
Figure 1.1 Diagram of Ni superalloy with (Ni, Pt) Al bond coat with EB-PVD YSZ.

It is well known that the efficiency of an engine system is directly related to its heating and cooling temperatures. It is also widely acknowledged that the efficiency of a thermal system is proportional to its inlet temperature; such is the case for a jet engine and power generator. Therefore, in agreement with thermodynamics, the efficiency of a jet engine and a power generator can be increased if the difference between its inlet and outlet temperatures can increase. Nevertheless, in this attempt of increasing efficiency of a system, the stability of the system must also be kept in mind. Hence, a synergistic criteria for the design of a system must be related to the cost, durability, efficiency, and ergonomics of a system, with and in its environment.

High temperature applications where metals perform at 0.8-0.9 of their Tm, must maintain a stable phase without much change of their mechanical and physical properties. In addition to maintaining a stable phase, it is also understood that such materials in such environments have a very high propensity to oxidize and corrode. Therefore, any

solution that is sought in order to improve the development of these materials must conform to the problems hereby mentioned.

The following study relates the qualitative performance of a thermal barrier coating deposited onto six different third generation nickel-base superalloys and compared to a second generation and a polycrystalline nickel-base superalloy. The thermal barrier coating system consists of an Yttria Stabilized Zirconia top layer fabricated by EB-PVD, supported by a heavy grit blasted (Ni,Pt) Al bond coat layer. The specimens underwent cyclic thermal exposure until failure occurred and were then examined using macroscopic and microscopic observations as well as energy dispersive spectrometry for topographical and chemical analysis. In the following, a theoretical background will be presented, followed by classification of the specimens into three categories based on the number of cycles reached until failure. Results are presented along with a discussion and conclusions stemming from these results.

2.0   BOND COAT

2.1   BRIEF HISTORY TO MODERN APPLICATIONS

In 1974 Bungardt et al. [1] working on behalf of Deutsche Edelstahlwerke AG received a patent for a protective diffusion layer on Ni and/or Co based alloys. He presented a basic work where aluminide coatings were proved to be simply inferior to aluminide coatings with diffused platinum metals. Moreover, he also stated that such coatings are also improved by the addition of palladium, and rhuthenium. The research also indicated that as the precious metal layer thickness increased, so did the life of the coated component. Since then, numerous studies have been conducted about Pt-Al and variations of the type.

2.2   FUNCTION, COMPOSITION, AND BEHAVIOR

In order to protect the underlying substrate from deleterious environments at elevated temperatures, meaning oxidation and/or hot corrosion, the bond coat forms a

protective layer atop of itself. These can be categorized into chromia or alumina formers. The following study is based on the formation of alumina. This protective layer, also known as a thermally grown oxide (TGO), is the product of selective oxidation of aluminum from the bond coat. Moreover, it provides a suitable surface for the top ceramic layer.

Bond coats normally contain elements that are found in the substrate matrix including an element with a high affinity for oxygen, which forms the oxide protective layer. Nevertheless, due to the potential of many metals to oxidize, internal oxidation of other elements within the bond coat, besides the preferred oxidizing element, can prevent the formation of a uniform protective layer and hence deprive the substrate from the environmental protection that is required. Some of today's most prominent bond coats include, MCrAlY (M for Ni, Co or both), nickel aluminide, and platinum modified nickel aluminide bond coats.

The effect of the Pt modified NiAl bond coats hold the main interest in this study and shall be addressed from here forth. At the same time, there will be an attempt to elucidate qualitatively some of the properties of this (Ni, Pt) Al bond coat with respect to the mechanical properties and thermodynamics.

The initial crystal structure of the (Ni, Pt) Al bond coat is a β phase B2 (CsCl) crystal structure. Nevertheless, as the outward diffusion of Al occurs during the growth of the selective oxide (Al_2O_3), along with inward diffusion of aluminum into the substrate, depletion of the aluminum from the bond coat layer is inevitable. This depletion of aluminum, occurring during exposure of the system, can cause the bond coat to oscillate between the β (CsCl) B2 phase and the β' (fct) $L1_0$ (martensitic) phase and

eventually to the γ' ($L1_2$) phase [2]. As a result of these phase transformations, significant changes occur not only to the volume of the bond coat, but also, changes in the mechanical properties and physical properties of the system, such as yield strength and the coefficient of thermal expansion [3] (See Table 2.2.1). Chen et al. noted a sizable volume change of 2.0±0.3% between the B2 and $L1_0$ structures. These conditions affect the adhesion and performance of the TBC systems. Karlsson [4] studied the effects of the martensitic phase transformations of the bond coat in a system with undulations with and without growth strain from an oxide layer. The study deduced that the ongoing phase transformation does not cause failure by itself in a TBC system. The study alluded to out of plane stresses and to strain from oxide growth as the responsible factors to increase the amplitude of an undulation and initiate cracks that create failure.

Table 2.1 Table of some physical and mechanical properties for thermal barrier coating systems.

Name	CTE α [$^{\circ}$C^{-1}]	Yield Strength [MPa]
Martensite $L1_0$	11.3×10^{-6}	500↑@ T < T_T[7]
β-B2 CsCl	12.4×10^{-6}	25 ↓@ T > T_T [7]
γ'-$L1_2$	16.9×10^{-6}	100-500 @ 100<T<900
TBC (Y_2O_3-ZrO_2)	$\sim 11\text{-}13 \times 10^{-6}$	0-100 [8]
Al_2O_3	$8\text{-}9 \times 10^{-6}$[8]	380 [8]

Furthermore, in the case of superalloys, significant attention must be paid to the active elements of the system. In many cases, it is observed that some of these alloying

elements have a tendency to diffuse outward, or segregate to preferred locations. For

situations where the alloying elements diffuse to the bond coat from the substrate, it is

possible that the properties of a martensitic prone bond coat change [5]. Kainuma et al.

[6] studied the martensitic transformation of NiAl alloys and the effect of a component X

on the transformation. The study determined that the martensitic transformation

properties can be changed with element composition, particularly M_s and A_f.

2.3 MANUFACTURING PROCESS

Some modern manufacturing processes of the bond coats include, air plasma

spray, low pressure plasma spray and chemical vapor deposition. Of interest in this case

is the chemical vapor deposition [9, 5]. For the application of a (Ni,Pt)Al bond coat, Pt is

deposited on the surface of the substrate via an electroplating process. Afterwards $AlCl_3$,

an aluminum halide, is introduced as a low activity gas into a chamber where the

specimen is to be coated internally and/or externally (see Figure 2.1). A heat treatment

follows at temperatures in the range of 1050-1100 $^{\circ}$C to homogenize the bond coat and

produce a single phase.

Figure 2.1 Diagram of a Low Activity Aluminizing system for Chemical Vapor Deposition

Surface treatments can also be applied prior to YSZ deposition to improve adhesion and remove impurities [10]. For example, grit blasting of the surfaces of as processed bond coats have been seen to change the performance of thermal barrier coating systems [11].

3.0 THERMALLY GROWN OXIDE

3.1 BRIEF HISTORY

Early development of alloys to protect against corrosion and oxidation utilized Cr_2O_3 formers. However, the need for alloys and more stable coatings in more corrosive environments, mainly higher temperatures, required the development of new alloys. The applications became more extreme as the temperatures rose, and the development of alloys began to shift towards alumina formers. Aluminum not only added creep strength to the alloys by forming γ' precipitates, but it also formed a more stable oxide. Although alumina formers presented a good solution to the oxidation problem, some obstacles remained, e.g. finding a critical Al content that maintained the continuous growth after spallation of the scale. Coatings that provided a large supply of metal to the protective scale appeared on the scene in the 70s; since then, the industry has introduced different types of coatings and processes used to deposit them. Moreover, the performance of these alloys has also improved. Figure 3.1 displays the evolution of protective coatings, it shows the evolution of oxidation of alloys and coatings for superalloys.
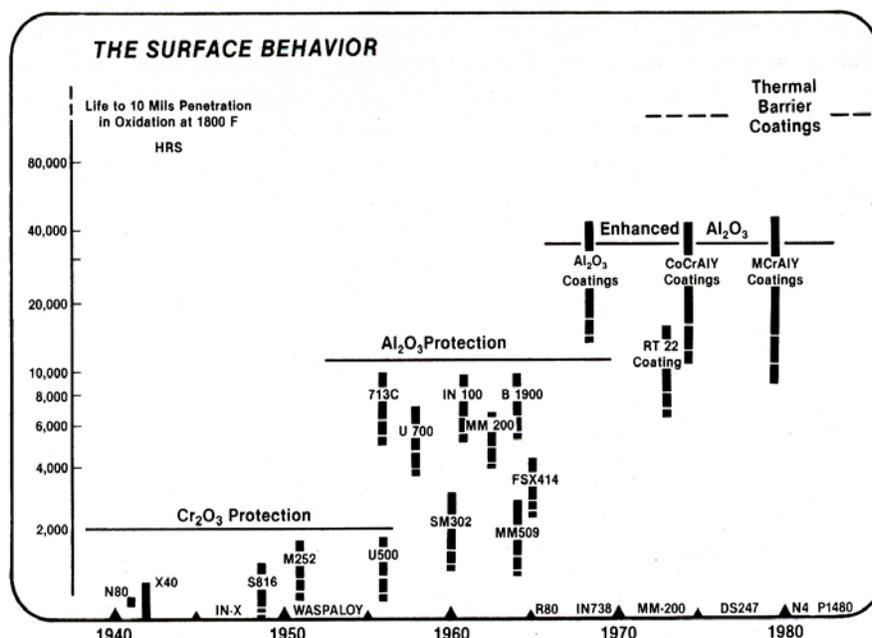
Figure 3.1 Progress of thermally grown protective oxide films. [12]

3.2 GROWTH AND STRESSES

Before continuing this explanation on the growth of an alumina layer, other comments may emphasize the complexity of this subject. Acknowledging that selective oxidation does take place, it must also be stated that successful oxidation of aluminum includes the formation of an external film and not internal. Hence internal oxidation would only mean that the substrate does not have the required composition to maintain the continuous growth of an external protective layer. In a recently written book not yet published by Prof. G. H. Meier at the University of Pittsburgh[1], he details two different

---

[1] Class hand outs for MSE 2050- Gas-Metal Reactions course taught by Professor Gerald H. Meier.

criteria for achieving a success at external protective layers. The first criterion details the solute content to establish external oxidation growth rather than internal oxidation,

$$N_B^{(O)} > \left[\frac{\pi g^*}{2\nu} N_O^{(S)} \frac{D_O V_M}{D_B V_{OX}} \right]^{\frac{1}{2}}$$

here $N_B^{(O)}$ refers to the solute concentration needed, D_o is the oxygen diffusivity, D_B the diffusivity of the solute, V_M is the molar volume of the solvent metal, υ moles of oxygen necessary to form the oxide, V_{OX} is the molar volume of the oxide film, $N_O^{(S)}$ the oxygen molar content. The second criterion, refers to maintaining growth of an external scale and is

$$N_B^{(o)} = \frac{V_m}{32\nu} \left(\frac{\pi K_p}{D_B} \right)^{\frac{1}{2}}$$

here Kp is the growth rate constant of an oxide scale.

Alumina grows by the inward diffusion of oxygen through the oxide scale to react with the aluminum. A slow growth rate of this layer can represent characteristics of a durable system, and is preferred in high temperature applications. There are various polymorphs to this oxidation reaction, including its stable phase of interest α-Al_2O_3. The other polymorphs of aluminum oxide include θ-Al_2O_3, κ-Al_2O_3, γ-Al_2O_3, and δ-Al_2O_3. The reaction follows as,

$$2Al + \frac{3}{2}O_2 \Rightarrow Al_2O_3$$
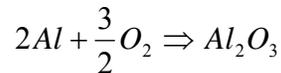
Several studies have determined the importance of the thermally grown oxides in the thermal barrier coating systems. Initial importance is focused on the residual stresses, a product of the coefficient of thermal expansion mismatches between the oxide

scale/bond coat layer, and oxide/YSZ top coat, which occurs as a result of cool downs from elevated temperatures to room temperature. As a result of these residual stresses, a high stress concentration interface can be formed to produce compression of the TGO which can lead to the failure of the TBC system [13, 14]. The failure produces spallation of the TGO along with the YSZ ceramic layer.

Other sorts of stresses that can act in the TBC system pertaining to the thermally grown oxide include growth stresses. Although previously believed to be of smaller magnitude than residual stresses, growth stresses have been found to be of equal magnitude as thermal stresses, but also to be among the driving forces in the deformation of bond coats with a deformed surface that undergoes a phase transformation and fail by ratcheting [4,14, 15, 16]. In systems with deformed bond coats, separation of the YSZ and the TGO scale can occur due to an increment of out-of-plane stresses [14], an active result derived from both thermal and growth stresses.

3.3 EFFECT OF REACTIVE, REFRACTORY AND PRECIOUS METALS

The effect of reactive and precious elements has also been among the main foci in the development of bond coats that may enhance the thermally grown oxide performance in thermal barrier coating systems [17]. Substrate composition has been cited as a factor in the adhesion and growth rate of the thermally grown oxide [17]. The effect of Y on the performance of alumina in NiCrAl alloys has been found to improve the α-Al_2O_3

adherence [18]. Due to the diffusion gradient produced at elevated temperatures as well as the oxidation potential of metals, some substrate elements diffuse outward to the bond coat, and bond coat-oxide interface.

Not enough has been done in the field to understand the effects of refractory metals on the performance of oxidation. Pettit and Meier [19] studied the effect of refractory metals not only on the oxidation of metals but also in the hot corrosion area. They found that though some positive effects can be seen with the presence of refractory metals such as Ta, Ti, Nb, W, Mo, etc., most of the effects are deleterious to the selective oxidation of Al_2O_3 and Cr_2O_3.

4.0   YSZ TOP COAT

4.1   BRIEF HISTORY

Frit enamels, a vitreous, non-organic material, constituted during the 1950s the initial stages of the industry that would grow to incorporate Y_2O_3-ZrO_2 as the leading insulating coating in high temperature corrosion applications. The evolution process prior to the YSZ included alumina, zirconia-calcia and zirconia-magnesia, all of which failed due to destabilization of the TBC at elevated temperatures. Eventually the process of evolution included the high Yttria concentration ceramic coating that contained between 12-20 Y_2O_3 wt%, and showed significant improvement. Yttria worked as a stabilizer for the Zirconia top coat which changes phase from a tetragonal to a monoclinic phase at elevated temperatures. By 1978, Stephen Stecura presented his work on the improved performance of the YSZ by lowering the Yttria content to between 6-8 wt%. Since then, the latter composition is standard for modern applications. For more information on the history of thermal barrier coatings, see Miller, R.A. [20].

4.2 ROLE OF THE YTTRIA STABILIZED ZIRCONIA

The YSZ functions as an insulating top coat with its low thermal conductivity to reduce the temperature of the supporting substrate and hence improve the all around efficiency of a system at elevated temperatures. Temperatures between the load bearing substrate and the ceramic top coat can differ between 100 ºC and 200 ºC. Since the efficiency of an engine is directly proportional to the change in temperature it undergoes and/or the durability of the components in a working system; the YSZ plays a key role in this technology to reduce the temperature of the alloy during operation.

4.3 MANUFACTURING PROCESSES AND PROPERTIES

There are two main processes to manufacture the ceramic top coat or YSZ; these are **e**lectron **b**eam **p**hysical **v**apor **d**eposition (**EB-PVD**) and the **p**lasma **s**pray (**PS**). Brief descriptions of both of these processes shall follow in the sub-sections. Of the two processes, EB-PVD is of interest in this research project. Besides mechanical properties, production costs are also a concern when selecting among the two top coatings for a given application. Plasma spray emerged first in the early 1960s as the leading coating process for high temperature applications. On the other hand, EB-PVD emerged during the 1970s. Though both manufacturing processes are widely used today, the plasma spray process is economically cheaper though given that a tradeoff does exist in the mechanical properties. On the other hand, the EB-PVD coating shows a higher coefficient of thermal conductivity but shows better strain resistance. Moreover it ought

to be noted, that the process of low pressure plasma spray and EB-PVD are also used to deposit bond coats, e.g. MCrAlY for M being Ni or Co.

4.3.1   Plasma Spray

Two main derivatives exist to the plasma spray process, a low pressure (LPPS) normally used for reactive materials, and an atmospheric air (APS) process. Strangman [21] indicates a 10-15% porosity and microcracks accommodation in the layer to improve strain impairments to prevent delamination. At the same time, these defects reduce the elastic modulus from 154 GPa to between 7-35 GPa.

The process is applied by means of a heated inert plasma gas that melts a fine powder in a gun and then coats the objective with molten materials [22, 23, 24]. The plasma may be a composition of argon with another noble gas such as He, or simply molecular gases such as H_2, O_2, N_2, etc. Figure 4.1 and Figure 4.2 display a concept mechanism for the plasma spray manufacturing process. Although all components are of importance in the design of the system, there will be an accentuation on some. As noted, the system is water cooled to maintain thermal stability of the system. The tungsten cathode heats up the noble or molecular gases that eventually melt the soon to be coated material. There are two powder feeds to the system; an internal and an external feed. There is also the gas injection feed noted as in the diagram as the Arc Gas Tangential/Injection. The gas temperatures go as high as 3000 K to melt and spray the material. Impact velocities between the coated surface and the gun range between 100-650 m s^{-1}. Another important factor, the cooling rate, ranges between 10^7-10^8 K s^{-1}[25]. Figure 4.3 displays a rotational rack with samples to be coated. A magnification on the

right side of the diagram manages to show how layers of deposition create pores that enhance strain tolerance. In addition, it should also be noted that even though not visual on the diagram, this technique profits from being applied on a rough surface for mechanical interlocking. Moreover, it is also applied in layers, hence achieving the porous structure.
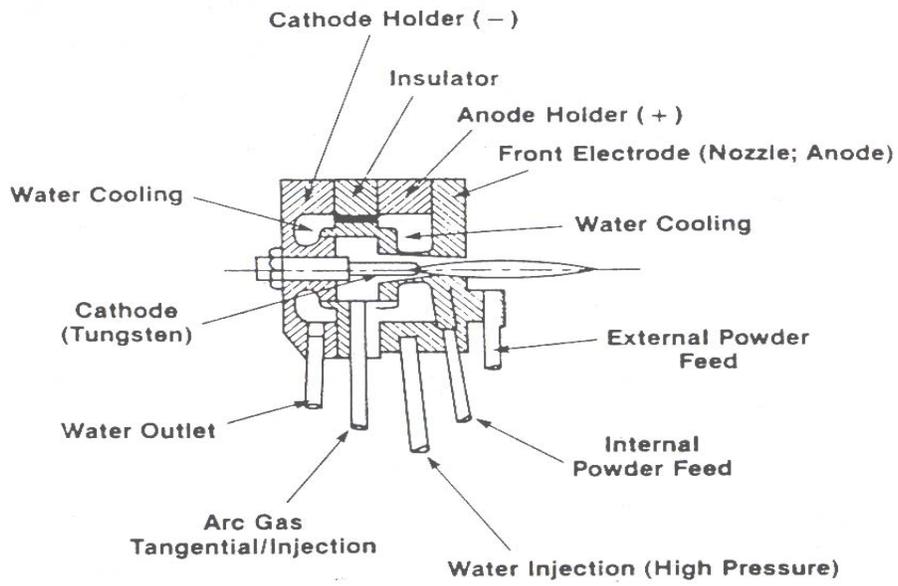
Figure 4.1 Diagram of a plasma spray gun mechanism used for coating of metallic substrates with YSZ or MCrAl bond coats.
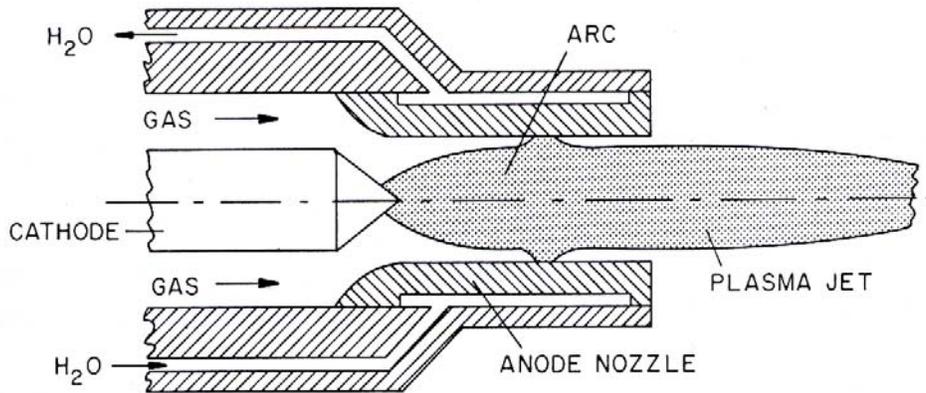
Figure 4.2 Diagram of the plasma spray torch.
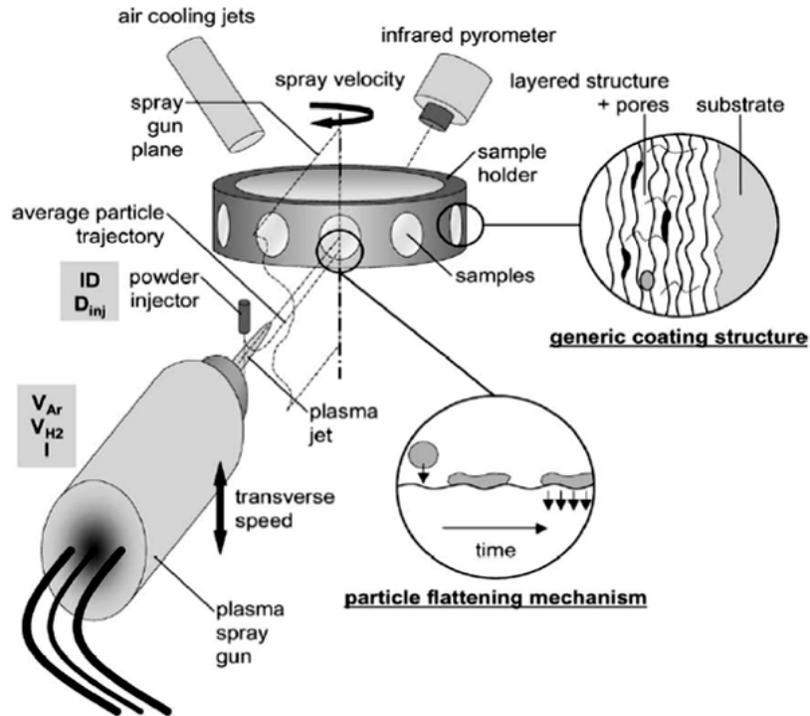
Figure 4.3 Diagram of a plasma coating process for multiple specimens.

4.3.1.1 Failure Mechanisms of PS TBCs

Failure mechanisms in plasma sprayed top coats with metallic under layers which may well be applied using the same technique occur at various levels. Padture et al. [24] noted that stress concentrations led to three types of failures, (i) bond coat/TGO separation, (ii) cracking within the top coat, (iii) linkage of the microcracks by fracture of the TGO.

4.3.2 Electron Beam Physical Vapor Deposition

EB-PVD was used in the 60's for metallic coatings. See Figure 4.4 displaying a schematic representation of the electron beam physical vapor deposition process. The

process is conducted in a vacuum chamber environment with pressures in the ranges of 10^{-4}-10^{-6} Torr. An ingot rod is melted by an electron beam powered by as little as 60 kW and as much as 200 kW. The melt is superheated to create a vapor cloud as the ingot of YSZ material continuously feeds the system [25, 26]. In order to maintain a balanced stoichiometry of the composition, oxygen is fed into the chamber during deposition. Prior to the component being introduced into the coating chamber, the component is cleansed and heated to around 1000 °C; this increases adhesion between the coating and the bond coat layer.
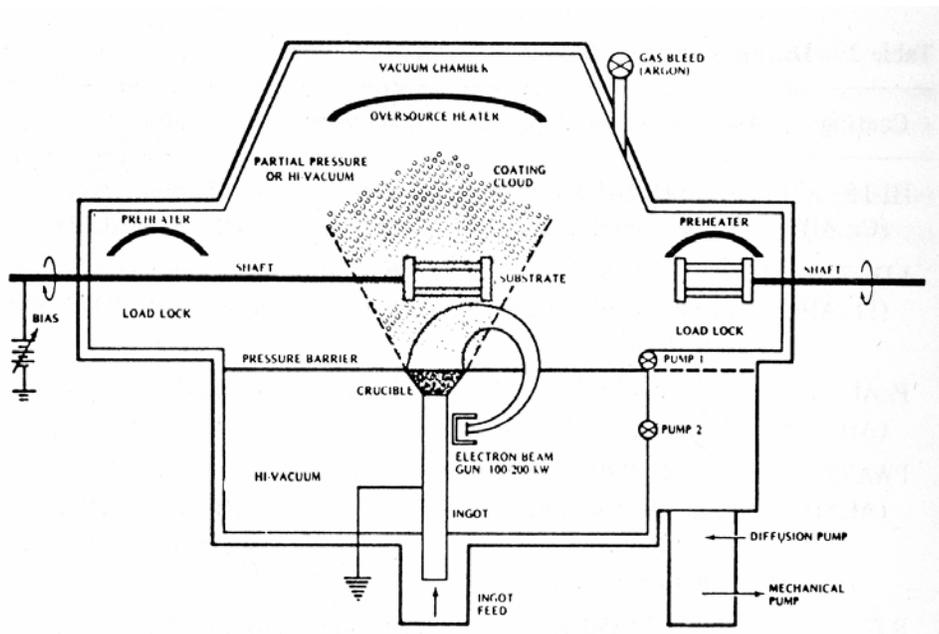
Figure 4.4 Schematic representation of an electron beam physical vapor depostion system.

The electron beam physical vapor deposition process was used in response to residual stresses on plasma sprayed YSZ. Nevertheless there is a tradeoff in some of its physical properties such as thermal conductivity, where this structure has a higher thermal conductivity than the plasma sprayed coatings. Unlike its predecessor, the EB-

PVD process forms columnar grains and in-between gaps called "leaders" that add strain tolerance during thermal cyclic exposures.

4.3.2.1 Failure Mechanisms in the EB-PVD System

Failure of the yttria stabilized zirconia coating fabricated under this process consists of spallation of the system that is detachment of the coating from its original protective area. This can occur by a couple of factors; first, a failure along the YSZ/TGO interface which allows the YSZ film to free itself. The second form of failure would consist of the delamination of the TGO from the bond coat, hence loss of both the TGO and the YSZ films at one time. These processes of delamination are all affected by some of the aforementioned stresses that occur as a result to the TGO residual stresses or growth stresses. Therefore, the coefficient of thermal expansion pertaining to the YSZ film is as important a factor as the coefficient of thermal conductivity in the performance of these protective films. Other defects in the coating that compromise the performance of these films include zero contact planes, and cracks coalescence, etc.

5.0 PROJECT OBJECTIVE

The continuous use of nickel superalloys in turbines for the aerospace, and power generation industry requires a good understanding of how these superalloys might behave under a given condition. Additionally, these superalloys inherit numerous configurations that can affect their performance. The configurations being referred to are substrate compositions and type of solidification such as single crystals, polycrystalline, or columnar grains. Moreover, it is well understood that the performance of nickel superalloys is improved by thermal barrier coatings. The thermal barrier coating as already noted is a system consisting of three layers, a ceramic insulating top coat, followed by a thermally grown oxide, and last the bond coat. For years now, these two systems of nickel superalloys and thermal barrier coatings have been used together in applications requiring oxidation resistance and corrosion resistance at elevated temperatures. Nevertheless, both of these systems continue to evolve. This evolution refers to substrate composition and for thermal barrier coatings composition as well as fabrication processes.

The objective of this study is to find out how the substrate composition of third generation, second generation and a polycrystalline nickel superalloys affect the performance of a Yttria Stabilized Zirconia thermal barrier coating system with a grit

blasted, platinum modified nickel aluminide bond coat at elevated temperatures in an oxidative environment. This study should yield qualitative information about whether or not substrate composition plays a big role in the failure of thermal barrier coatings in an oxidative environment at elevated temperatures. If substrate composition fails to play a significant role in the failure of these thermal barrier coating systems, then the primary failure mechanism should be identified along with cause leading to this type of failure.

The method used to identify the cause of failure of this system include scanning electron microscopy, energy dispersive spectrometry and optical microscopy. Data will be tabulated using EXCEL XP and MatLab.

6.0 EXPERIMENTAL PROCEDURE

The experiment consisted of depositing a thermal barrier coating on six code-named, single crystal, generation three nickel base superalloys, on a generation two single crystal, and on a polycrystalline alloy (See Table 6.1). Prior to depositing the ceramic top coat, specimens were coated with a (Ni,Pt) Al bond coat via CVD and grit blasted to produce a rough surface. During the application of the ceramic top coat, the specimens developed a thin oxide scale between the YSZ and the bond coat.

The specimens were cycled in a vertical furnace at 1100 $^{\circ}$C until failure of the thermal barrier coating occurred. The observations of the specimens are divided as follows: as processed surfaces, as processed cross sections, failed interface surfaces, and observation of failed cross sections. The methods of observation included macroscopic and microscopic, as well as chemical analysis using energy dispersive spectrometry. Microscopic observations were performed using a Philips Scanning Electron Microscope FEG (Field Emission Gun) XL30. There were four specimens to test for each substrate type to determine the reproducibility of the tests, with the exception of René N5 for which only two coupons were available. Failure was identified as any visible disruption of the coating after completion of a furnace period; e.g. spallation of the coating, a buckling of the coating. These code named superalloys are classified by using a set of

letters and numbers, main effect superalloys (ME) and the carbon effect superalloys (CE) as seen in [27]. Compositional content distinguishes the superalloys from one another to classify them among third generation superalloys and compared to second generation and polycrystalline superalloys in the experiment. An additional table displays the solidus and liquidus temperatures of these alloys (see Table 6.2). The code-named substrates assimilate René N5, a second generation superalloy, and differ from the latter in the variations that exist in the wt% range amounts of refractory and reactive elements within them. Table 5.3 shows the amount of moles that exist in these alloys for the most stable carbide formers, which are hafnium and tantalum. As seen in table 6.3, there are a number of superalloys that do not contain any carbon, hence carbide formation is not seen in these substrates.

Table 6.1 Wt.% Composition of third generation superalloys along with IN738 (polycrystalline) and René N5 (second generation).

Material	C	B	Zr	Nb	Al	Ta	Ti	Hf	W	Re	Mo	Cr	Co	Ni
ME-2	0.00	0.00	0.00	0.00	6.70	6.10	0.00	0.14	2.30	4.60	1.50	7.00	7.50	Bal.
ME-13	0.13	0.00	0.00	0.00	4.60	6.20	0.00	0.14	2.40	4.70	1.50	7.00	7.50	Bal.
CE-1	0.00	0.00	0.00	0.00	5.60	8.40	0.00	0.00	4.50	2.80	1.50	7.00	7.50	Bal.
CE-3	0.00	0.00	0.00	0.00	5.80	4.00	0.00	0.28	4.60	2.90	1.50	7.00	7.50	Bal.
CE-6	0.14	0.00	0.00	0.00	5.80	4.00	0.00	0.00	4.80	3.00	1.50	7.00	7.50	Bal.
CE-8	0.12	0.00	0.00	0.00	5.40	8.40	0.00	0.26	4.50	2.90	1.50	7.00	7.50	Bal.
N5	0.00	0.00	0.00	0.00	7.50	6.50	0.00	0.10	6.00	3.00	1.00	7.00	7.50	Bal.
IN738	0.11	0.001	0.050	0.900	3.40	1.70	3.40	0.00	2.60	0.00	7.10	16.00	8.50	Bal.

Table 6.2 Solidus and liquidus temperatures pertaining to the third generation nickel-base superalloys. [27]

Alloy	T(Solidus) °C	T(Liquidus) °C
CE1	1369	1402
CE3	1381	1416
CE6	1370	1410
CE8	1364	1393
ME2	1333	1397
ME13	1378	1416

Table 6.3 Content of moles for most stable carbide formers in the nickel superalloys.

Material	Tantalum	Hafnium	Carbon
ME-2	3.37E-02	7.84E-04	0.00E+00
ME-13	3.43E-02	7.84E-04	1.08E-02
CE-1	4.64E-02	0.00E+00	0.00E+00
CE-3	2.21E-02	1.57E-03	0.00E+00
CE-6	2.21E-02	0.00E+00	1.15E-02
CE-8	4.64E-02	1.46E-03	9.74E-03
N5	3.59E-02	5.60E-04	0.00E+00
IN738	9.39E-03	0.00E+00	9.00E-03

The complete study included thirty seven coupons; five coupons for each of the third generation superalloys, five for IN738 (polycrystalline) and two for René N5 (generation 2). These as processed coupons can be seen on Figure 6.1. It is possible to view that some spallation of the thermal barrier coating did occur prior to the start of thermal cycles. This can be seen for CE6-TBC2, CE6-TBC7, and ME13-TBC2.

CE1-TBC2	**CE1-TBC3**	**CE1-TBC4**	**CE1-TBC5**	**CE1-TBC6**
CE3-TBC1	**CE3-TBC3**	**CE3-TBC5**	**CE3-TBC6**	**CE3-TBC7**
CE6-TBC1	*CE6-TBC2*	**CE6-TBC4**	**CE6-TBC6**	*CE6-TBC7*
CE8-TBC1	**CE8-TBC2**	**CE8-TBC3**	**CE8-TBC6**	**CE8-TBC7**
ME2-TBC2	**ME2-TBC3**	**ME2-TBC4**	**ME2-TBC6**	**ME2-TBC7**
ME13-TBC1	*ME13-TBC2*	**ME13-TBC4**	**ME13-TBC5**	**ME13-TBC7**

| IN738-TBCA | IN738-TBCB | IN738-TBCC | IN738-TBCD | IN738-TBCE |
| N5-TBC1 | N5-TBC2 | | | |
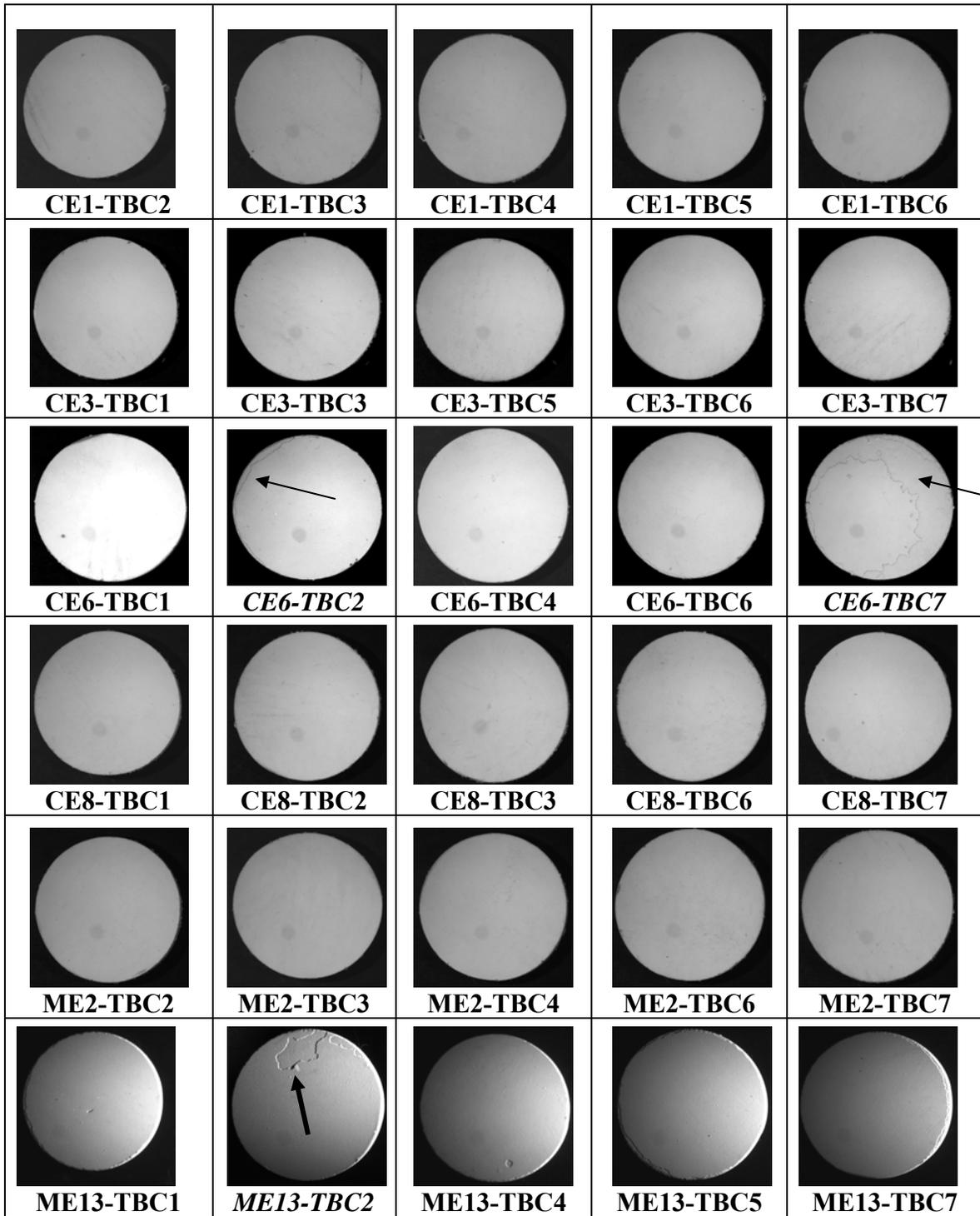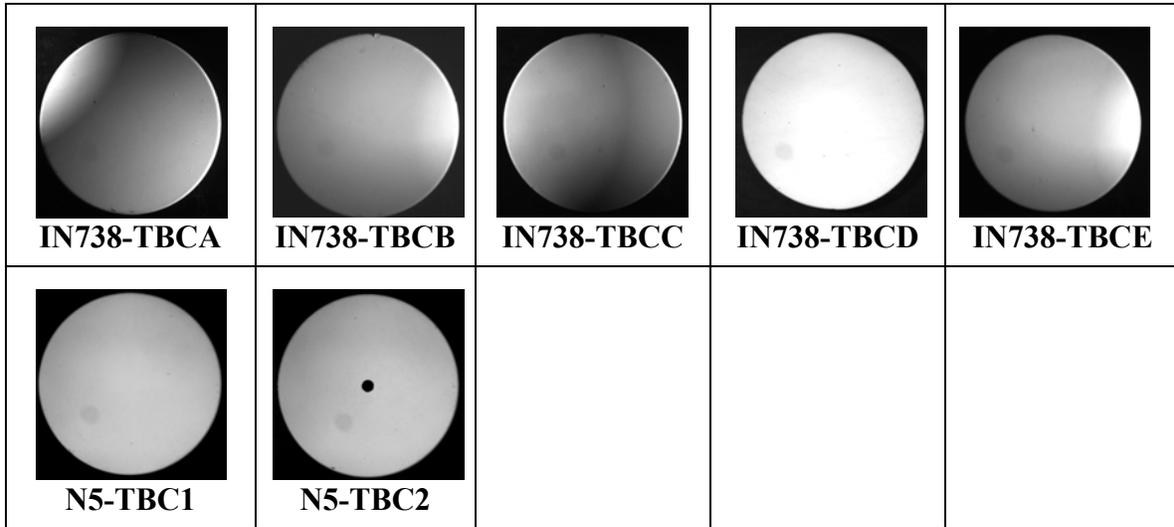
Figure 6.1 Single Crystal Superalloys coated with Y$_2$O$_3$-ZrO$_3$.

The thermal barrier coating was deposited at the Howmet Corporation. The process included chemical vapor deposition to produce the (Ni, Pt) Al bond coat followed by a heavy grit blast to remove grain boundary ridges from the bond coat. The next step was coating with Yttria Partially Stabilized Zirconia (6-8 wt%Y$_2$O$_3$ – ZrO$_2$). The thermal barrier coating was deposited by means of electron beam physical vapor deposition EB-PVD. It is important to note that the heavy grit blasting procedure left a coarse and rough surface onto which the thermal barrier coating was deposited.

Upon receiving the coupons, one coupon for each of the superalloys was examined in the as processed condition. These as processed coupons were sandwiched using .33[mm] thick aluminum plates and clipped on the coupons using coiled pins from Struers. Sandwiching the superalloys preceded the mounting of specimens in a resin, which was allowed to dry for twenty-four hours to be later polished in a pseudo-automatic polishing machine down to 3[μm] using Al$_2$O$_3$ polishing solutions. After polishing, the mounted specimens were coated with palladium prior to SEM and EDS

analysis, in order to avoid charging of specimens. This concluded the preparation procedure for the as received substrates which were then examined using the scanning electron microscope and EDS analysis, with the exception of René N5 for which only two specimens were manufactured. The same procedure was also used in the preparation of failed specimens.

The rest of the thirty specimens were cyclically heated at 1100 $^{\circ}$C in an automatic programmable vertical furnace (See Figure 5.2) until failure occurred. A heating period consisted of twenty cycles. A cycle consisted of a sixty-five minute time span, divided into three stages. The first stage was a ten-minute period that raises the coupons from room temperature to 1100 $^{\circ}$C. The second stage was a forty-five minute plateau at 1100 $^{\circ}$C. The third and final stage was a ten-minute period that reduces the temperature back to room temperature. A diagram for the thermal cycle is presented on Figure 5.3.
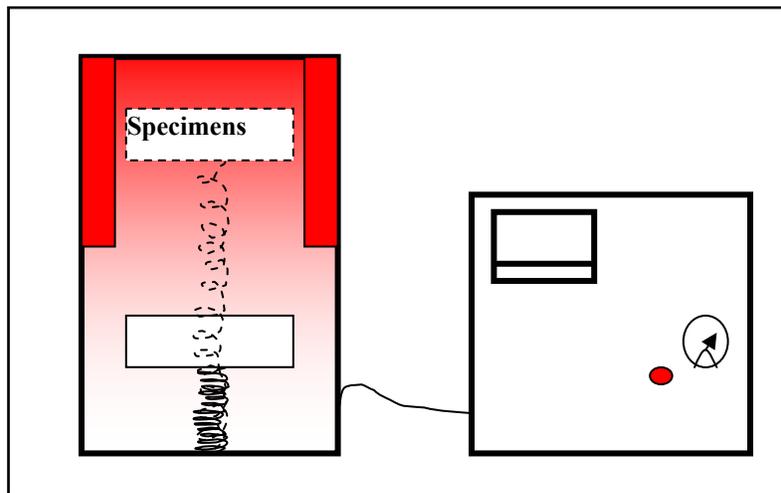
Figure 6.2 Sketch of the automatic programmable furnace used for cyclic exposure of the coupons.

Removal of the specimens from the test occurred after visual spallation and/or fracture of the thermal barrier coating. Following spallation of the TBC, four more steps

were performed to document failure characteristics. These steps consisted of recording of the optical micrographs for each coupon followed by scanning electron microscopy and compositional analysis of the YSZ spalled scale and examination of the interface where the failure occurred at the coupon. The final step included electron microscopy and EDS analysis of the cross section for each of the failed coupons. The same mounting procedure used for the as received specimens was employed to examine the cross sections of the specimens after cyclic failure.
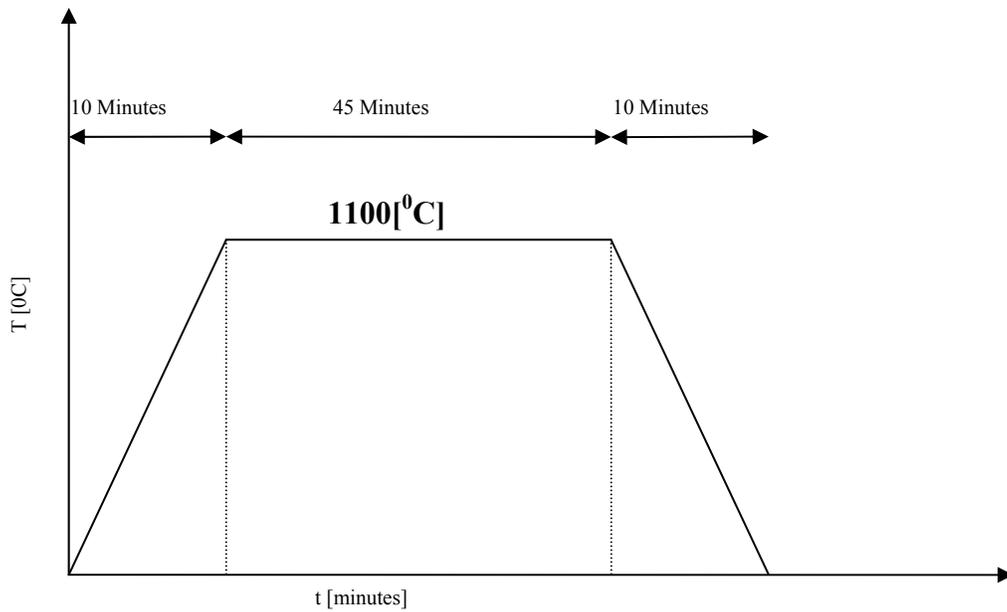
Figure 6.3 Temperature diagram followed by the automatic furnace.

7.0 RESULTS

Substrates displayed very similar features for the as processed conditions and shall

be displayed within the next subsection. Substrate classification is determined after all

failures occurred in reference to N5, the overall best performer. According to this

classification, the superalloys are categorized as high cycle failures, medium cycle

failures, and short cycle failures. Figure 7.1 is a chart presenting the categorization of

these superalloys.
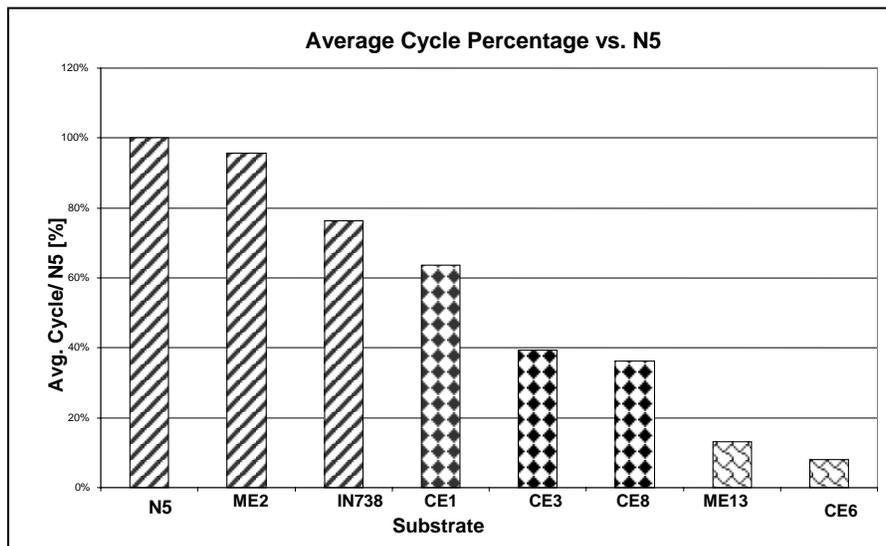
Figure 7.1 Average life cycle percentage with respect to Rene N5, which outperformed all other superalloys.

7.1 AS-PROCESSED SPECIMENS

The as-processed specimens display a mean thickness of the YSZ layer of 130 microns, while the thickness of the bond coat shows a mean thickness of 50 microns. Although the system has been grit blasted after deposition of the bond coat, it can be seen in the forth coming figures that a thin thermally grown oxide in the range of .2-.5 μm develops between the YSZ and the bond coat. In addition to the thermally grown oxide, various defects can also be seen and are hereto presented. The bond coat chemical composition yields a beta phase of (Ni, Pt) Al.
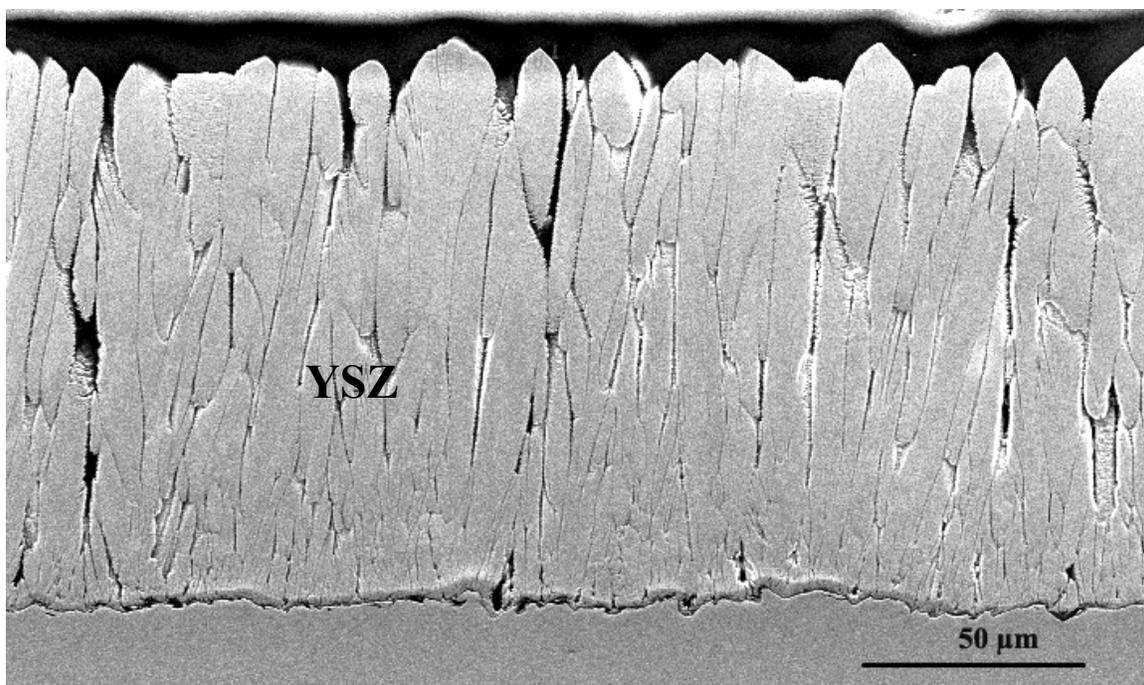
Figure 7.2 As processed YSZ grains on a grit blasted beta β (Ni,Pt) Al bond coat.

Various micrographs are included in this segment in order to present a visual perception of the general defects of the specimens. Figure 7.2, displays the as-processed YSZ layer, along with the grit blasted bond coat. It is easy to note from this micrograph

the initial undulations of the YSZ/TGO and TGO/Bond Coat interface. Along the bond

coat intra-layer, it is possible in some instances to see cracks expanding along the

chemical vapor deposited bond coat as seen in Figure 7.3. Cracks also propagate along

the YSZ/Bond Coat interface. Low cycle substrates display numerous holes in the as

processed conditions as seen in Figure 7.4. Figure 7.5 shows some of the effects created

by the grit blasting process, as part of the bond coat seems to have been removed and

only a YSZ/Substrate interface exists; moreover, a large group of YSZ grains in a conical

shape is formed. A conical shaped aggregate of grains formed without a contact point is

also seen in Figure 7.6.
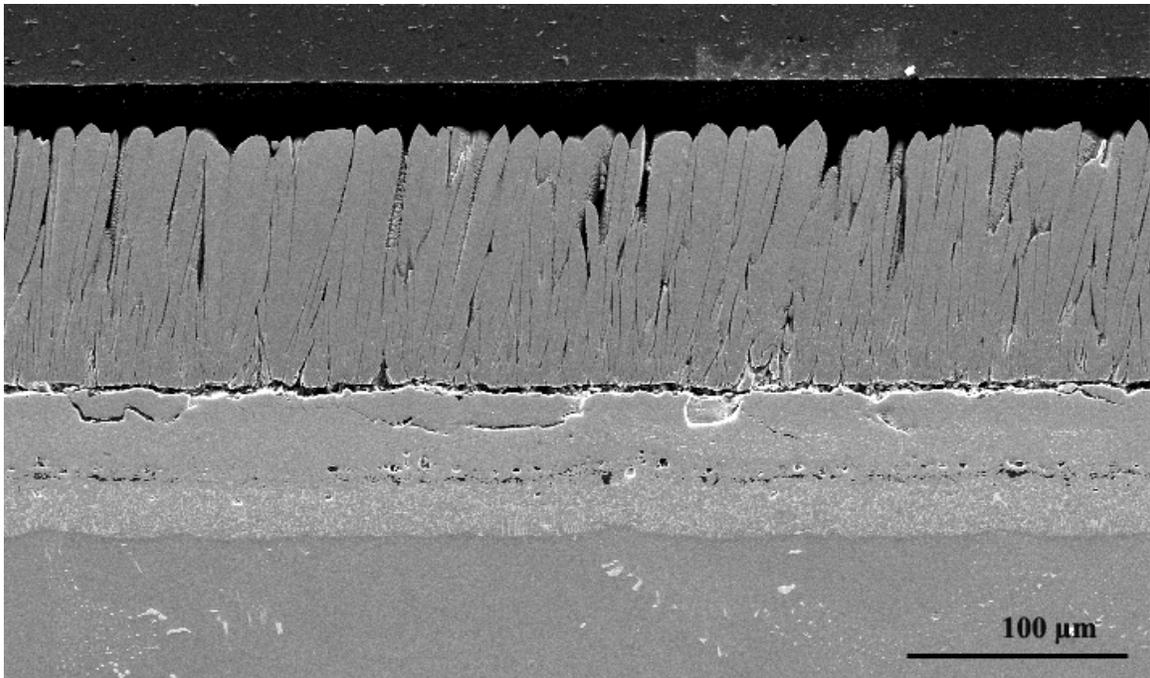
Figure 7.3 As processed thermal barrier coating system with cracks present inside the bond coat and along the YSZ and bond coat interface.
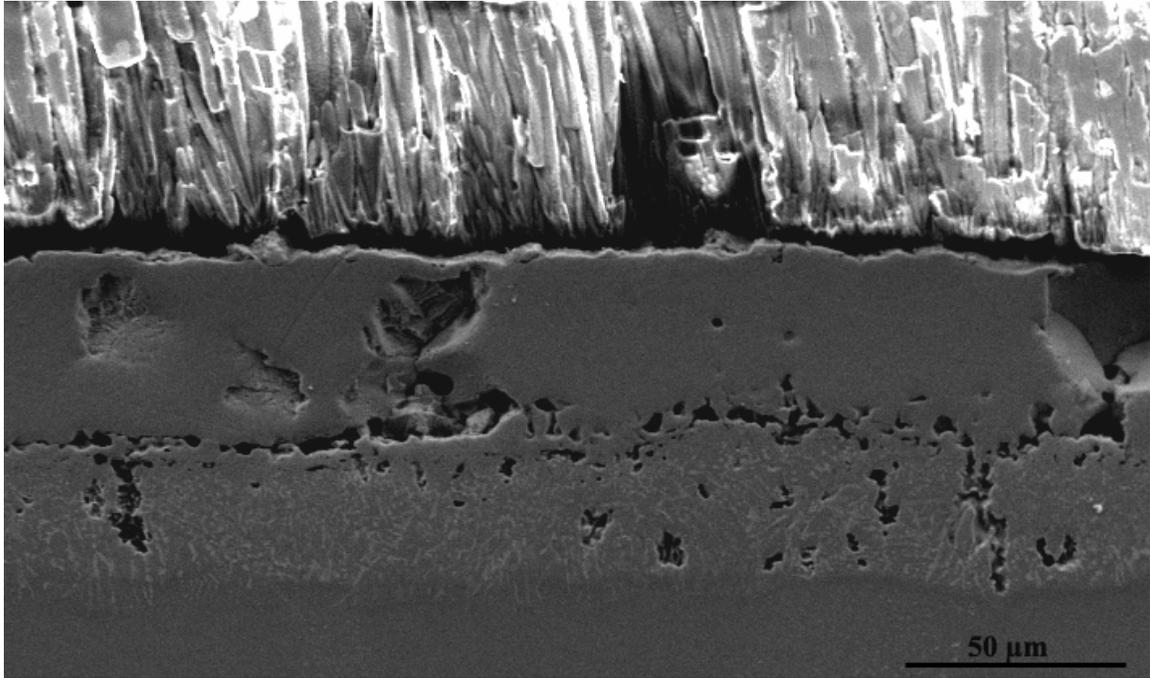
Figure 7.4 As processed bond coat with numerous holes along the bond coat /ceramic overlayer interface. Holes run into the interdiffusion area.
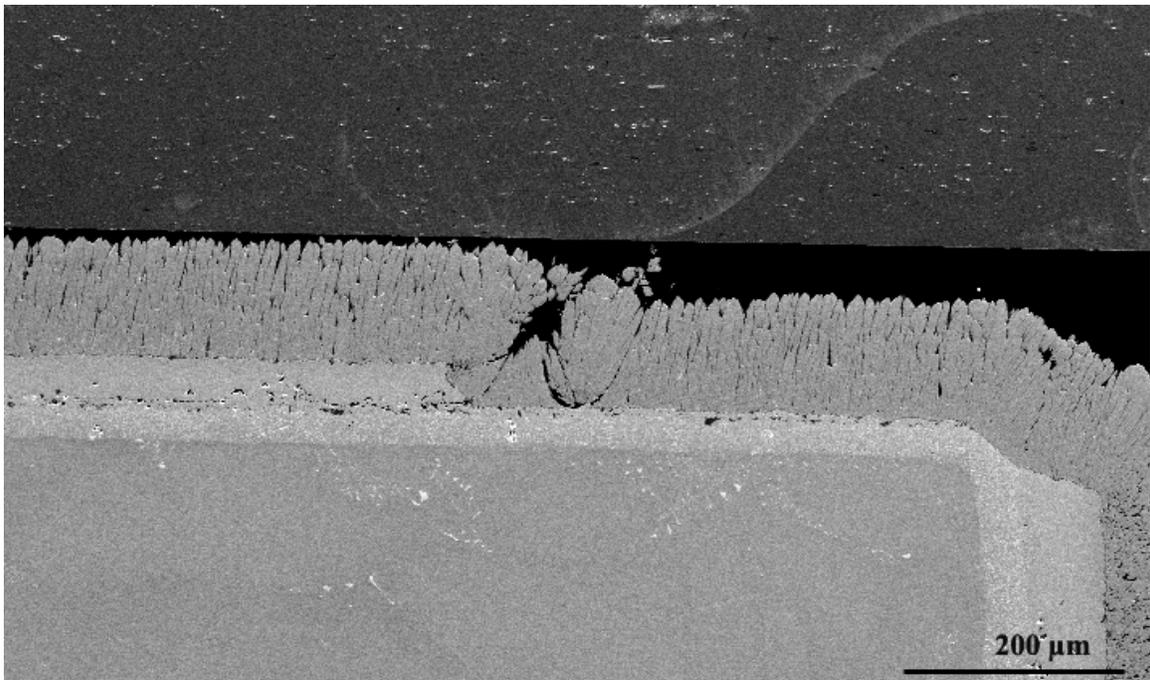
Figure 7.5 Thermal barrier coatings system without the bond coat can be seen here due to the heavy grit blasting technology.
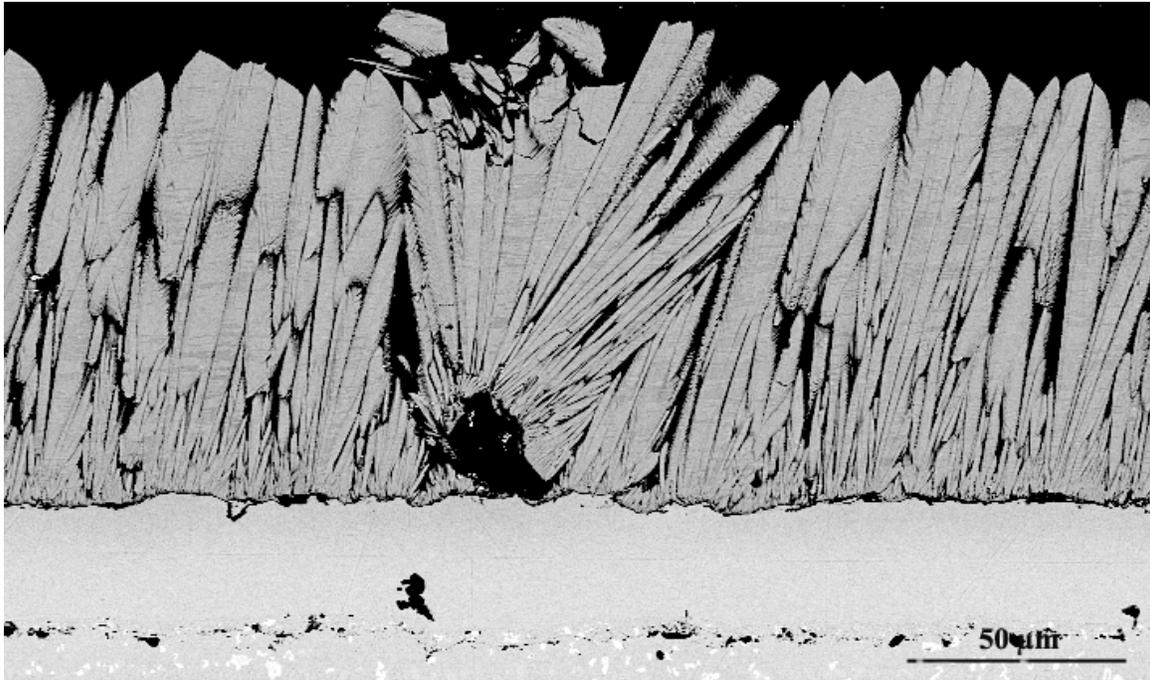
Figure 7.6 Conical defect created by the rough surface does not have a contact point with the bond coat.

Closer examination of the as-processed specimens, shows a weak interface constituted by porous and discontinuous grains. Figure 7.7 - 7.9 show once again the response of the EB-PVD YSZ to the rough-surfaced bond coat. Figure 7.7 shows no contact surfaces, which can easily slip during high tensile stress conditions. On a larger magnification in Figure 7.8, the discontinuous growth of the YSZ scale created by a deep undulation and competition among the YSZ grains to grow, can be seen; hence, a void is formed and high stress points at each one of its ends are produced. Although heavily grit blasted, the thermal barrier system contains a thin thermally grown oxide as exhibited in Figure 7.9. The TGO formed during YSZ deposition which occurred after the grit blasting. The TGO is continuous along this interface and is the product of high temperatures used during the deposition of the YSZ.
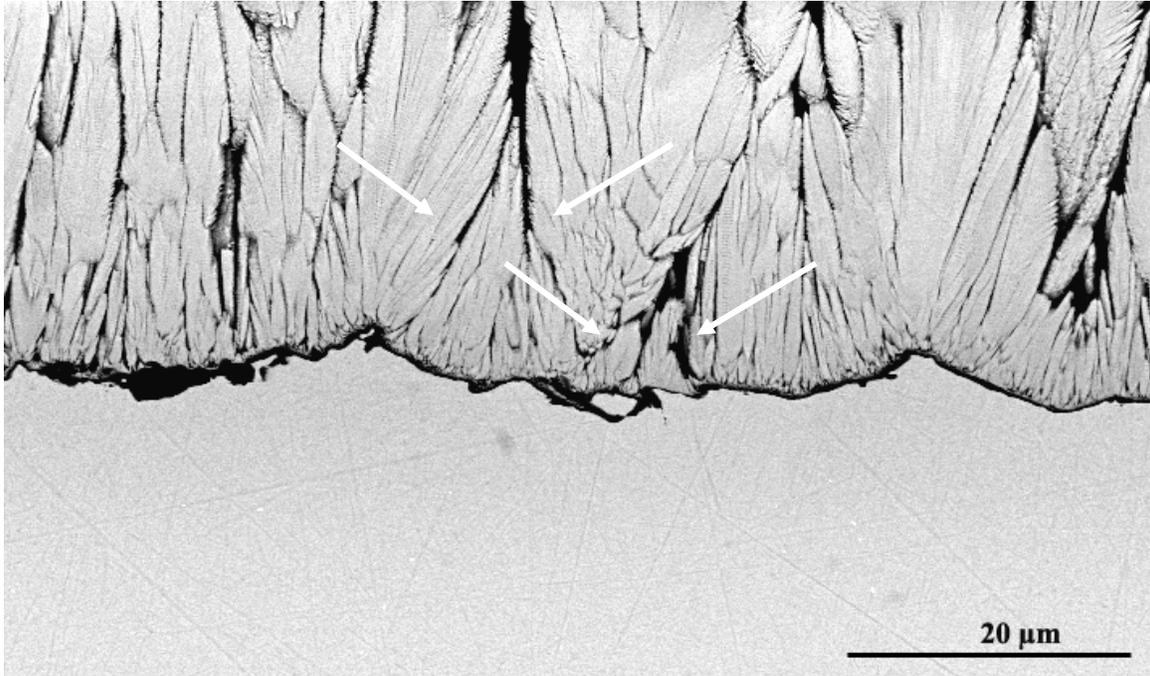
Figure 7.7 Undulations of the rough surface create zero contact planes, easy to pull under normal stresses.
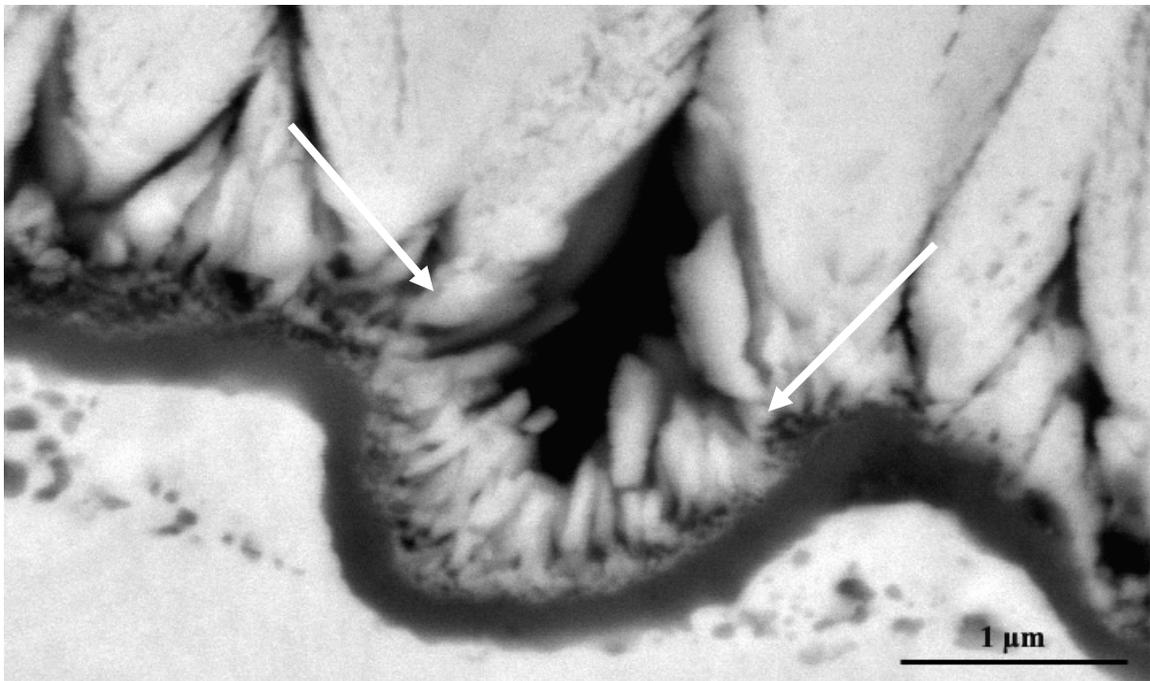
Figure 7.8 Rough Surface undulations create inhibitions for the continuous growth of YSZ leaders, creating vacancies and stress concentration points.
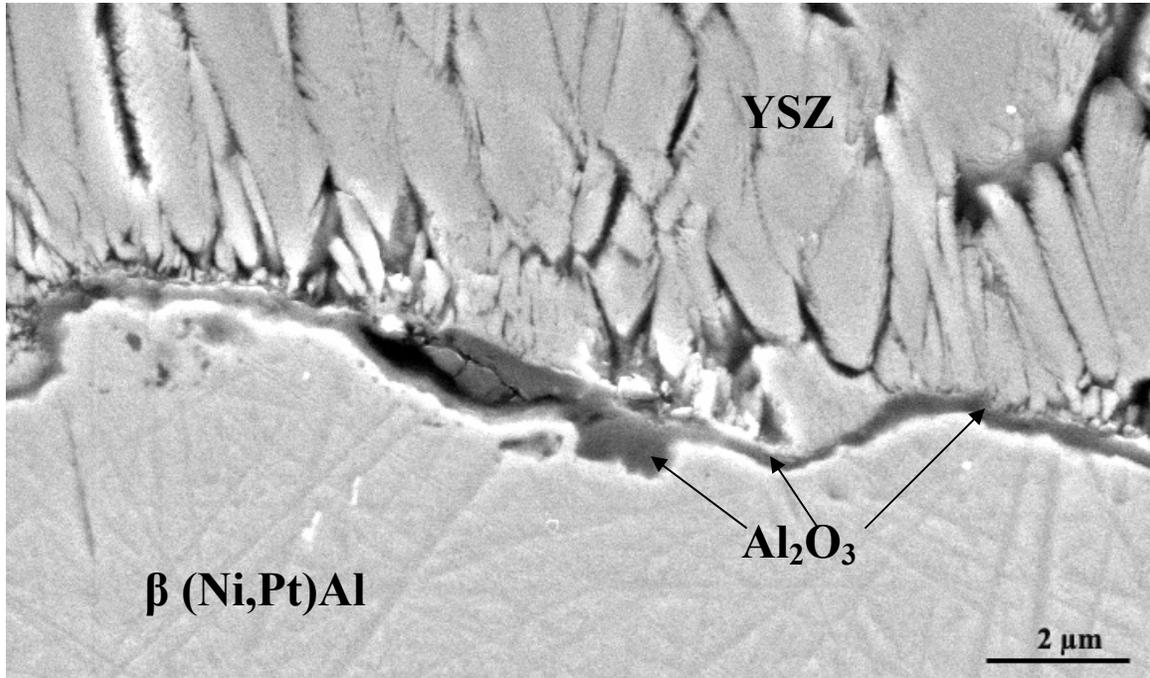
Figure 7.9 A porous YSZ/TBC interface with various discontinuities, also a thin Al$_2$O$_3$ layer close to 200 nm.

The interdiffusion area is also another very important area within the system. Micrographs were taken to represent the different interdiffusion areas that ranged from highly dense areas to dense when compared to each other. Figure 7.10 represents the interdiffusion area of high cyclic failure samples. The entire interdiffusion area has a width close to 20 microns, comprised by globular and acicular precipitates. In addition to the dense precipitate area, alumina particles are also present above the interdiffusion area. Figure 7.11 unlike the previous figure, represents the interdiffusion area of a low cycle failure specimen. Noted is the distance between the interdiffusion area and the bond coat, which when compared with the previous and next figure is a very small distance. Figure 7.12 corresponds to mid-cycle failures and, as seen here, there are various precipitates, mostly globular of different sizes which become larger as they get closer to the bond coat.

In addition to the precipitates, Figure 7.10 - 7.12 all show Al_2O_3 particles most likely

incorporated during deposition of the bond coat.

Figure 7.10 The interdiffusion area below the thermal barrier coating system.
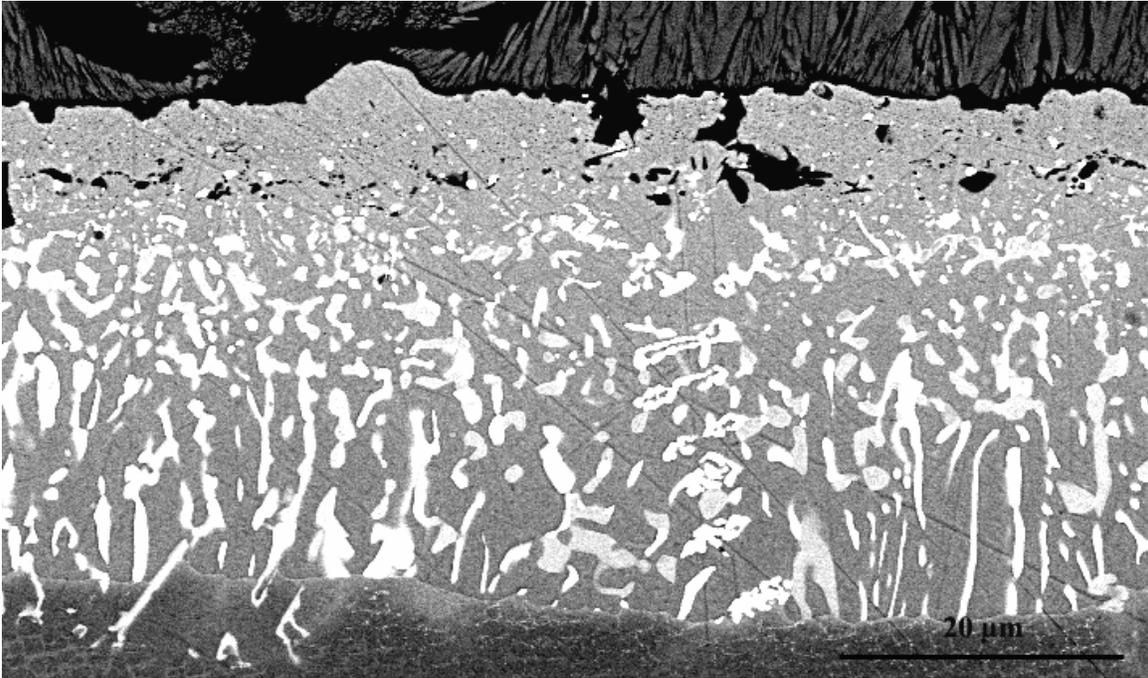
Figure 7.11 Interdiffusion area of a low cycle failure specimen.

Al$_2$O$_3$
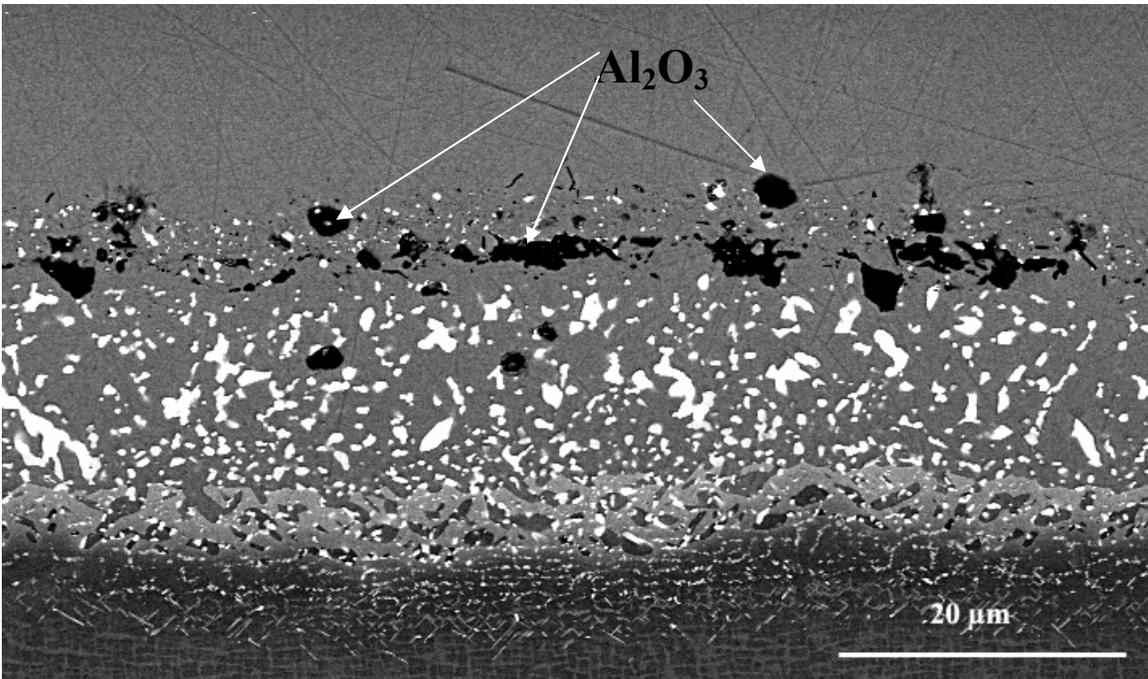
Figure 7.12 Interdiffusion area of a mid-cycle failure TBC specimen for as processed, atop some alumina particles.

7.2 HIGH CYCLE FAILURE

Cycles to failure expressed as a percentage of the cycles to failure for N5 can be seen in Figure 7.1. High cycle failure refers to the left most three specimens seen in Figure 7.1, which are René N5, Inconel 738, and ME2. René N5 achieved the highest failure average reaching a maximum mean of 800 cycles. ME2 reached the second highest in this category with 765 cycles per specimen and finally Inconel 738 reached a mean life of 610 cycles per specimen. All specimens failed along the YSZ/TGO interface, although in some instances spallation of the TGO is seen along with some reoxidation of the bond coat. Phase transformations occur at the bond coat due to aluminum depletion, β (CsCl), β' (L1$_0$), γ' (FCC) phases are seen. This is mostly due to the formation of the thermally grown oxide and the depletion of aluminum from the substrate. In addition to the depletion of aluminum, the behavior of other elements such as the refractory metals should also be noted, which segregate to the interdiffusion area forming primary, secondary, and perhaps even a tertiary reaction zone.

7.2.1 Performance of René N5

René N5 outperformed all of the third generation alloys by a percentage difference ranging between 4% for the closest and 92% for the furthest, as seen in Figure 7.1. It also outperformed Inconel 738 which is not a single crystal, but rather a polycrystalline alloy. The main form of failure for these specimens includes one along the YSZ/TGO interface as seen from the failure surface of the YSZ scale and the failure surface of the substrate, Figure 7.13. On the YSZ failure surface, as seen in Figure 7.14,

it is possible to pick out areas where a large amount of the YSZ is missing, a link that is later used to reinforce the failure mechanism of ratcheting. Figure 7.15 displays thermally grown oxide adhered to the YSZ surface after failure. Some of the bond coat is visible, which indicates that failure also occurred along the TGO/Bond Coat interface, as seen in Figure 7.16.
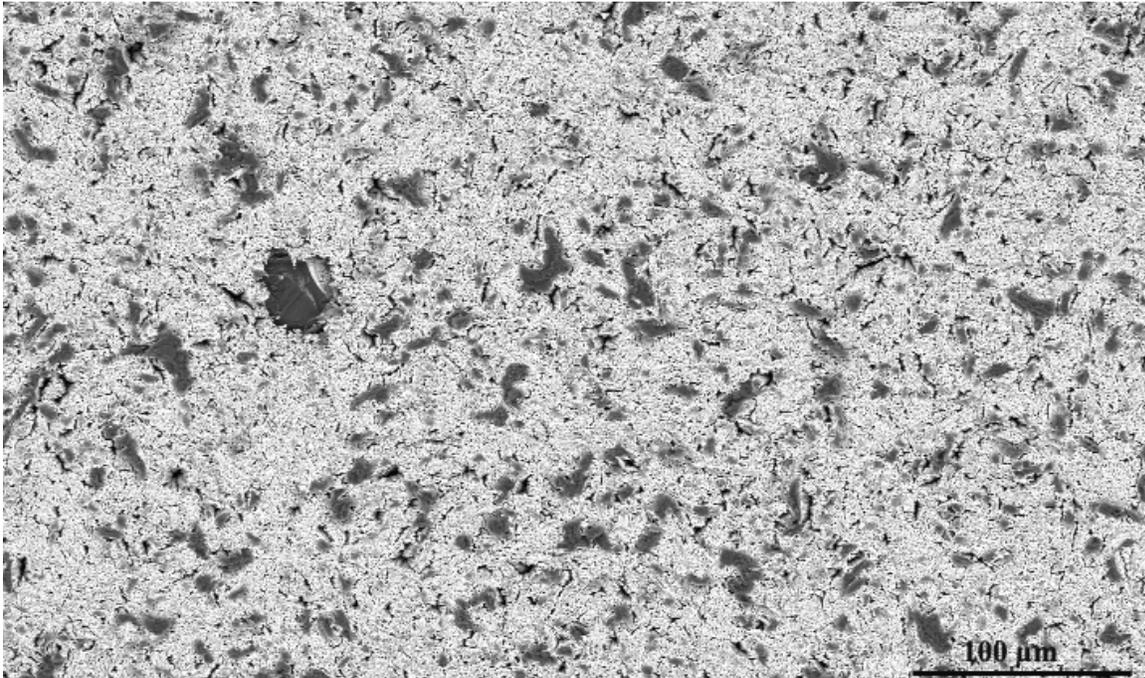
Figure 7.13 YSZ failure of Rene N5 comprised of the supporting YSZ ceramic (white area) and the thermally grown oxide (dark areas).
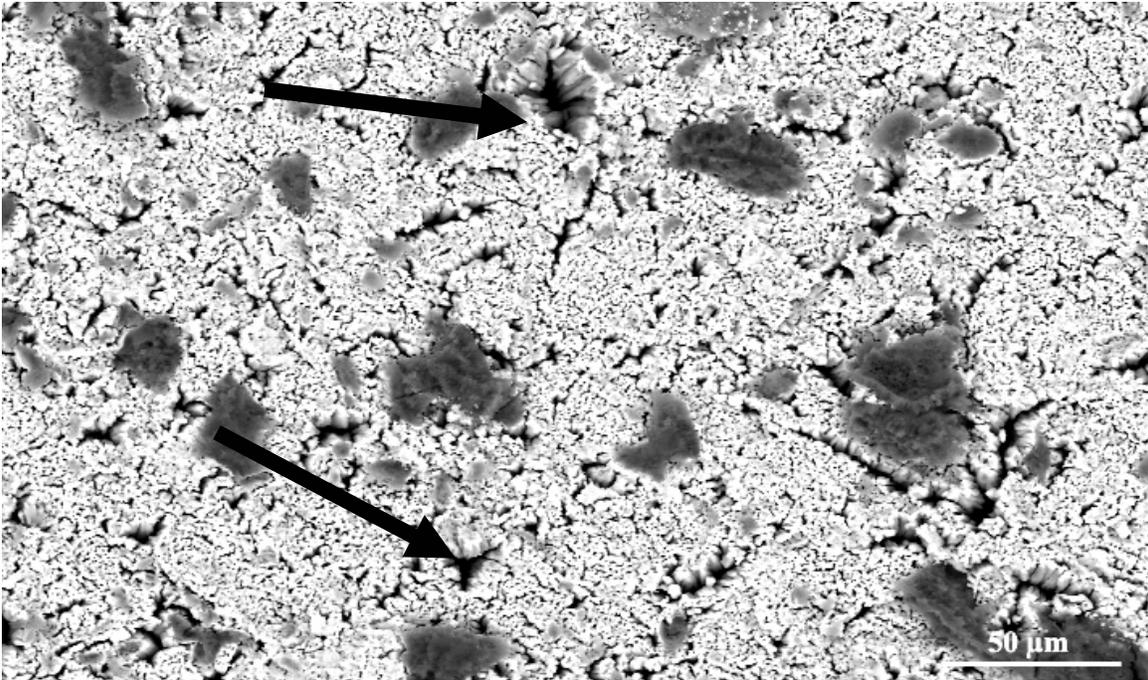
Figure 7.14 Closer look at the YSZ/TGO failure surface shows the loss of YSZ noted by black arrows, and the alumina adhered to the surface.
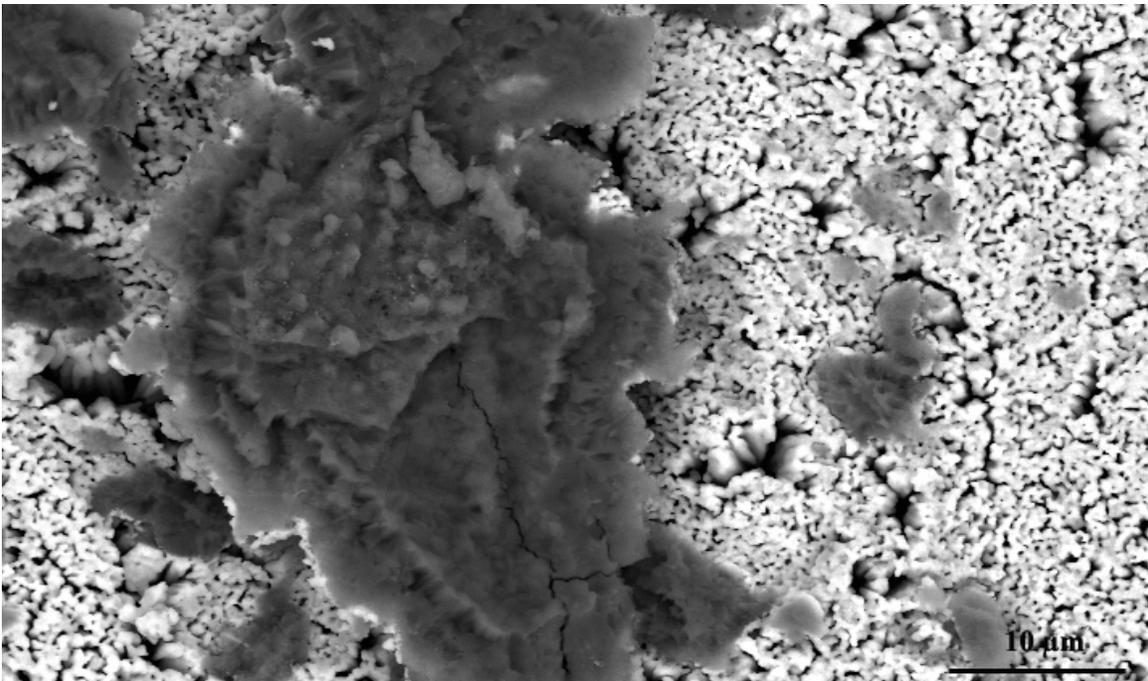
Figure 7.15 Thermally grown oxide adhered to the YSZ after failure of the TBC system on a N5 specimen.
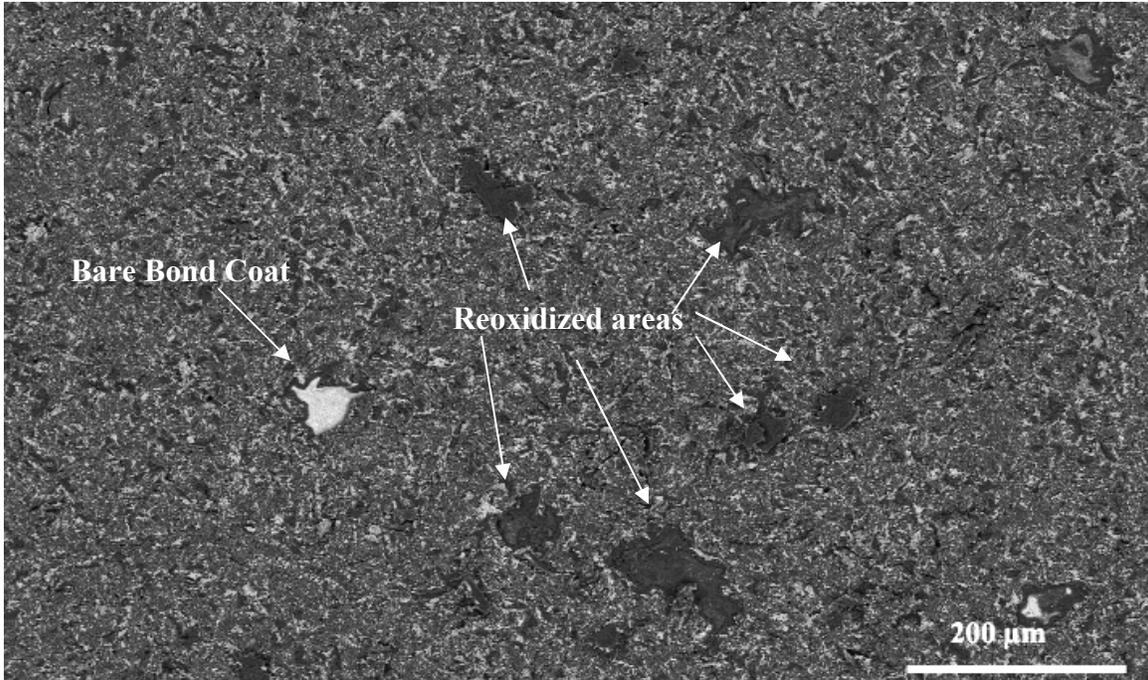
Figure 7.16 Surface area of the substrate after failure shows a large amount of alumina and various bond coat reoxidized sites.

Surface holes were also present at the substrate surface failure as seen in Figure 7.17. A magnification of these holes on Figure 7.18 yielded high traces of Ni, Al, and O. Figures 6.19-6.21 show an area of the bare bond coat, which shows very different features. Figure 7.19 shows a micrograph of a reoxidized area, with large traces of Ni, and some traces of Cr. The following figure exposed surface, shows the formation of alumina on a Ni rich surface, Figure 7.20. Finally, Figure 7.21 shows the initial stage of a bare bond coat prior to reoxidation. In this figure, different shades on the substrate are seen, which are featured holes along which grain boundaries are noted.
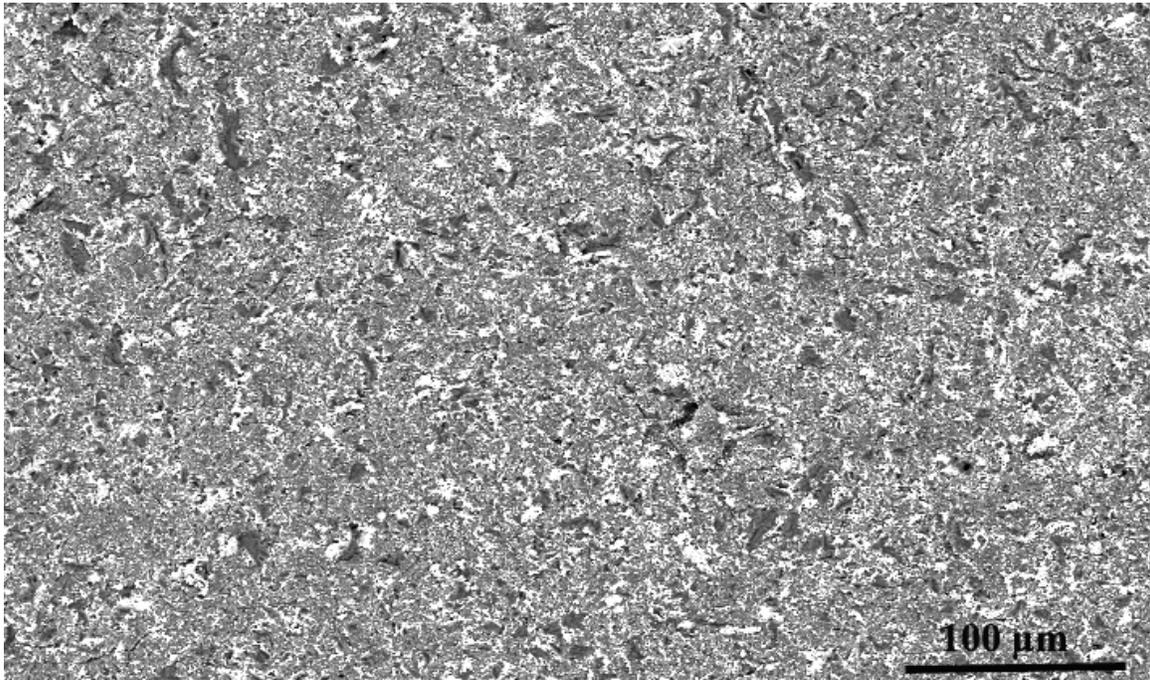
Figure 7.17 Substrate failure surface shows some YSZ adhered and underneath the thermally grown oxide.
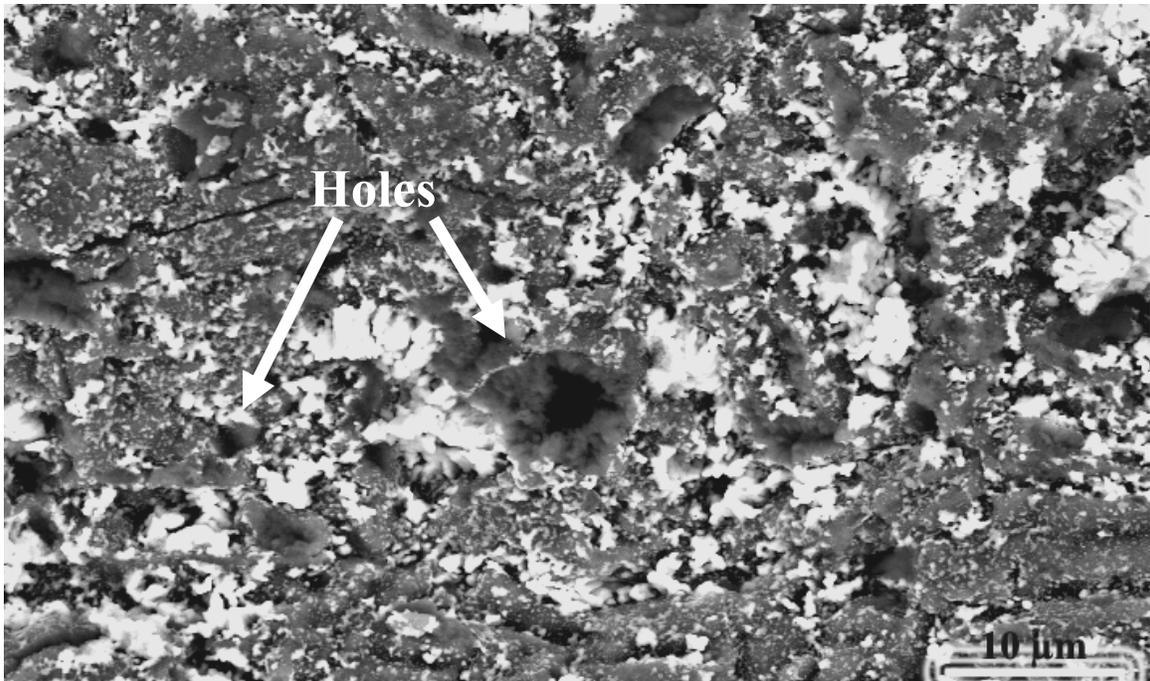
Figure 7.18 Numerous holes on the substrate surface after failure, also seen is the detached YSZ adhered to the TGO.
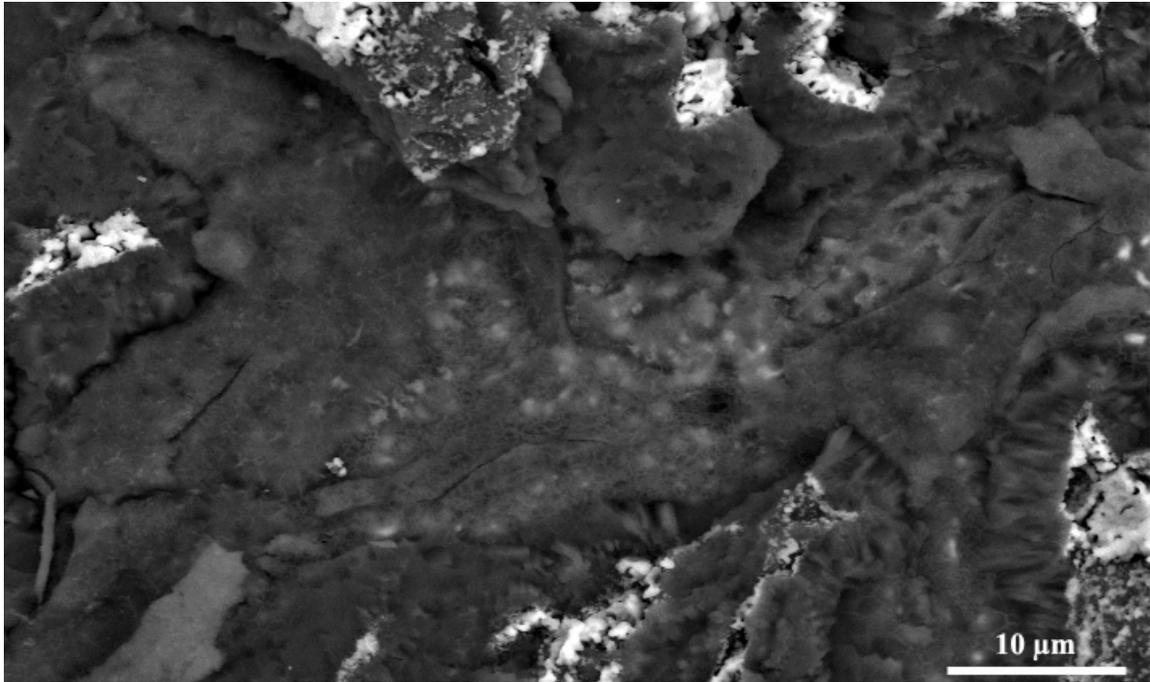
Figure 7.19 Reoxidized bond coat surface.
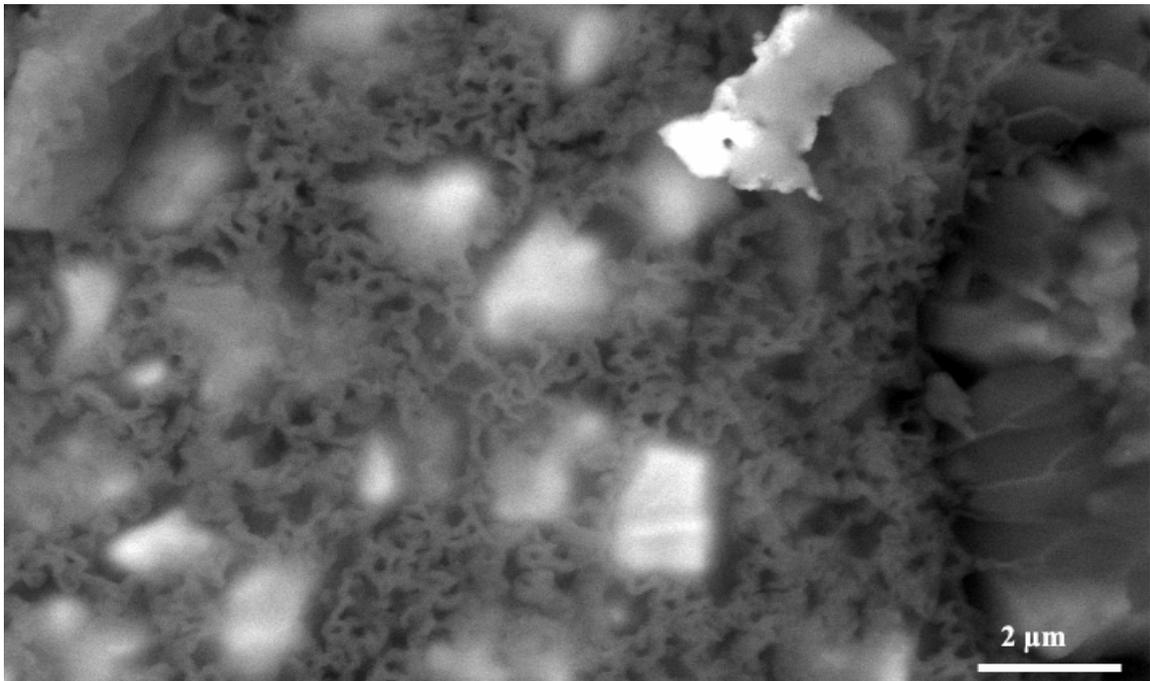
Figure 7.20 Reoxidized substrate surface shows precipitates of Al rich in Ni.
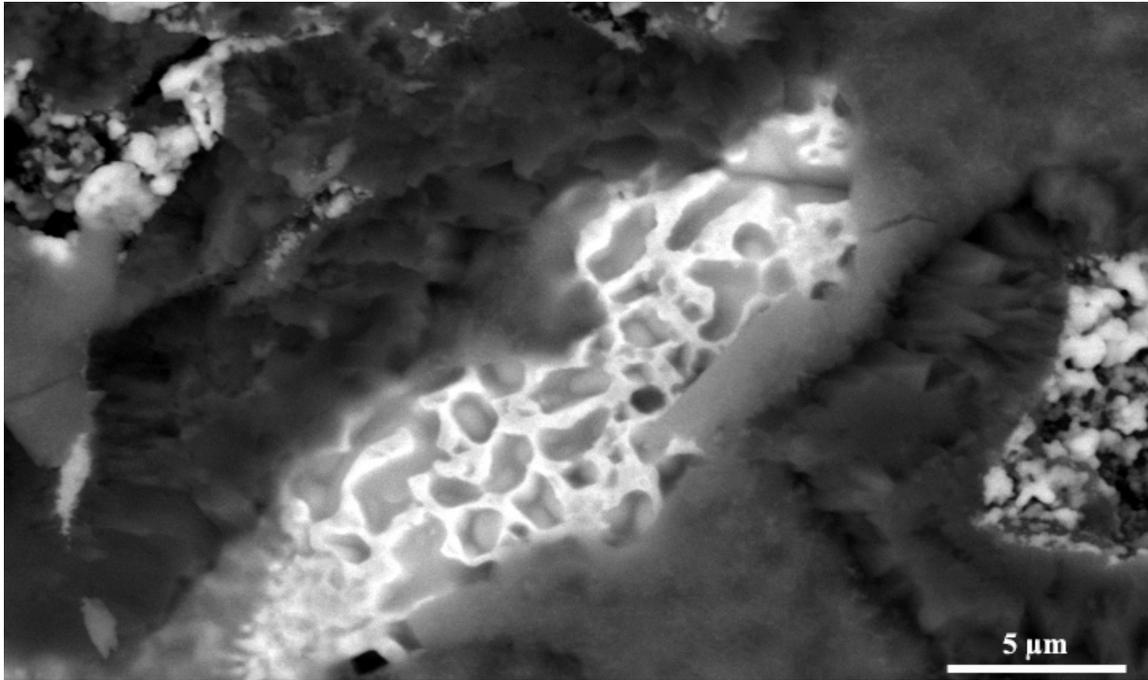
Figure 7.21 Nickel rich bare bond coat shows holes and grain boundaries on the bond coat.

Cross sectional examinations of these specimens indicated a very weak interface between the YSZ and the TGO was responsible for the failure seen, (Figure 7.22). Moreover, oxidation of the bond coat surface in many areas as the undulations increased in size show that the specimens failed by ratcheting (Figure 7.23). Another characteristic of these N5 coupons as well as most of the rest of the other third generation alloys is the complete phase transformation from the β (NiAl) $\rightarrow$ β' (L1$_0$) taking place in the bond coat (also Figure 7.23). β' was identinfied by composition analysis and later by etching. TGO thickness plays a significant role in the failure of TBCs, as residual and growth stresses in the TGO can increase and produce failure along the TBC/TGO interface. Here it is seen in Figure 7.24 that the TGO on N5 accumulated an average thickness of 5 μm at failure. Figure 7.24 notes that most deformation occurred at martensitic regions, and not at γ' regions. Yet, in observance of the substrate composition as the primary variable in

48

this study, it is important to indicate what happens to the substrate elements, primarily the refractory metals, during the cyclic thermal exposure. Tantalum is seen to segregate to the gamma prime phase at the interfacial boundary with the thermally grown oxide. Figure 7.25 shows the interdiffusion area, including large precipitates and small precipitates. Closer to the bond coat are TCP precipitates in the globular and acicular shapes, mainly constituted from two phases; one phase contains W, Ni, Cr, Co, and Mo, the other phase contains Cr, Ni, Re, W, Co, and Mo. The secondary reaction zone is populated by finer globular precipitates composed of the same elements seen in the primary reaction zone, while the tertiary reaction zone has acicular precipitates rich in Re, Ni, Cr, W, Co, and Al. All these zones differ in the size of their precipitates as well as the distance from the bond coat.
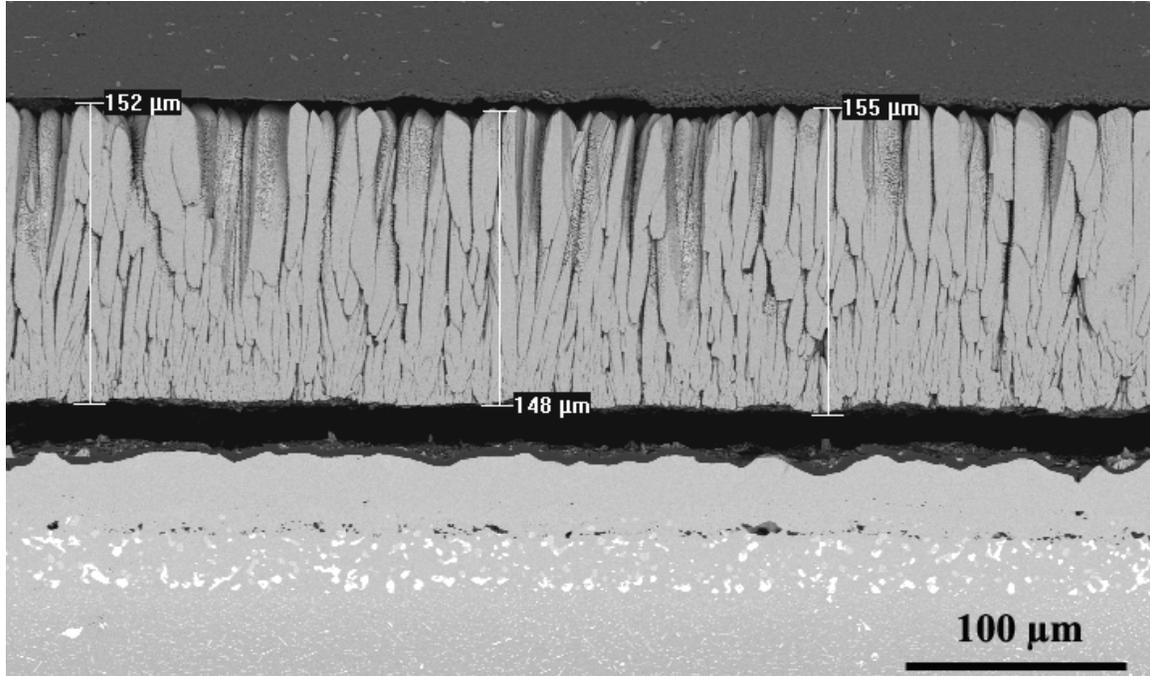
Figure 7.22 YSZ and TGO separation after failure indicative of a weak interface.
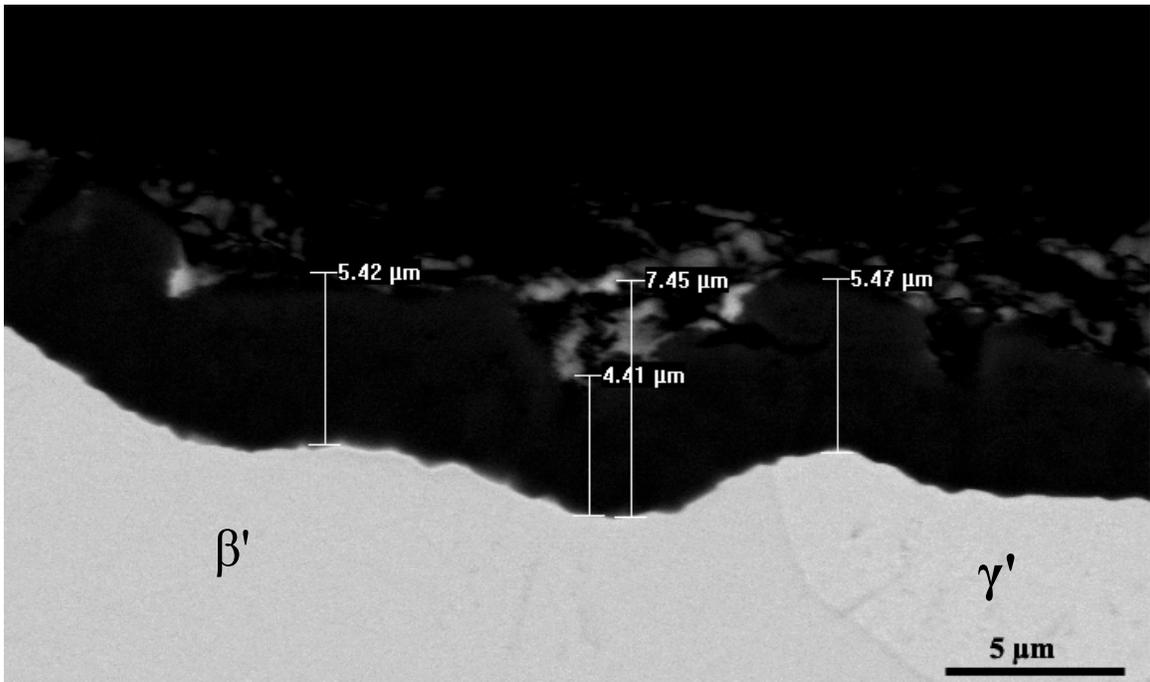
Figure 7.23 Ratcheting effect increases undulations while simulteneously accumulating oxide. Both β' and γ' populate the bond coat region.
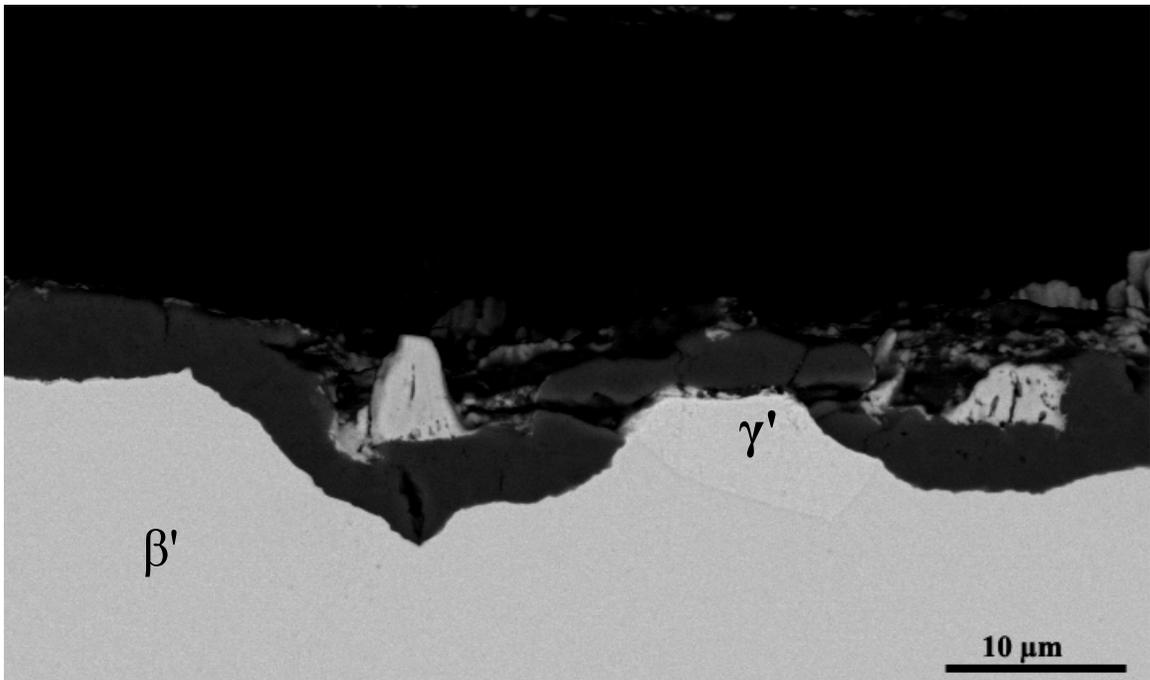
Figure 7.24 TGO thickness at failure for N5. TGO appeared to deform at martensitic regions and not FCC.

Acc.V Spot Magn   Det WD Exp   50 µm
15.0 kV 3.0 500x   BSE 10.0 1   N5-1, HT Cross Section, p.5
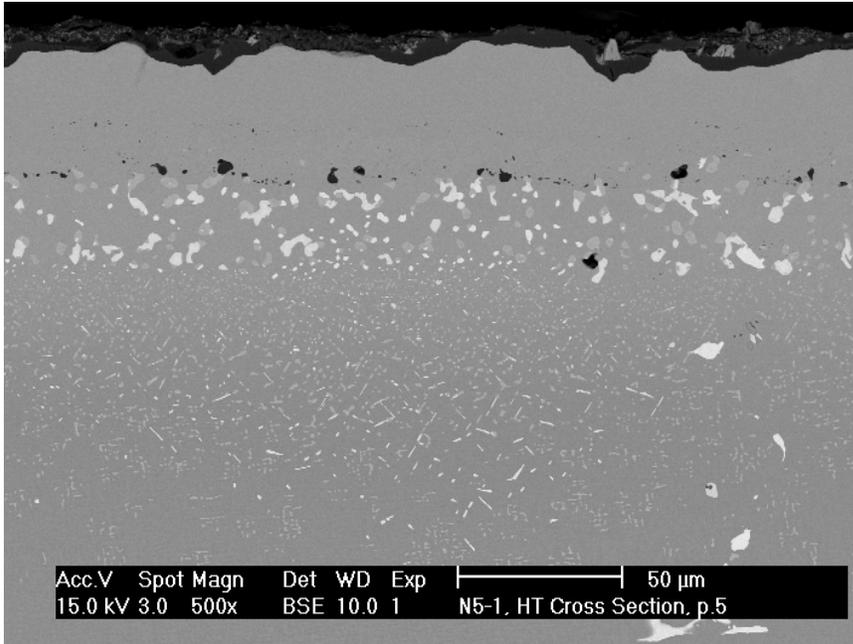
Figure 7.25 Interdiffusion area of N5 at failure.

7.2.2 Performance of ME2

Substrate ME2 performed particularly well, being among the third generation

alloys and the only substrate of its kind in this category of high cycle failure. ME2

averaged 765 cycles per specimen, or 96% of N5s total. Like the best performer N5,

ME2 also failed along the YSZ/TGO interface, as seen in Figure 7.26. Some areas from

which the TGO spalled did appear, although they were not as prevalent as on N5.

Thermally grown oxide portions or bits are attached to the YSZ, an indication of a crack

that changes planes during propagation. Some of the largest portions can be seen in

Figure 7.27. The substrate side of the failure did not show as many spalled or reoxidized

areas as N5 showed (see Figure 7.28 and 7.29). Nevertheless, some were present as seen

in Figure 7.29. Besides spallation of the TGO and exposure of the bond coat, another

important feature is seen in Figure 7.30. As it appears on Figure 7.30, a compilation of

YSZ grains remained attached to the surface of the TGO while the TGO extended into the bond coat. This loss of YSZ grains produces holes in the YSZ scale, in addition to cracks that lead to failure. ME2 also developed more surface holes than N5, as seen in the Figure 7.31.
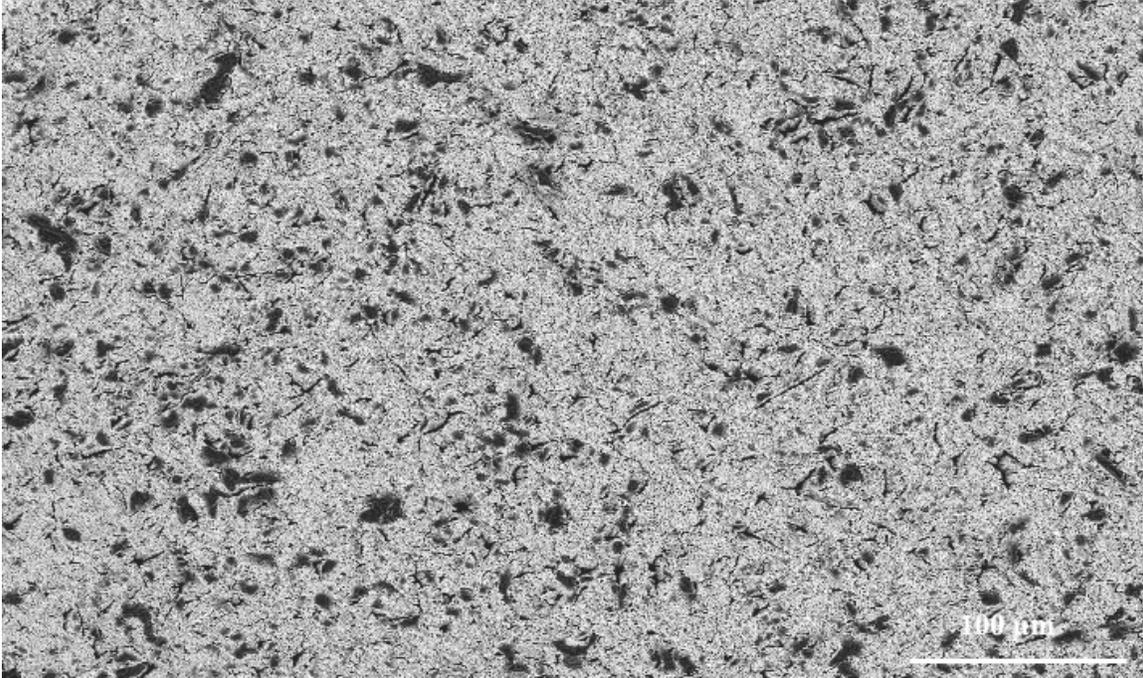
Figure 7.26 YSZ Failure Surface of an ME2 specimen after 780 cycles at failure.
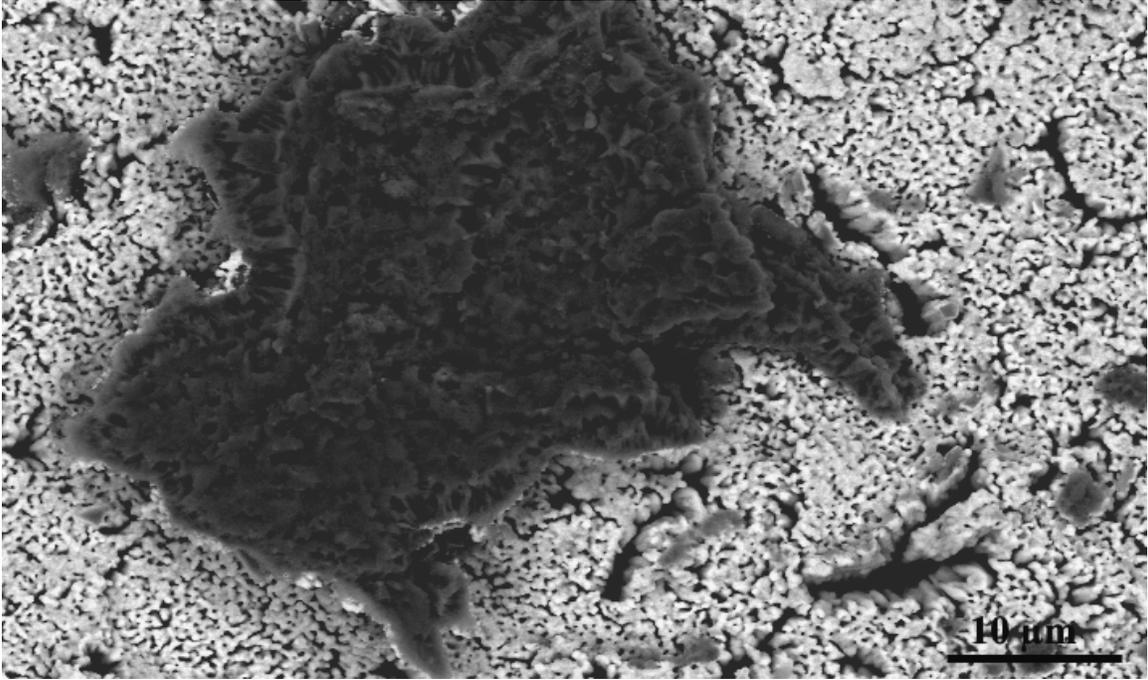
Figure 7.27 Alumina bit adhered to the YSZ scale after failure.   YSZ holes also are present on this surface, indicative of YSZ loss during cyclic heat treatment.
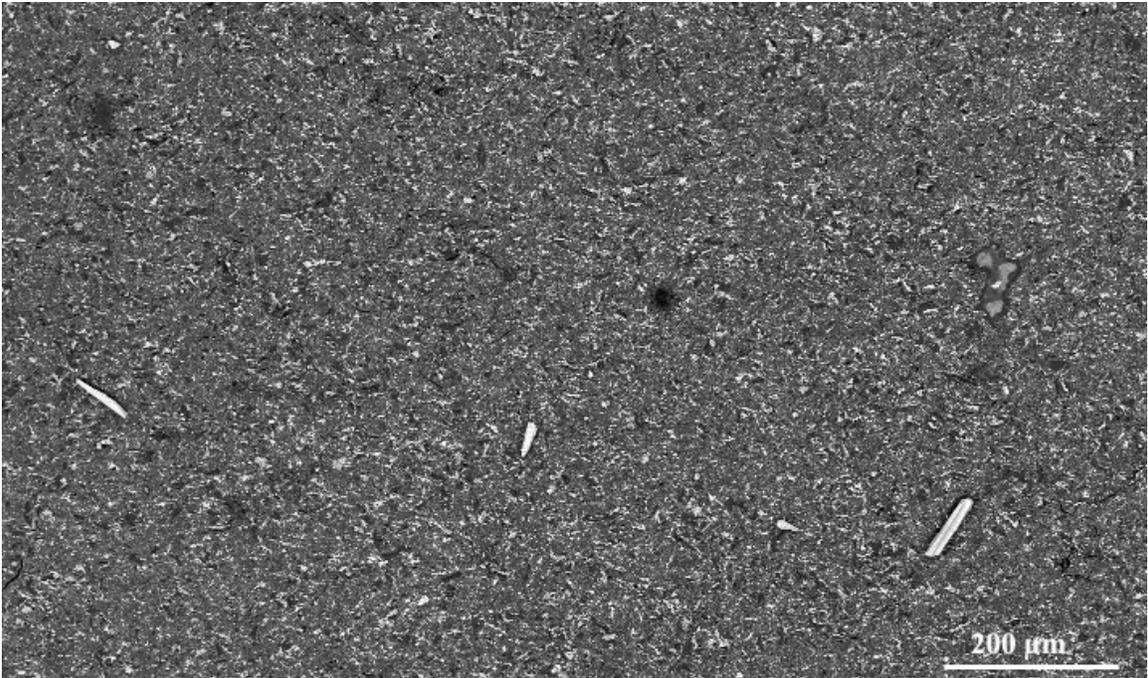
Figure 7.28 Substrate failure surface after 740 cycles, with spalled/reoxidized area at the mid right area and numerous holes.
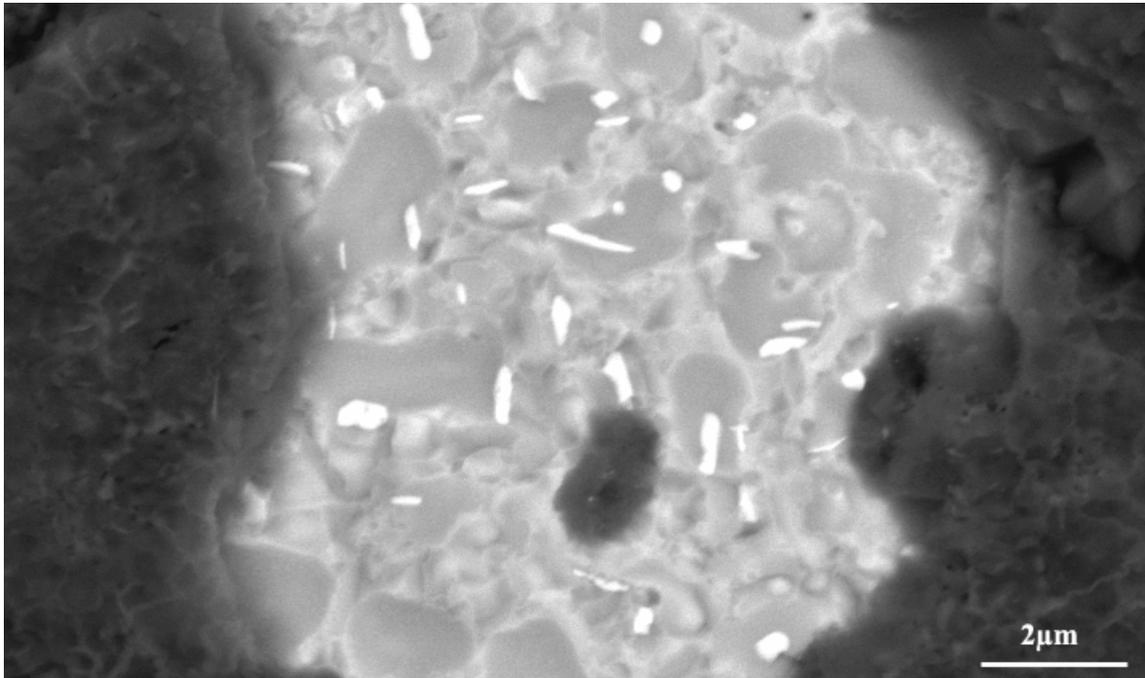
Figure 7.29 Spalled area on the failed substrate surface shows Re precipitates on a Ni matrix.
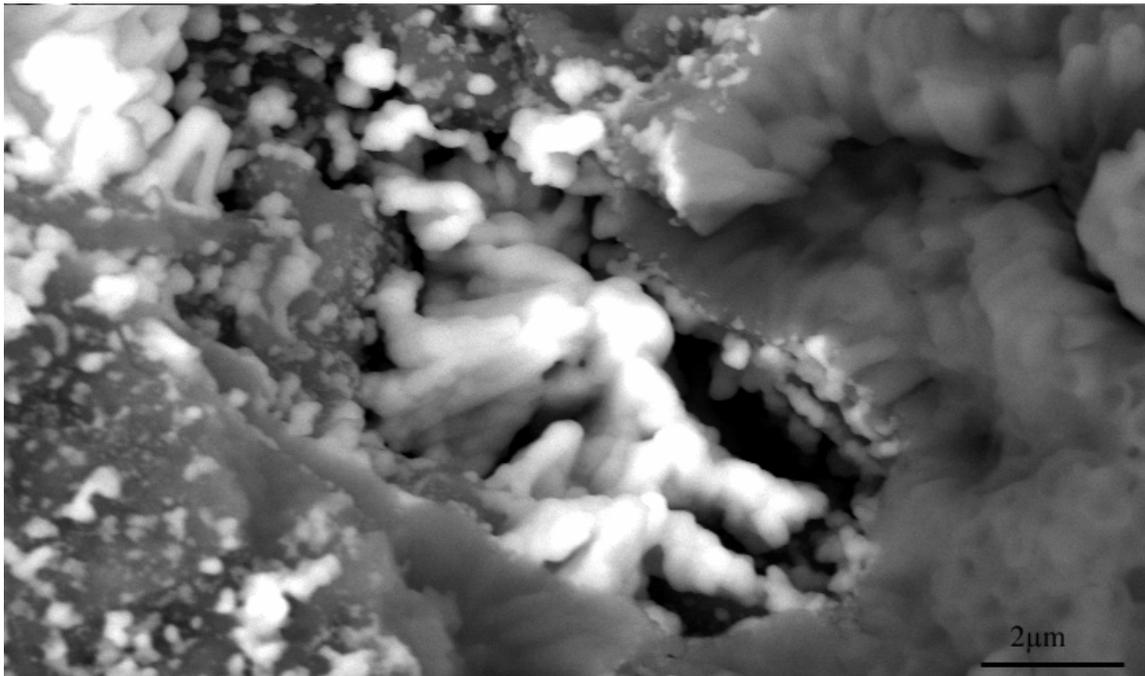
Figure 7.30 YSZ grains being absorbed by out of plane stresses created by TGO residual stresses.
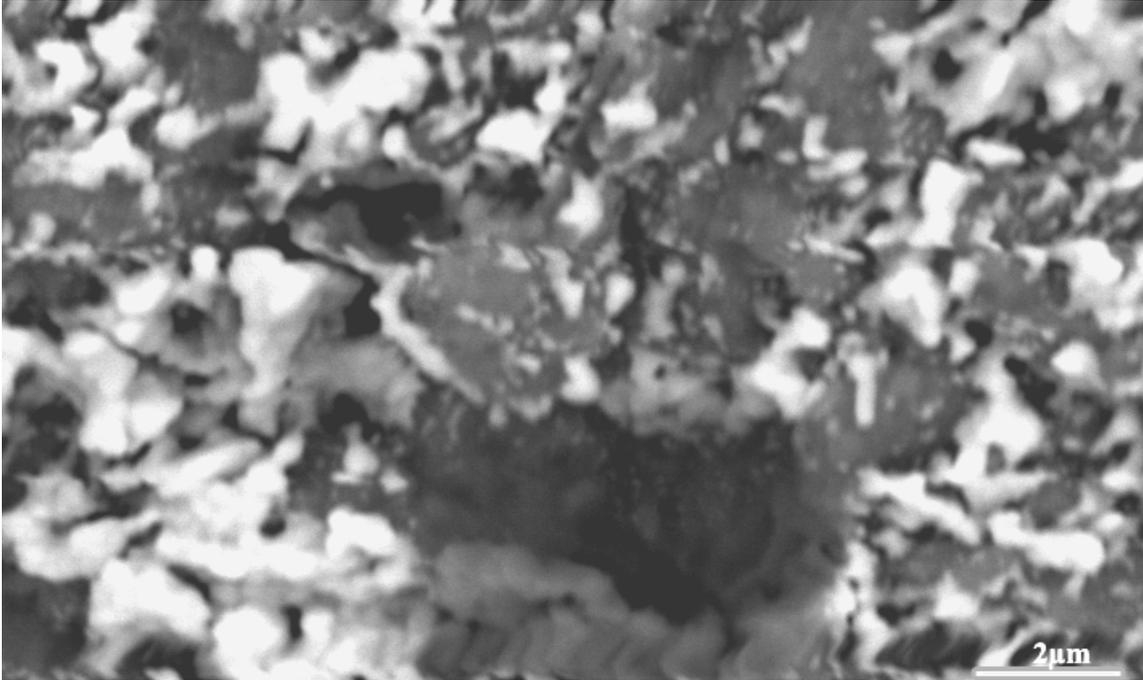
Figure 7.31 Holes on the surface of an ME2 specimen after failure due to ratcheting effect.

The cross section of the substrate develops a more pronounced deformation of the bond coat as the cycles increased, i.e. the depth of the undulations extended into the bond coat as seen in Figure 7.32. The TGO thickness, as seen in Figure 7.33, averages the same as that for N5, between 4 and 5 microns. Then moving downwards, it can be seen in Figure 7.34 that most of the substrate components did not significantly influence much in the adhesion or failure of the TBC system, as most of them formed precipitates at the interdiffusion area, both acicular and globular. The globular precipitates are rich in Re, Cr, Ni, and Co, all in descending atomic percentage concentration. The acicular precipitates are rich in Ni, Re, Cr, W, Co, Al, and Mo also all in descending atomic percentage concentration. Ni content for the globular precipitates is half of the Ni found in the acicular precipitates, while Re content in the globular precipitates is 2 times the amount of Re found in the acicular precipitates. As seen from Figure 7.34, the population

density of the precipitates is greater than that of N5. Nevertheless, as in the case of N5,

Ta segregated to the gamma prime phase along the TGO/bond coat interface.
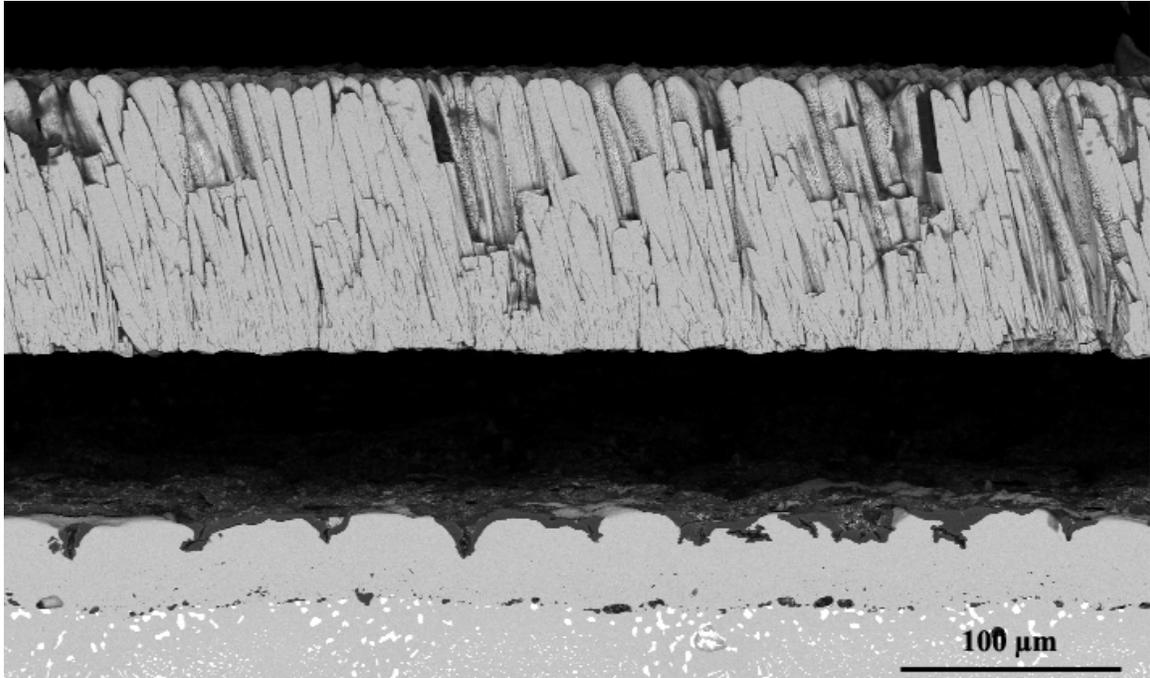
Figure 7.32 Cross sectional micrograph of ME2 points to a weak YSZ/TGO interface as well as to failure by a ratcheting mode.
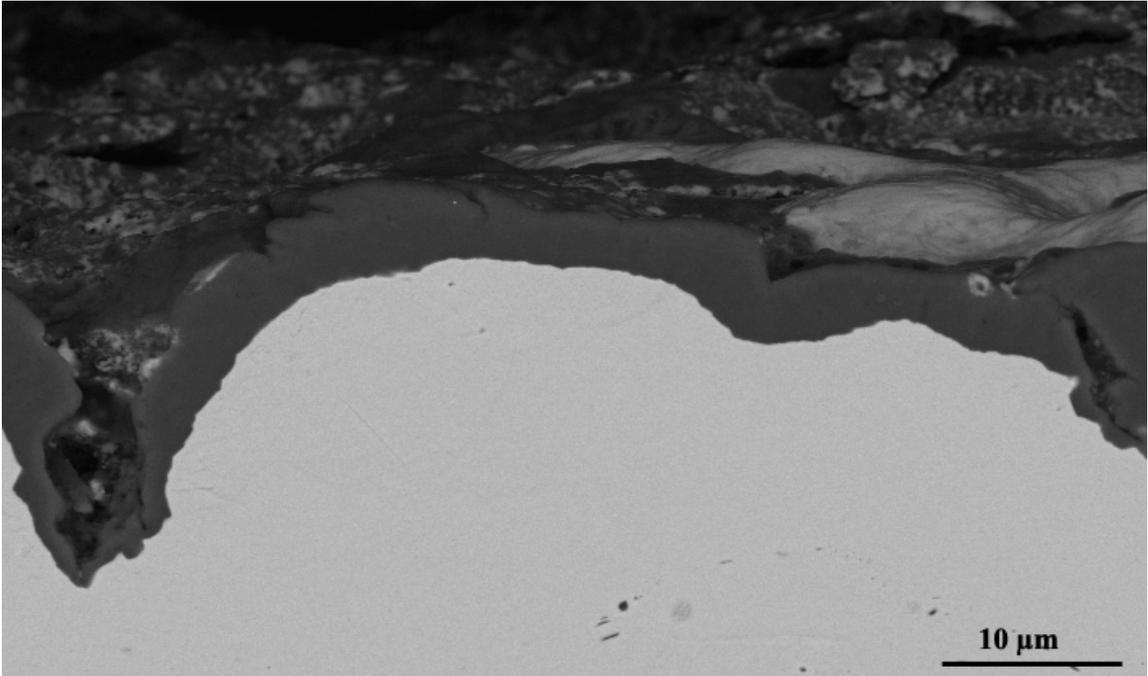
Figure 7.33 Deformation of the bond coat by a ratcheting mode allows for the oxide to penetrate the bond coat and oxidize eventually causing failure.
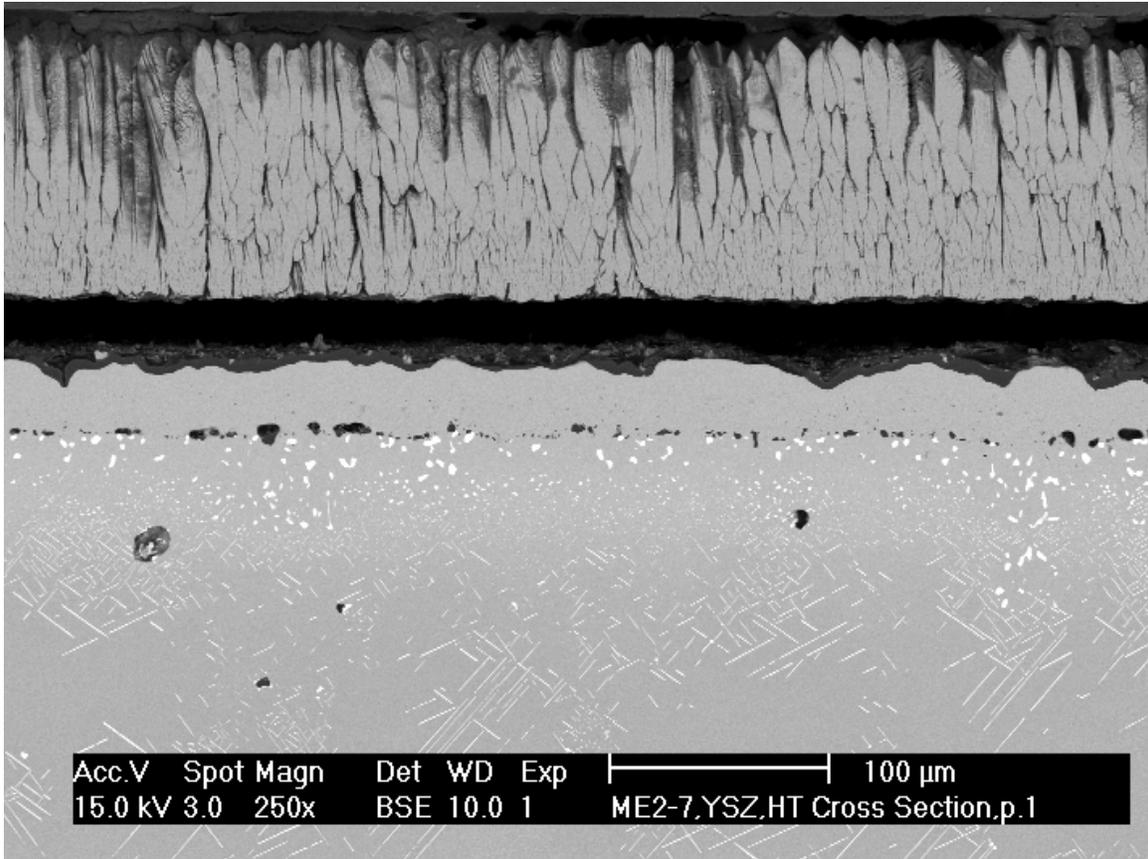
Figure 7.34 Interdiffusion area stretches vastly from the bond coat into the substrate matrix, various forms of precipitates in globular and acicular shapes.

7.2.3 Performance of Inconel 738

IN738 is the only polycrystalline substrate in the study averaging 610 cycles per specimen, or 76% from N5s total cyclic life. Failure of the IN738 specimens occurred along the YSZ/TGO interface as seen in Figures 7.35-7.41. Figure 7.35 presents the large density of TGO bits adhering to the YSZ TBC after failure, while Figure 7.36 shows a magnified view of a TGO bit after spalling from the bond coat. In this figure, it is possible to see the fine details of the TGO grain growth in contact with the bond coat. Interesting to note is that no ridge growth has occurred for the bond coat after cyclic thermal treatment. The IN738 specimens displayed in general the largest amount of TGO

spallation relative to the other substrates in the study. These specimens also displayed a large amount of bond coat reoxidation, as seen in Figure 7.37 and 7.38. Yet into other aspects and characteristics of this specimen, it is observed that cracks propagate along the TGO in the direction of the failure surface, as seen in Figure 7.39, which can improve the chances of spallation of the TGO. Figure 7.40 shows a hole surrounded by a no contact plane grain attached to the TGO after failure of the system.
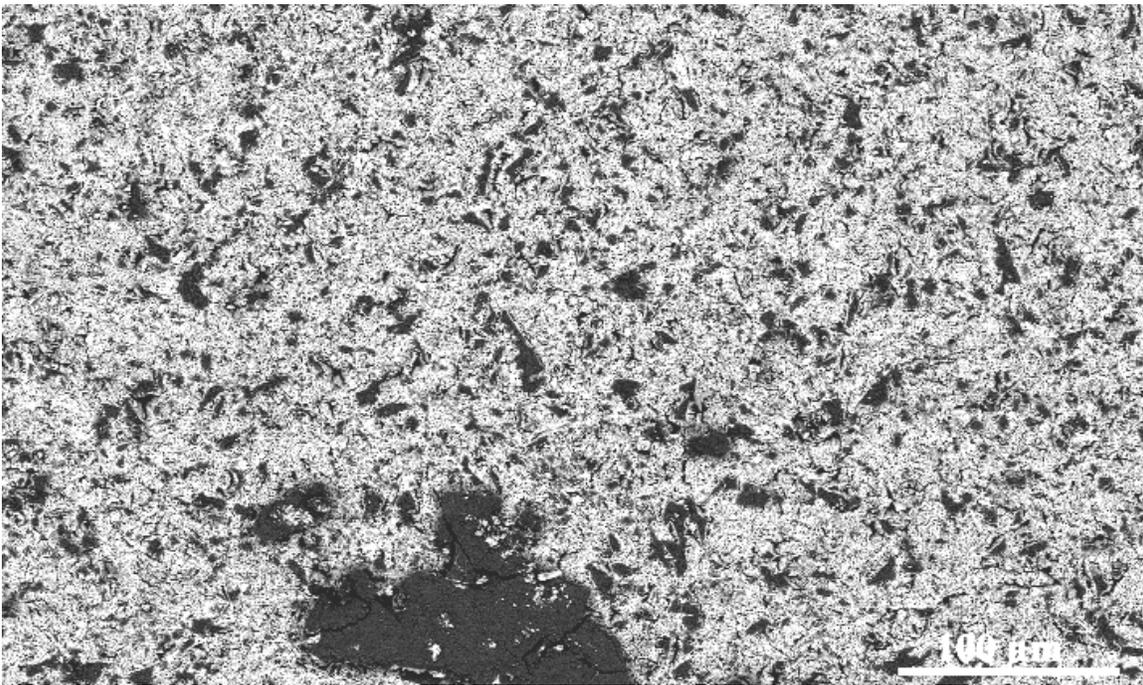
Figure 7.35 Inconel 738 YSZ failure surface displays a large amount of TGO bits as well as large portions of TGO.
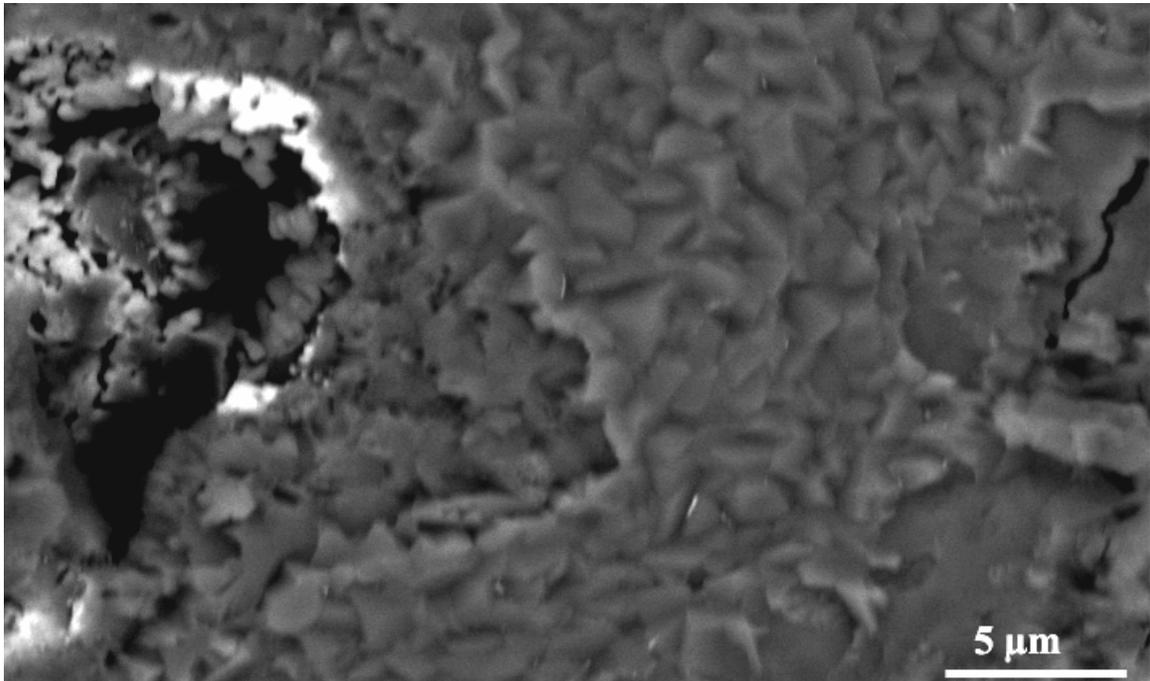
Figure 7.36 TGO on YSZ failure surface shows engraved details. These are the TGO grains in contact with the bond coat.
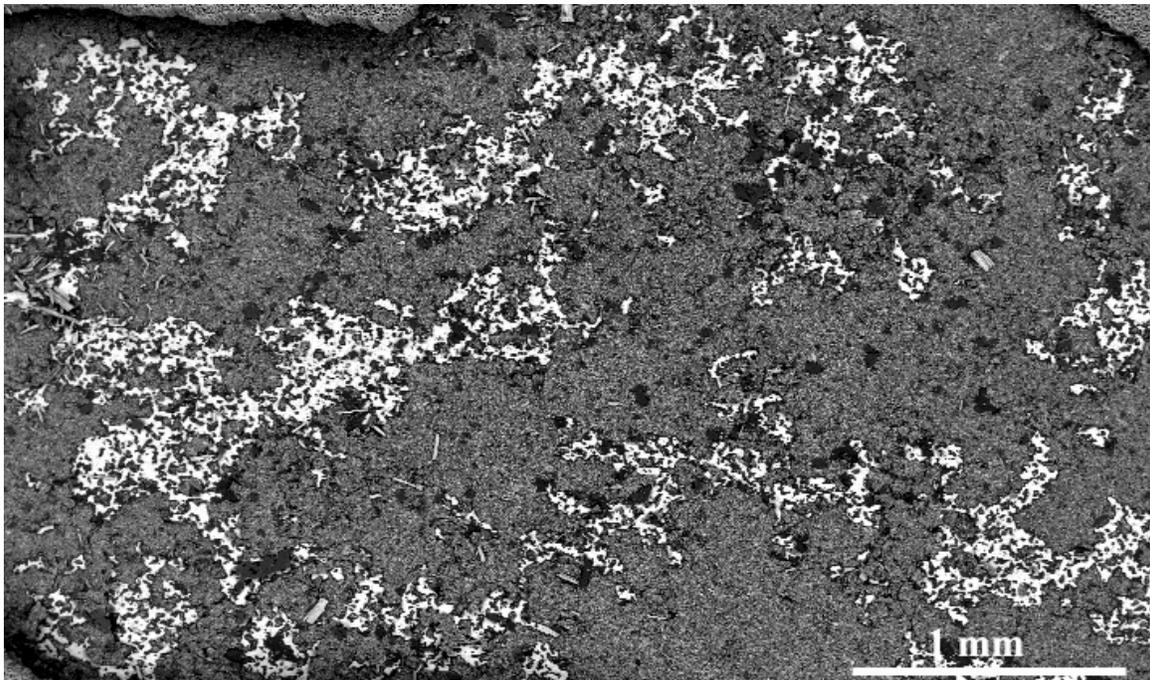
Figure 7.37 Substrate surface after failure of the TBC system displays large amounts of spalled areas, showing the bare bond coat.
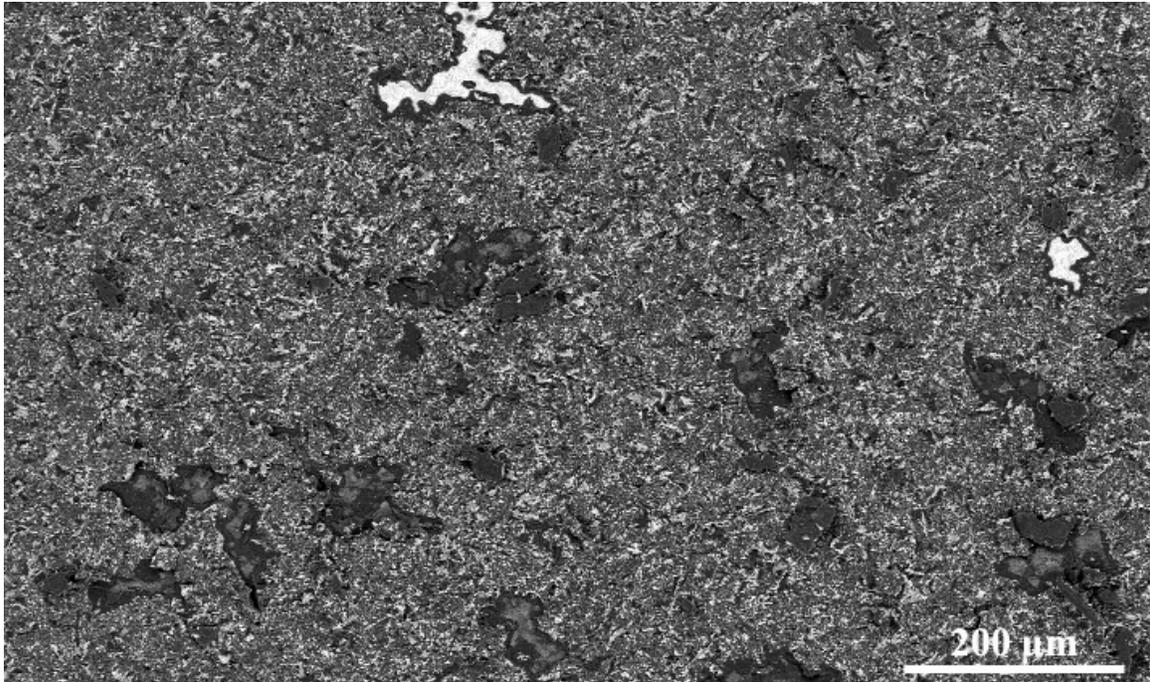
Figure 7.38 Substrate surface of Inconel 738 displays reoxidized surfaces, pointed by arrows.
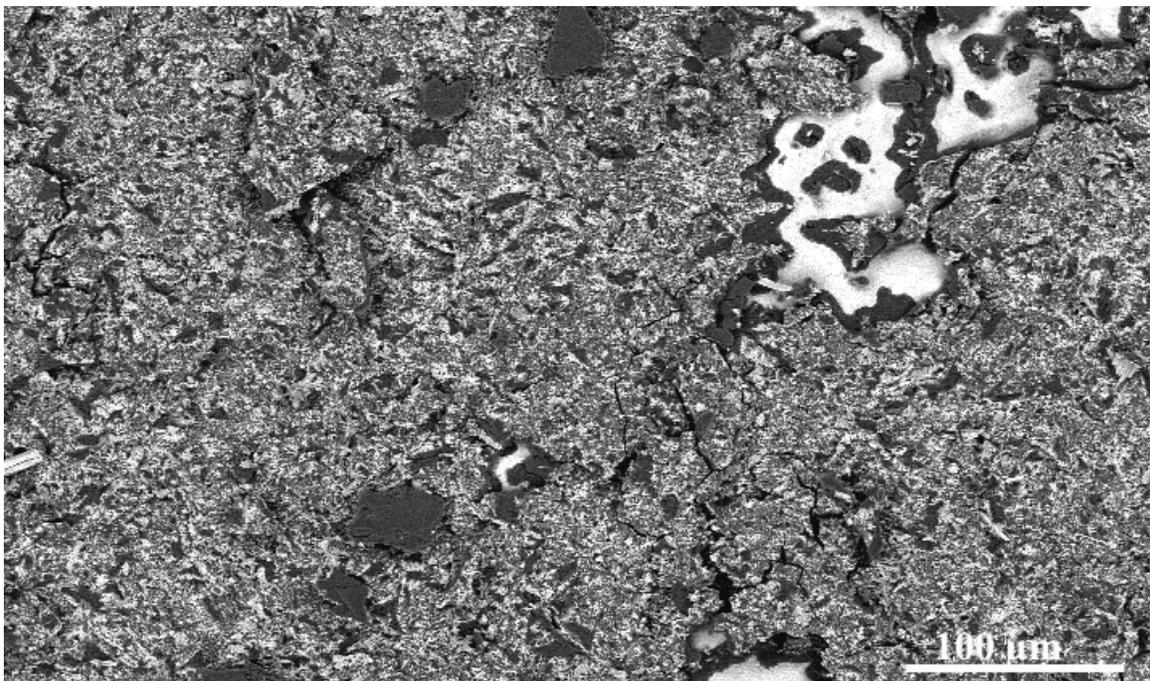
Figure 7.39 IN738 substrate surface contains cracks, spalled bare bond coat surfaces and holes.
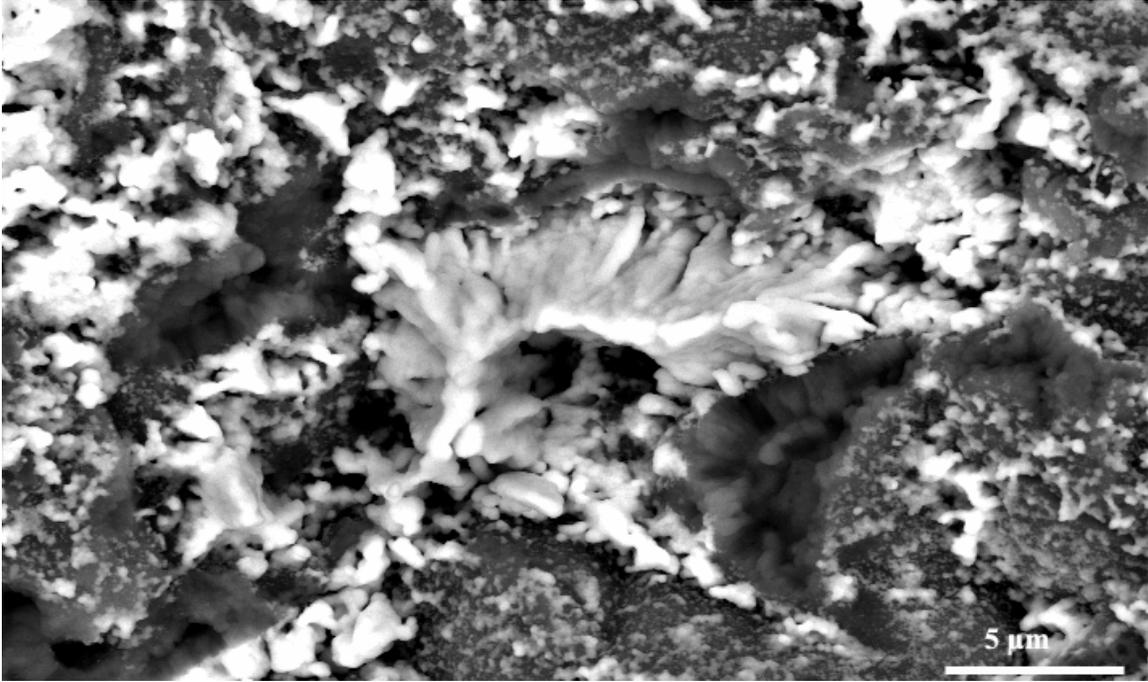
Figure 7.40 Holes on the surface of IN738, surrounded by YSZ grains.

Cross sectional view of Inconel 738, Figure 7.41, shows the failure occurred by ratcheting. Initially a weak interface is present at the TGO/YSZ interface, hence indicative of the failure type. In addition to the weak interface, there are also plenty of oxidized areas that extended into the bond coat, characteristic of the ratcheting effect seen in all of the specimens (see Figure 7.42). Different contrast intensity on these black and white images is indicative of phase composition differences, which is also present in this specimen, in Figure 7.43. For these specimens, unlike others there is not any martensitic phase present at the moment of failure; the only two phases present are γ' and γ. γ' is richer in Ti and Pt than γ by approximately two times, while γ is richer in Cr and Co. Small traces of Ta, W and Mo were found mostly near the interdiffusion area. The thickness of the TGO at failure coincides or approaches that of the other two specimens already reviewed (see Figure 7.44). Nevertheless, there seemed to be more areas without

TGO when looking at the cross section than for the other specimens. In retrospect, this coincides with the plentiful amount of bare areas. As for the interdiffusion area, it is possible to comment that it has the least dense interdiffusion area of all the specimens, which again can be seen from Figure 7.41. Precipitates found in the interdiffusion area are constituted mainly by Ti, Ta, Nb, Ni, Co, Cr, arranged in the order of their atomic concentration. Carbides were not observed, although it is expected that carbon segregated to the grain boundaries of the substrate. Carbon segregates to the grain boundaries to improve creep resistance.
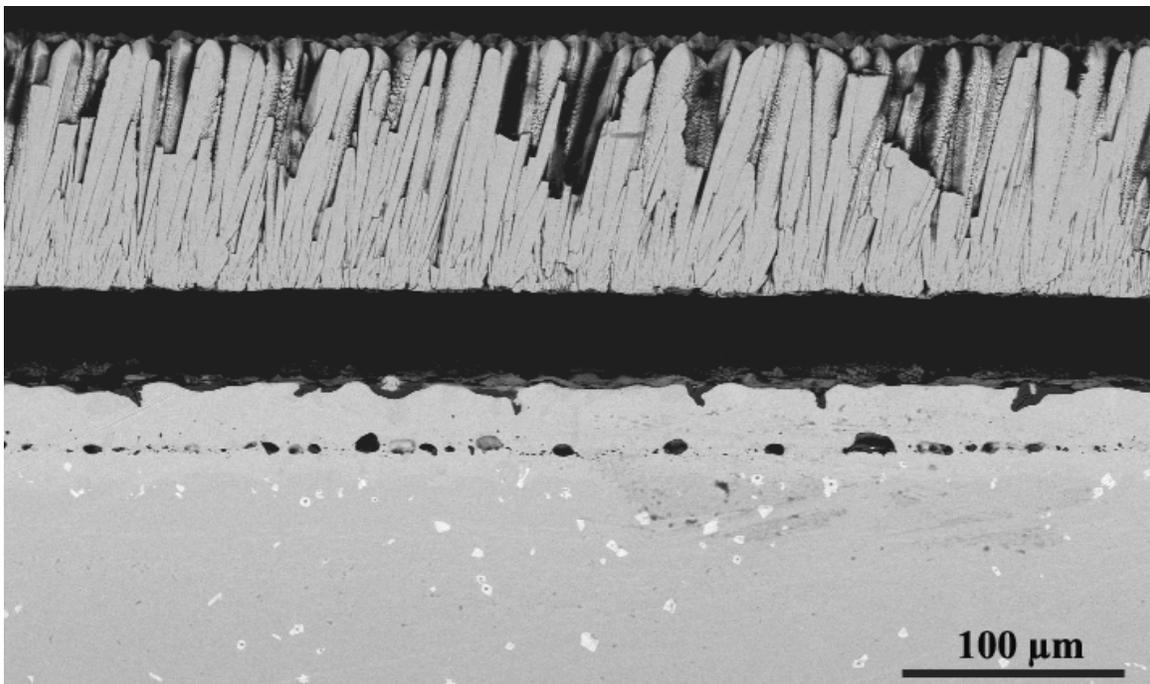
Figure 7.41 Cross sectional view of IN738 displays, YSZ/TGO weak interface, ratcheting mechanism, holes in the bond coat, and the interdiffusion area.
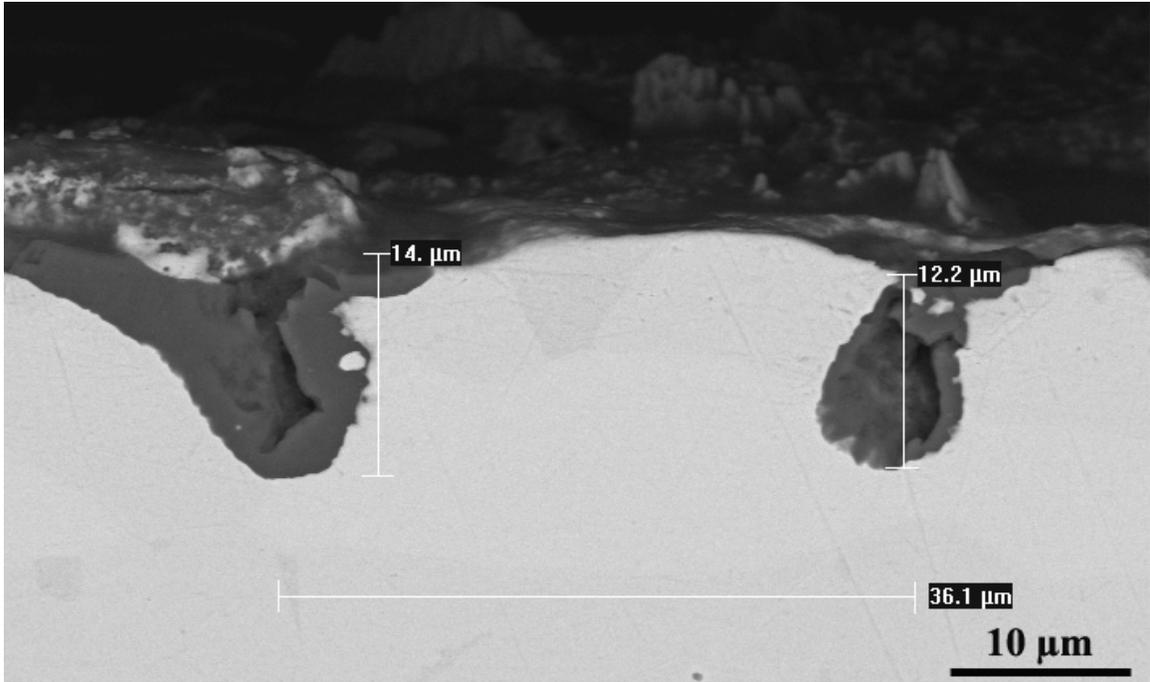
Figure 7.42 Bond coat of IN738 displays displays the failure mode of ratcheting.
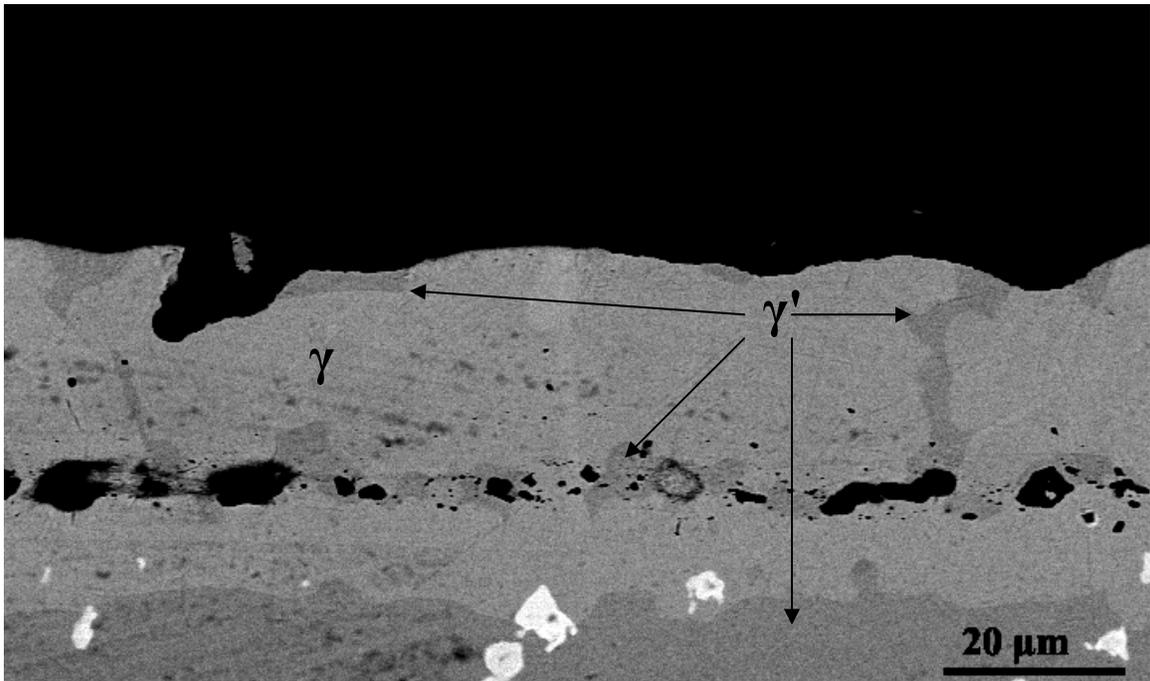
Figure 7.43 A closer look at phase distribution along the bond coat of IN738, displays γ and γ'.
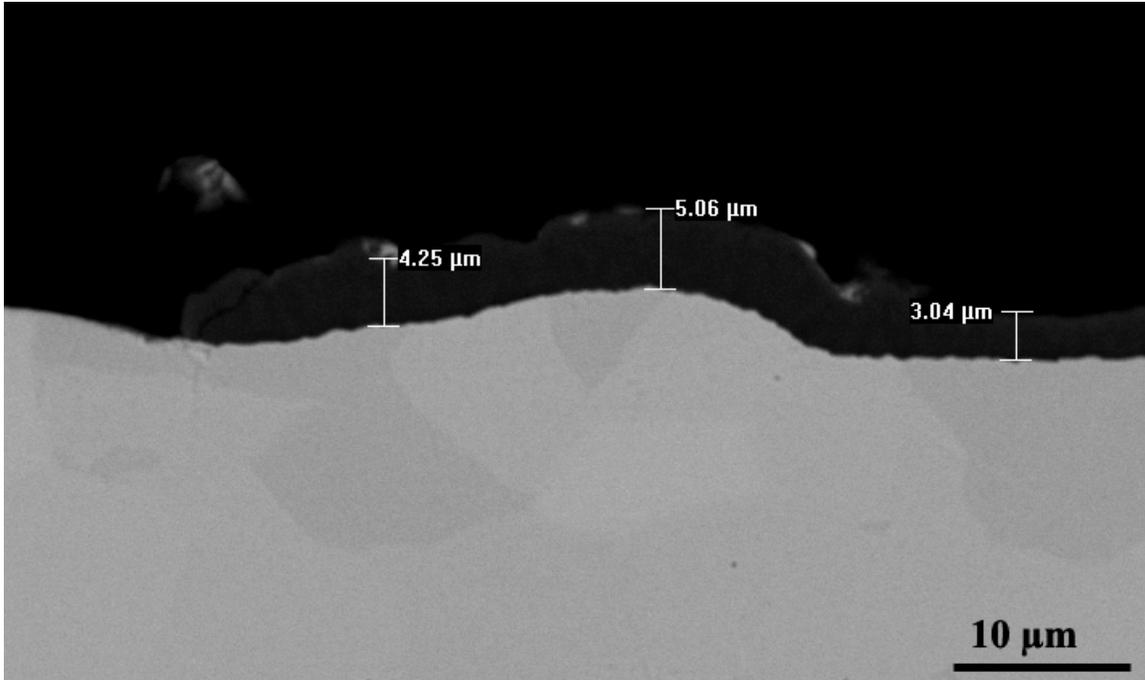
Figure 7.44 TGO thickness average on IN738 similar to N5; in addition, some bare areas also show on the cross section.

7.3 MID-CYCLE FAILURE

Mid-cycle failures include the range of alloys that failed between 39 and 64 percent of René N5. As seen earlier in Figure 7.1, this category includes three third generation nickel based superalloys, which are CE1, CE3, and CE8. CE1 had the highest mark in this category averaging 510 cycles per specimen or 64% of N5. CE3 and CE8 averaged 39% and 36% of N5, respectively. The specimens displayed martensitic transformation at the bond coat and a rougher bond coat surface than N5.

7.3.1 Performance of CE1

CE1, like all the other specimens, also failed along the YSZ/TGO interface. Figure 7.45 presents the YSZ failure surface of CE1. Like the high cycle failure specimens, CE1 has bits of TGO attached to the YSZ, as well as missing YSZ in certain areas. A closer look at these TGO bits in Figure 7.46, shows a porous surface as well as ragged edges. The substrate surface after failure resembled that of IN738, though less spalled, see Figure 7.47. In Figure 7.48, spalled areas as well as reoxidized areas and cracks all populate the same area, again similar to the substrate surface of IN738 after failure; additional holes are also present. Holes seem not to be in high density as previously seen in other substrate failure surfaces.
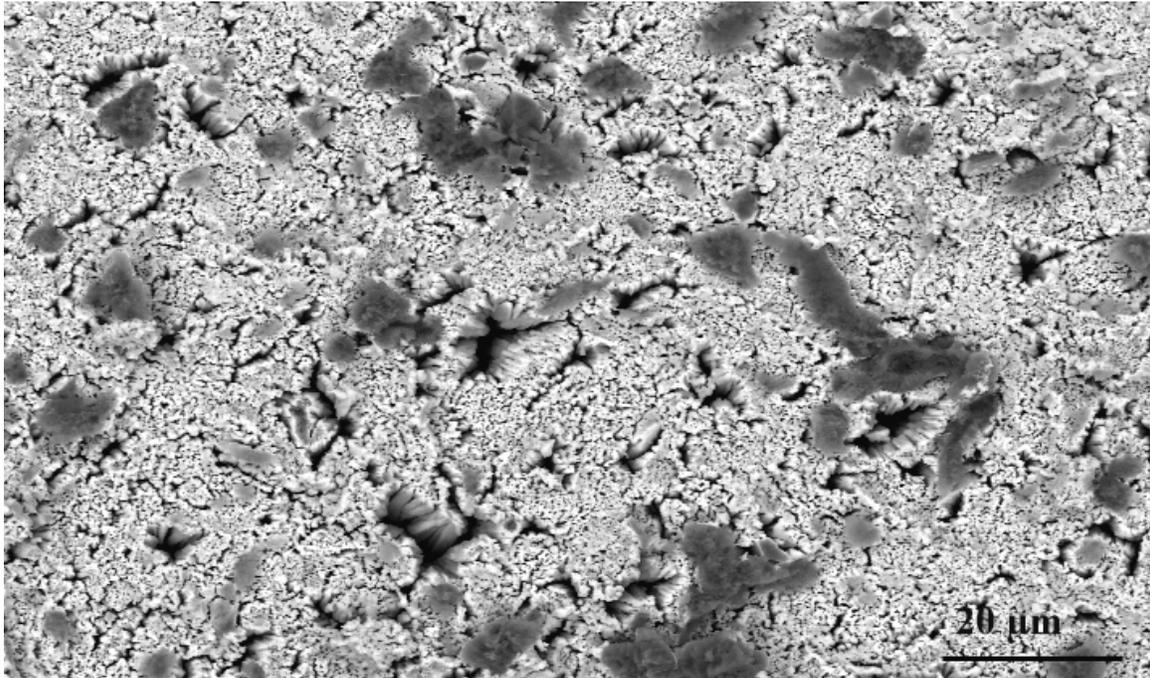
Figure 7.45 YSZ scale from CE1 displays bits of alumina, and missing YSZ.
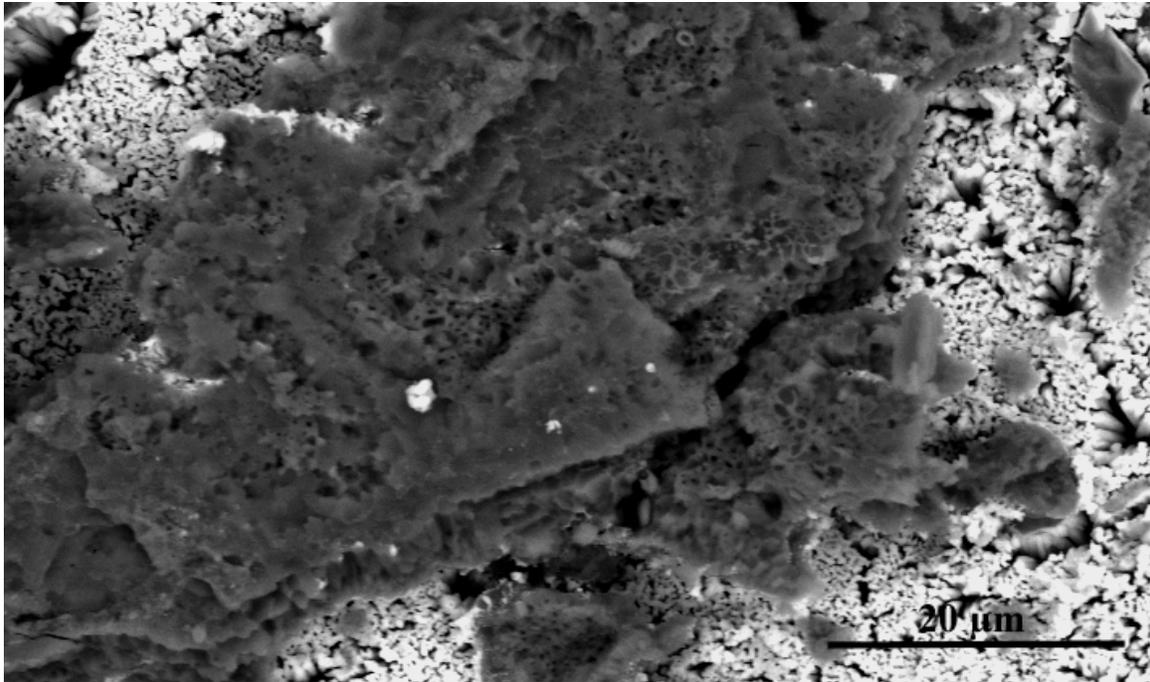
Figure 7.46 Alumina on YSZ of CE1 is large and porous.
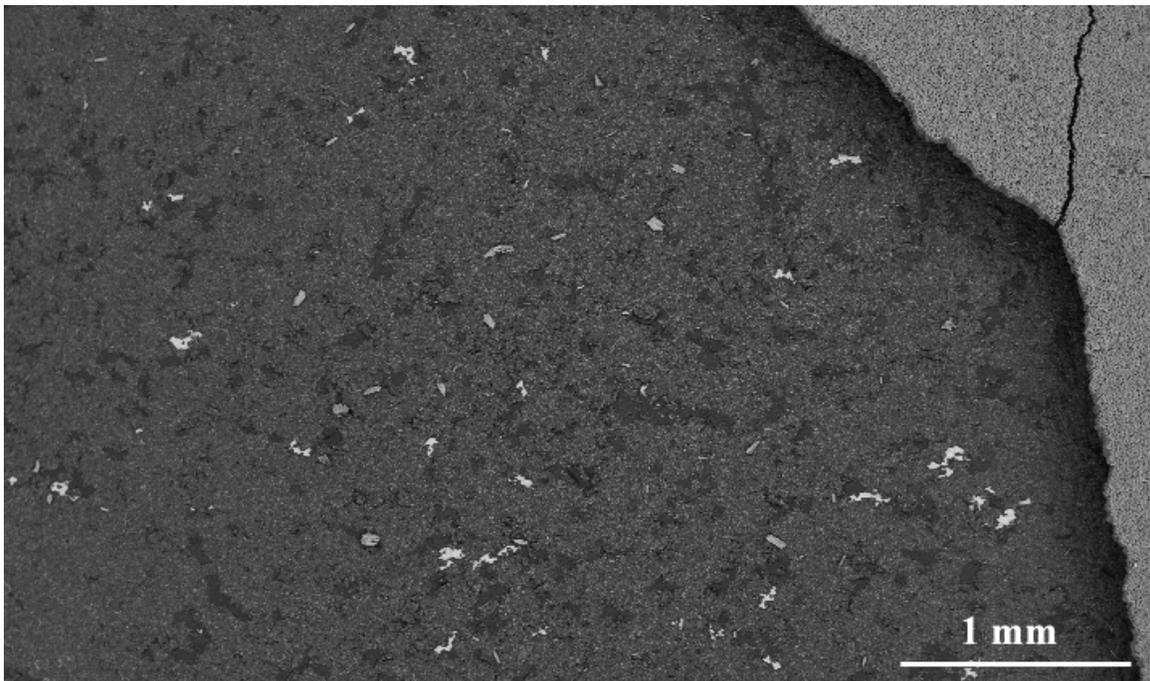
Figure 7.47 CE1 substrate surface displays areas from where the TGO has spalled as well as reoxidized spots.
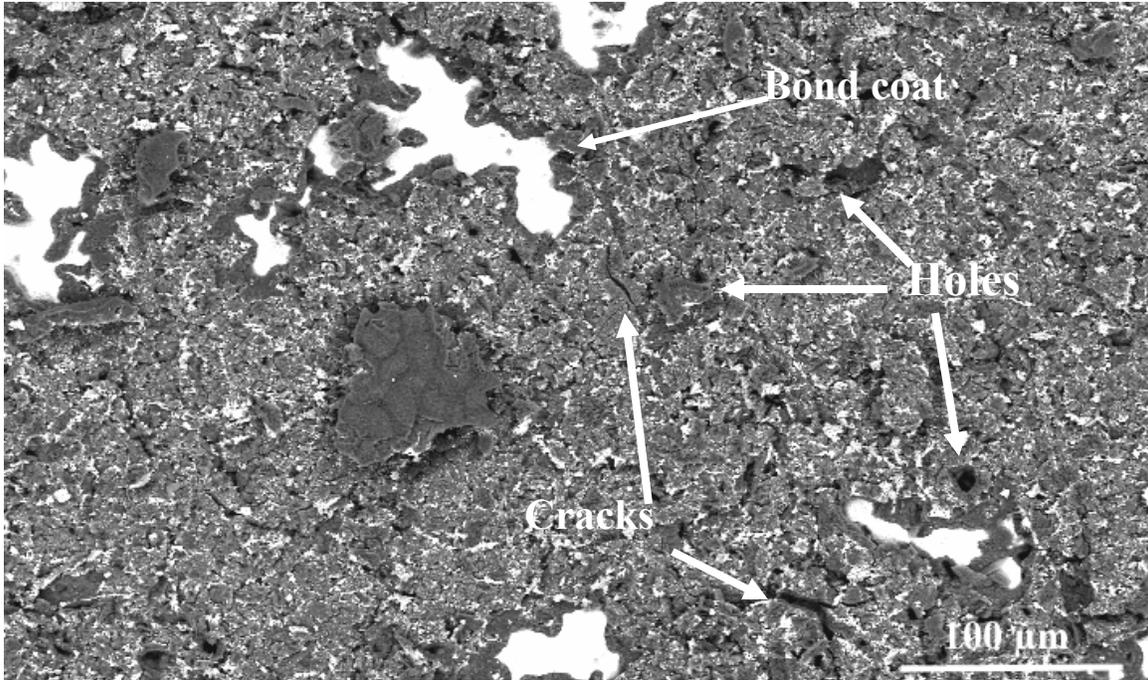
Figure 7.48 Magnification of CE1 failure surface shows TGO spalled areas, cracks, holes, and reoxidized areas.

The cross sectional view of CE1 revealed a similar behavior to that of the higher failure cycles, like N5. As seen in Figure 7.49, the bond coat cross section displays less sections of the oxides expanding into the bond coat and presents a more consumed bond coat than that of N5. Additionally, Figure 7.49 shows that TGO thickness exceeds that of previous superalloys. Furthermore, one can see the interdiffusion area and its geometrical shapes. Again, the shapes are in the form of circles and needles, as seen in the previous alloys. However, the density lies between IN738 and N5, considering that ME2 has the most dense interdiffusion area. The composition of these precipitates includes W, Re, Ni, Cr, Co, Mo, and Al for the globular shaped ones. Meanwhile, forming the secondary reaction zone, one sees the acicular shaped precipitates formed by Cr, Ni, W, Co, Re, and Mo. Figure 7.50 displays the thermally grown oxide at failure time. As seen in the figure, the thermally grown oxide cracks parallel to the YSZ/TGO

interface and not normal to the interface, as seen in the previous superalloys. Figure 7.51 also displays the unprotected area adjacent the thermally grown oxide with YSZ adhered to it. Again, Figure 7.51 additionally shows the thickness of the TGO and significant deformation of the bond coat without much increasing of the concavity of the oxide penetration. Moreover, Figure 7.51 also shows the phase distribution along the bond coat. As seen here, most of the bond coat has transformed to β' ($L1_0$) and some to γ'($L1_2$). Tantalum segregated to the gamma prime phase. Finally, Figure 7.52 shows the oxide extending into the bond coat and retaining YSZ.
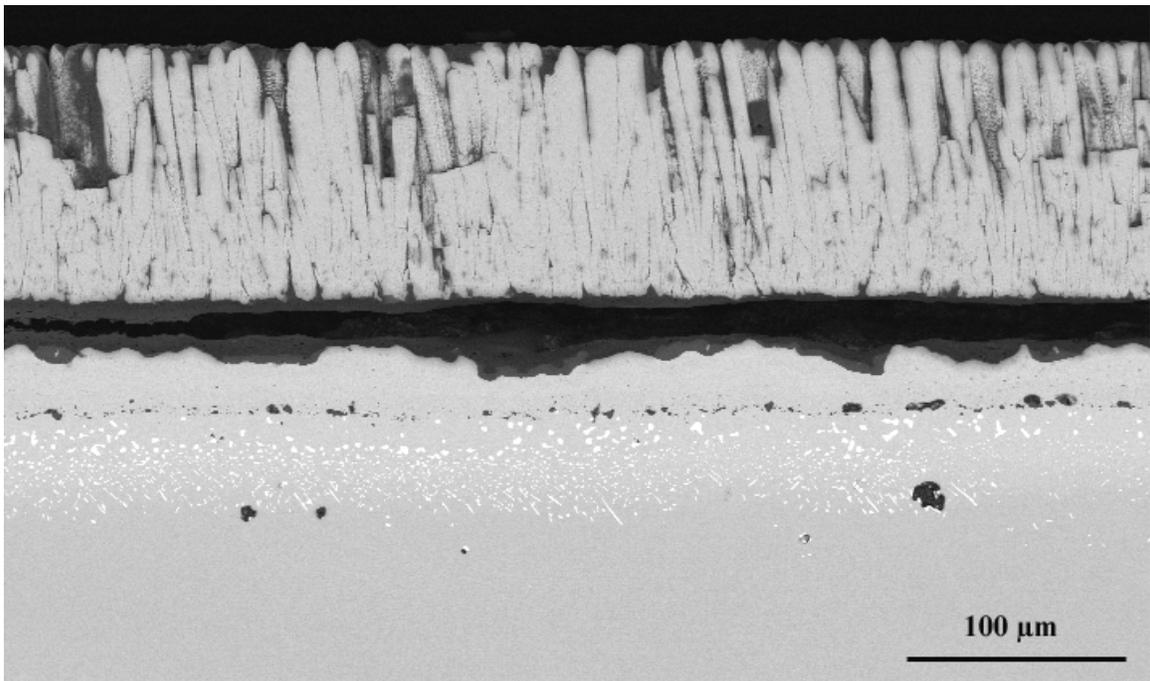
Figure 7.49 CE1 cross section after TBC failure along YSZ/TGO interface.
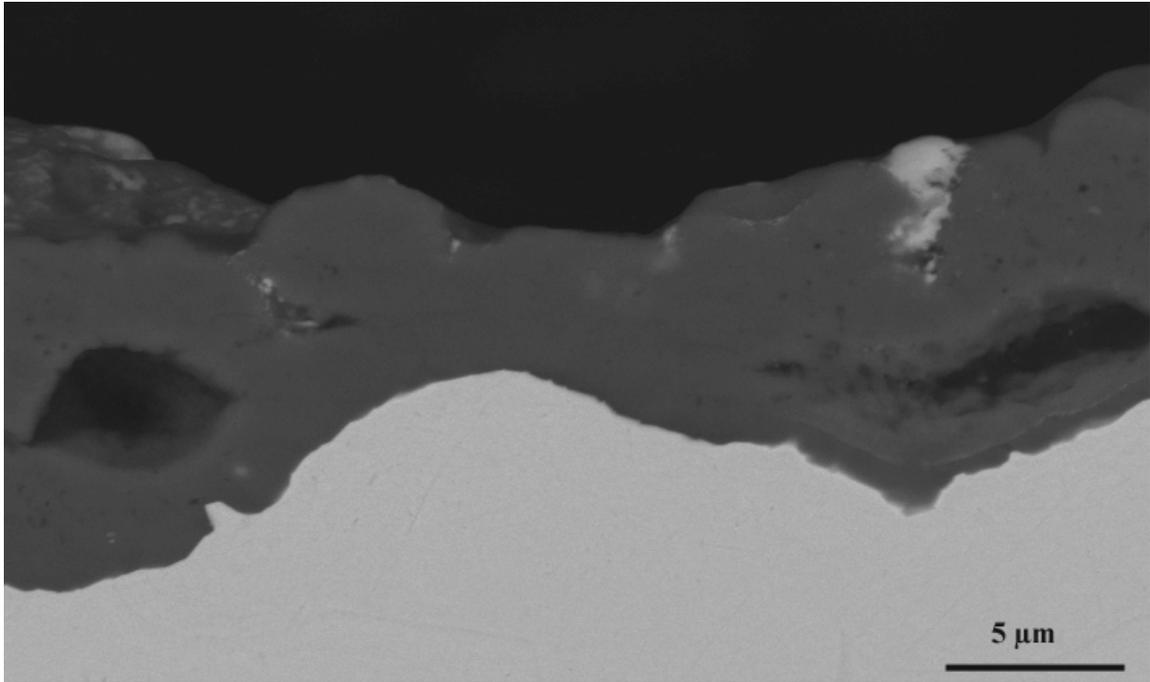
Figure 7.50 TGO thickness on CE1 substrate surface displays heterogeneous growth. Unlike previous deformations, TGO cracks propagate parallel and not normal to the YSZ/TGO interface.
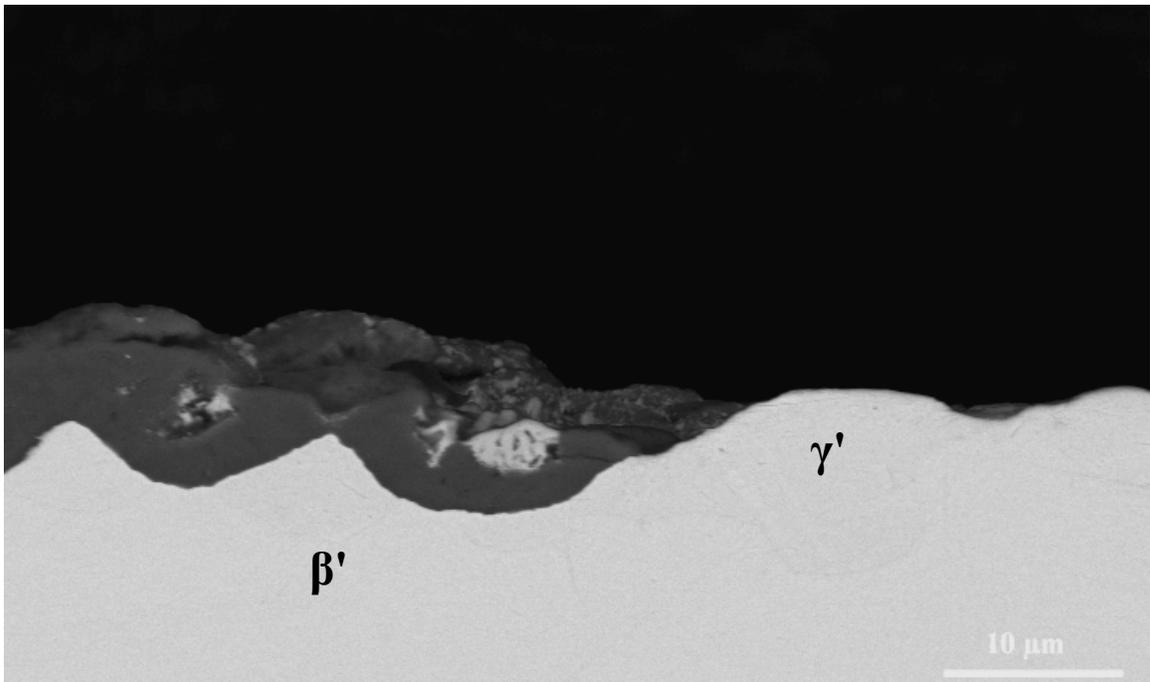
Figure 7.51 Bond coat remains unprotected after loss of TGO, while other areas are still protected.
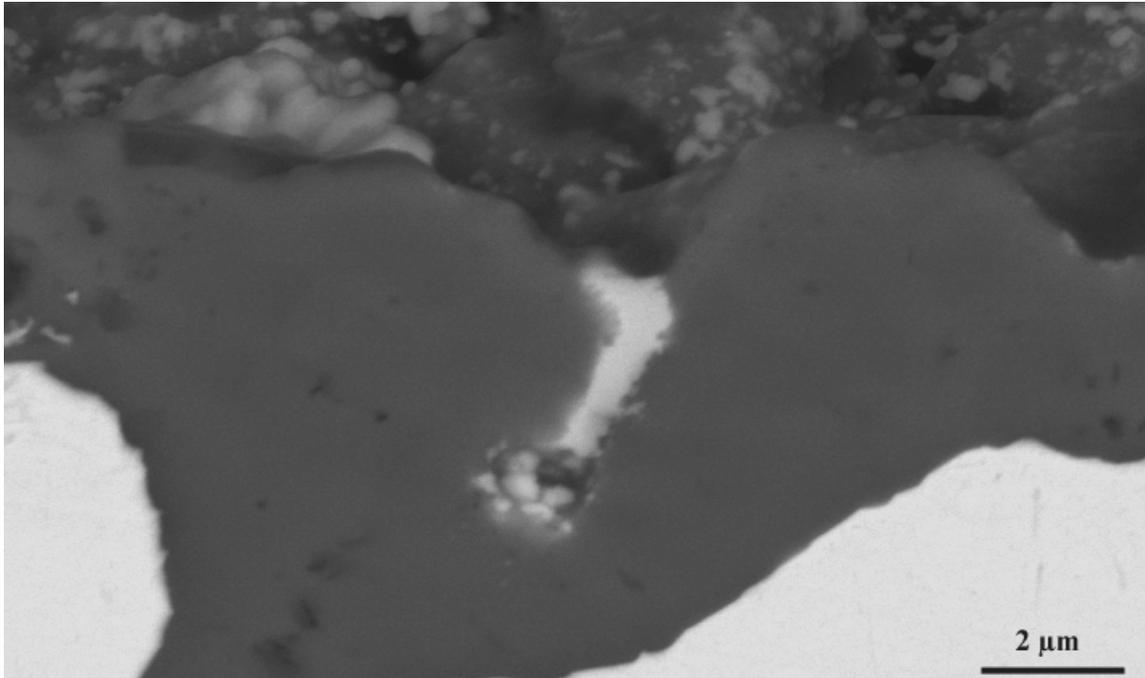
Figure 7.52 Oxide extends into bond coat and retains YSZ inside as seen in this figure.

7.3.2 Performance of CE3

The performance of CE3 specimens averaged 310 cycles or 39% of N5s total

average. As seen in Figure 7.53, the failure of the TBC system occurred along the

YSZ/TGO interface. Like the rest of the previously discussed specimens, subject to the

ratcheting failure type, there is attachment of some TGO on to the YSZ surface and vice

versa. Figure 7.54, shows a micrograph of an alumina bit attached to the YSZ surface.

In addition to the TGO in Figure 7.54, there is also the presence of holes on the YSZ

surface as well as cracks. Figure 7.55 shows the substrate surface which is protected by

the TGO. Unlike the previously seen specimens, CE3 does not show any spallation at the

TGO/BC interface nor reoxidation surfaces. These characteristics could be seen in

Figure 7.55 and 7.56. Nevertheless, other not yet seen features do appear on the failure

surface of the substrate, including the formation of a button like precipitate whose

composition includes Al, O, Ta, Ni (see Figure 7.56). Some holes are also seen in Figure

7.56 accompanied by cracks and YSZ debris from the detachment of the systems

components. A closer look at the features seen on top of the substrate is seen in Figures

6.57 and 6.58, which show magnifications of a crack and grains adhering to the TGO

after failure, respectively.
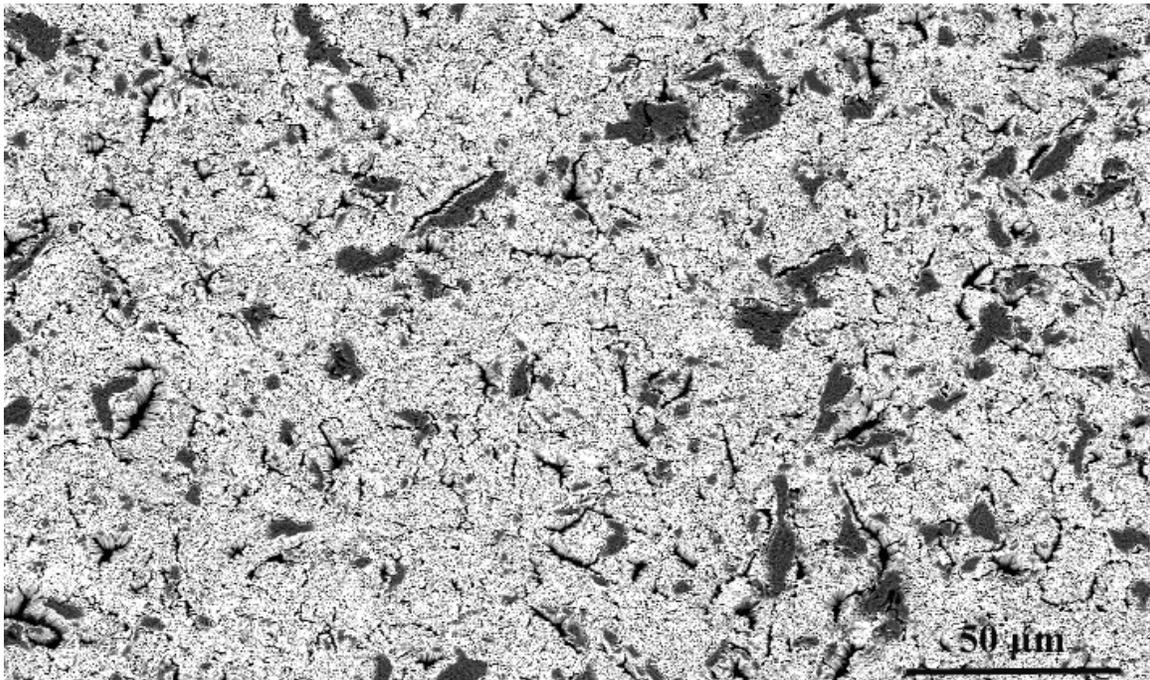
Figure 7.53 YSZ failure surface of CE3 shows similar failures of other substrates in the study, YSZ/TGO interface failure.
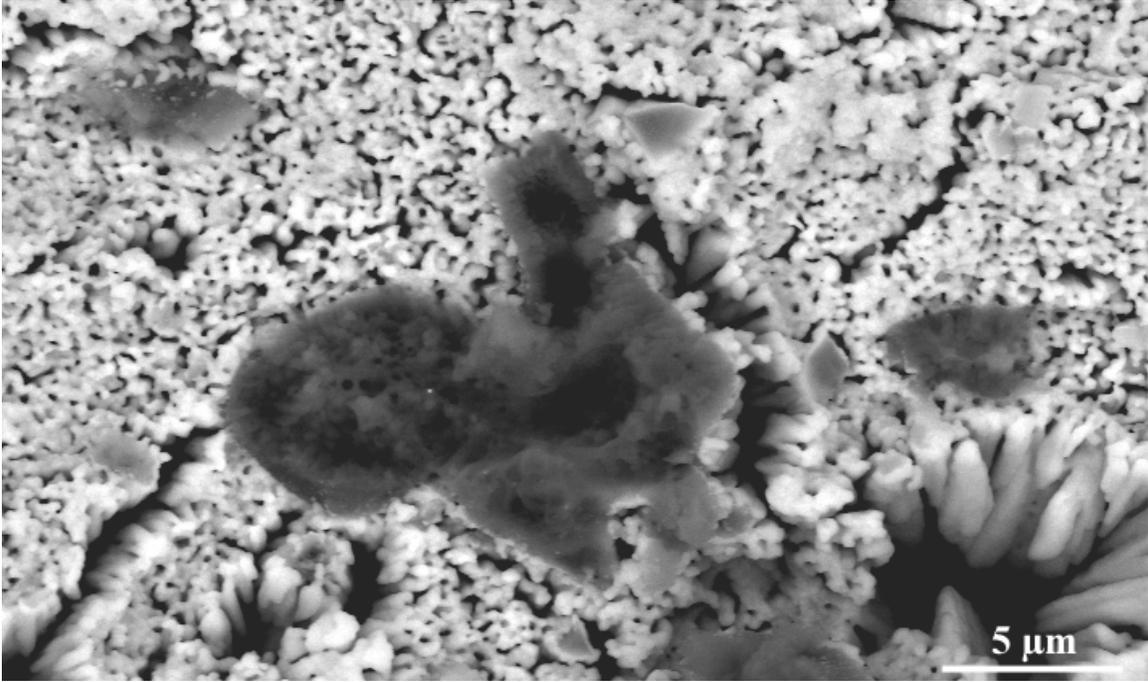
Figure 7.54 TGO bits on the YSZ failure surface accompanied by holes and cracks on the surface.
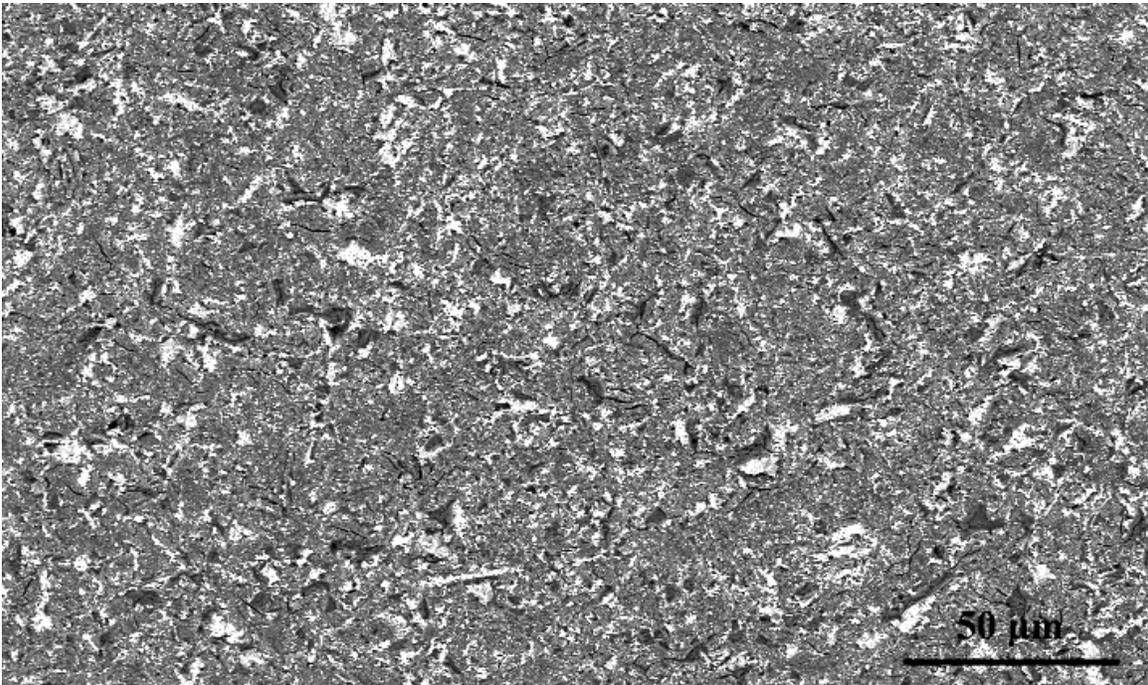
Figure 7.55 CE3 substrate failure surface elucidates on the failure type, and failure traits.
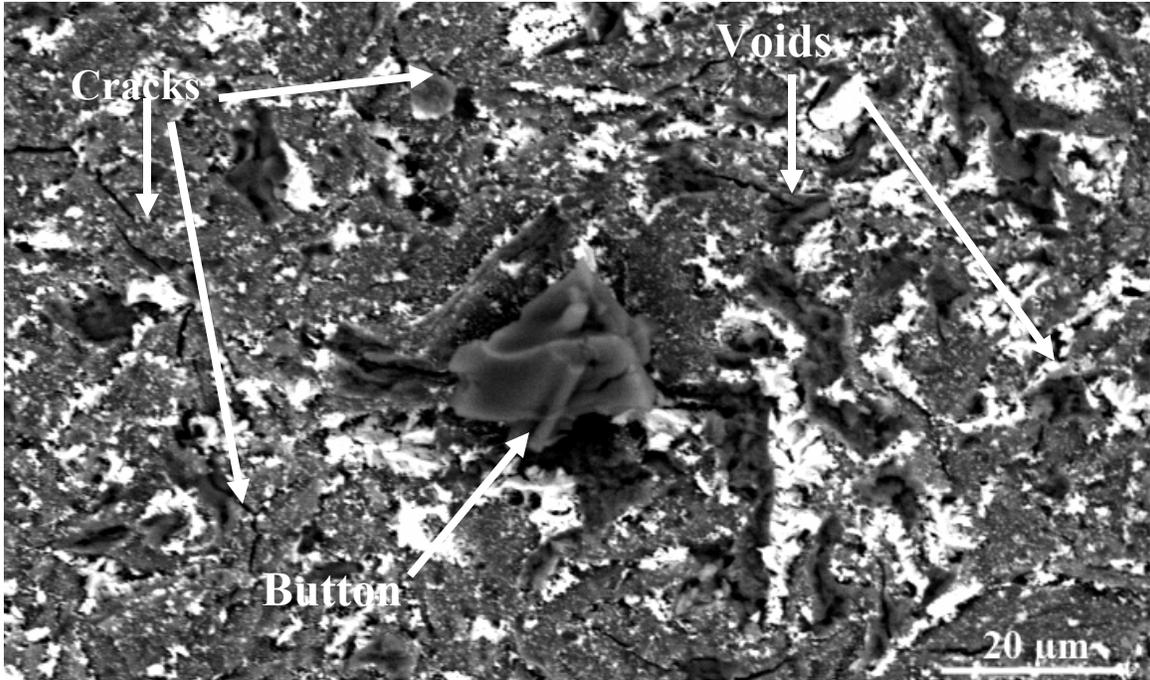
Figure 7.56 Substrate failure surface of CE3 displays cracks, YSZ and perforations, as well as oxidized buttons.
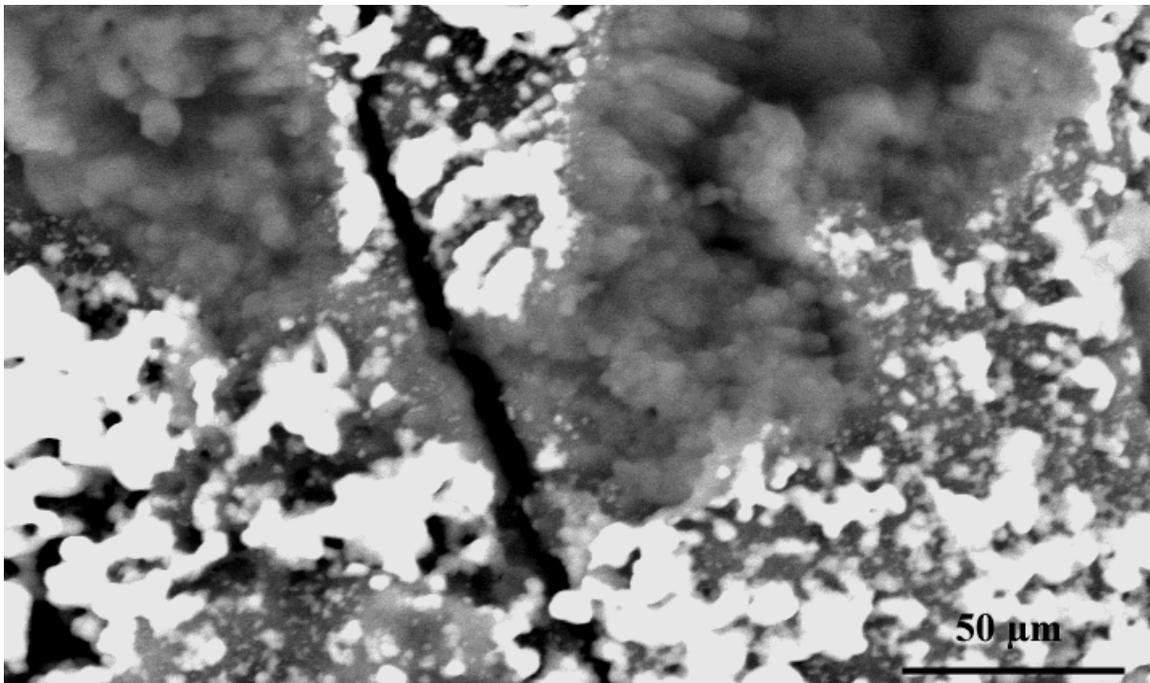
Figure 7.57 Crack propagation on the surface of CE3 at failure expands for over 50 µm.

Figure 7.58 YSZ grains attached to the TGO on the substrate surface after failure.

The cross section of this specimen also shows a very pronounced contrast between the martensitic phase and the $L1_2$ phase in the bond coat. Figure 7.59 displays the ratcheting mechanism which leads to the failure of all CE3 specimens. Additionally, it also displays an interdiffusion area that is not as dense as that of the high cycle failure specimens. Alumina particles are also seen as part of the CE3 bond coat, right above the interdiffusion area. Figure 7.60 displays the thickness of the TGO which did not exceed that of N5 or any of the substrates already presented. The TGO thickness is about 4μm and is about standard among all the specimens tested. Figure 7.60 also shows the martensite and $L1_2$ phase creating an interface with one another and the thermally grown oxide; tantalum is also found to segregate to the gamma prime phase.
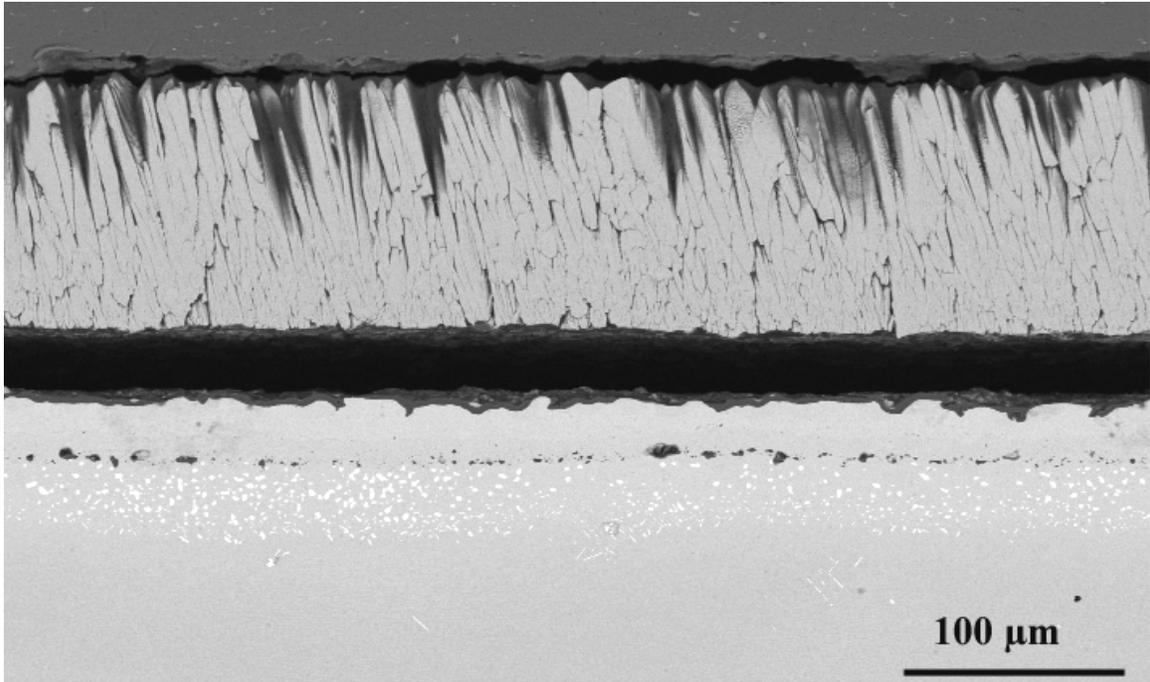
Figure 7.59 Cross section CE3 shows the interdiffusion area, ratcheting effect, and alumina particles in the bond coat.
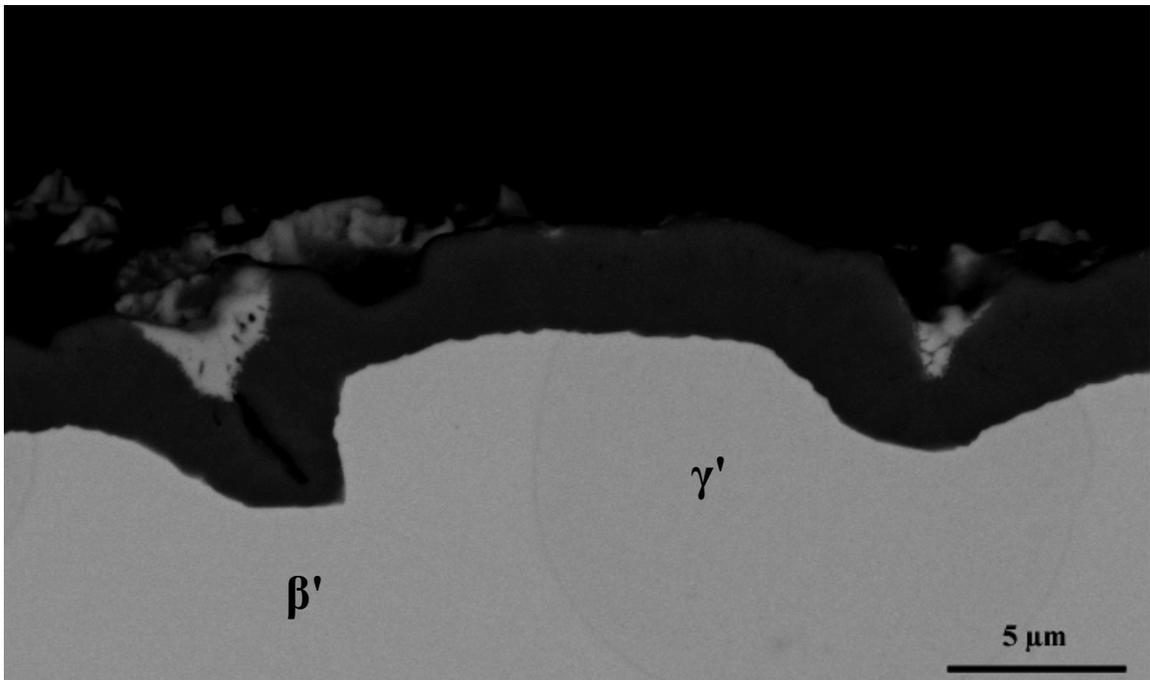
Figure 7.60 TGO thickness on the bond coat of CE3 did not exceed 4 μm. Additional is the presentation of the β' and the γ' phases.

7.3.3 Performance of CE8

The failure of this TBC system occurred along the YSZ/TGO interface, as seen in Figure 7.61. Again, thermally grown oxide portions remain on the failure surface of the YSZ, as seen in Figure 7.61 and Figure 7.62. Other features of this failure mechanism include the loss of YSZ, creating holes and/or cracks on the YSZ, as seen in Figure 7.63. The failure surface of CE8 shows cracks, holes and YSZ that remained attached to the TGO after failure of the TBC system, as seen in Figure 7.63. Not representative of the CE8 specimens is the spallation of the TGO from one specimen, allowing for reoxidation and/or complete exposure of the bond coat to the environment, as seen in Figure 7.64. This last figure is from a specimen that underwent 380 cycles. Figure 7.65 is a close up of the holes and cracks seen on the CE8 failure surface.
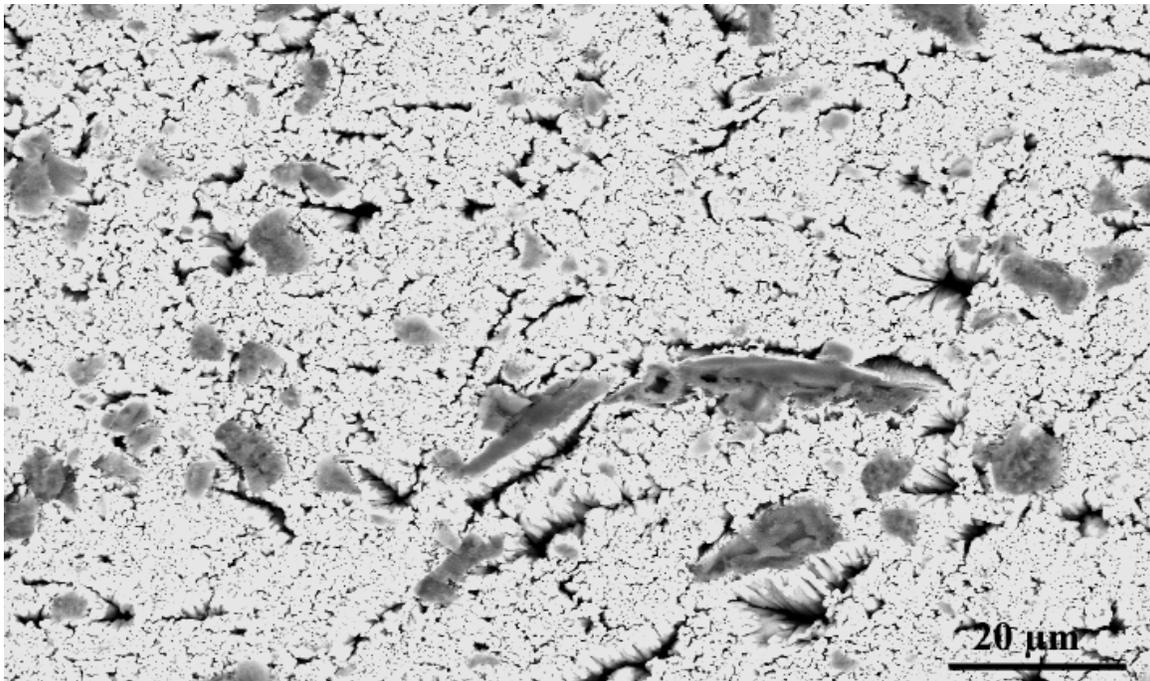
Figure 7.61 The YSZ failure surface from a CE8 specimen.
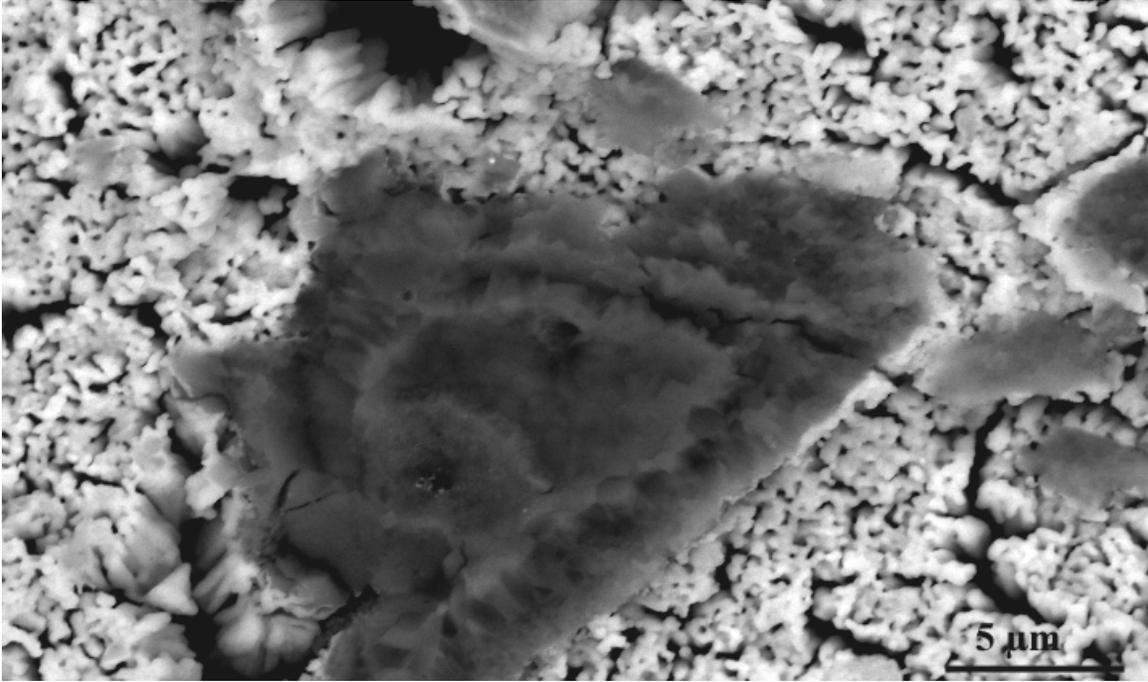
Figure 7.62 Thermally grown oxide, holes, and cracks on the YSZ failure surface of a CE8 specimen.
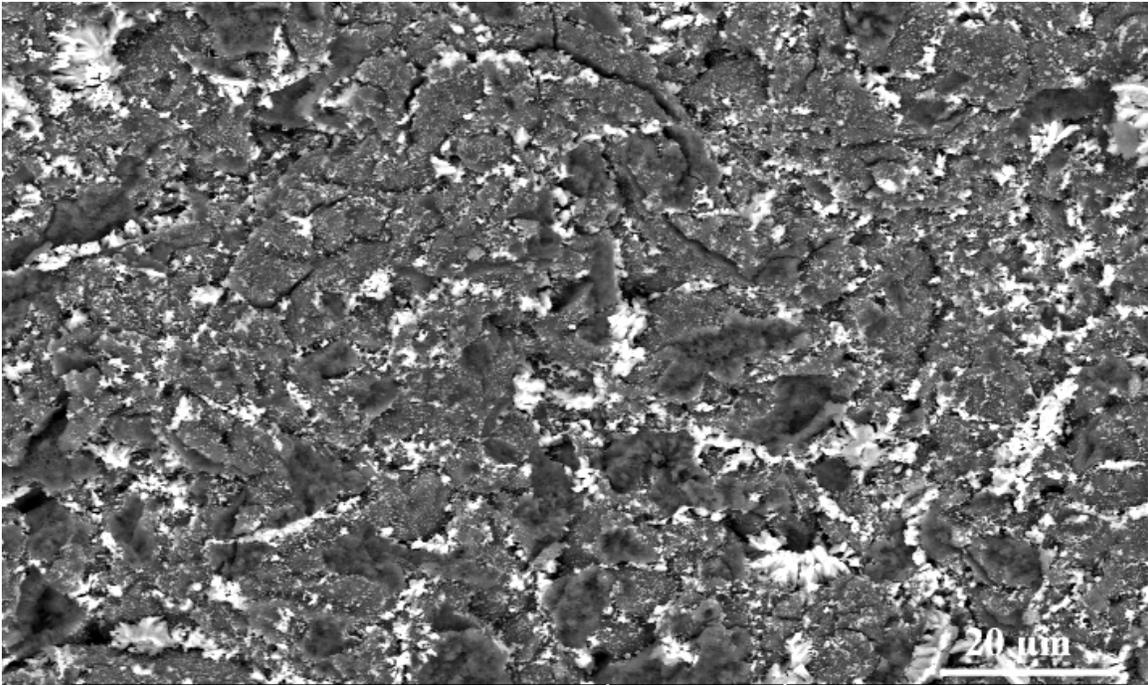
Figure 7.63 TGO failure surface from a CE8 specimen, showing holes, cracks and YSZ remains.
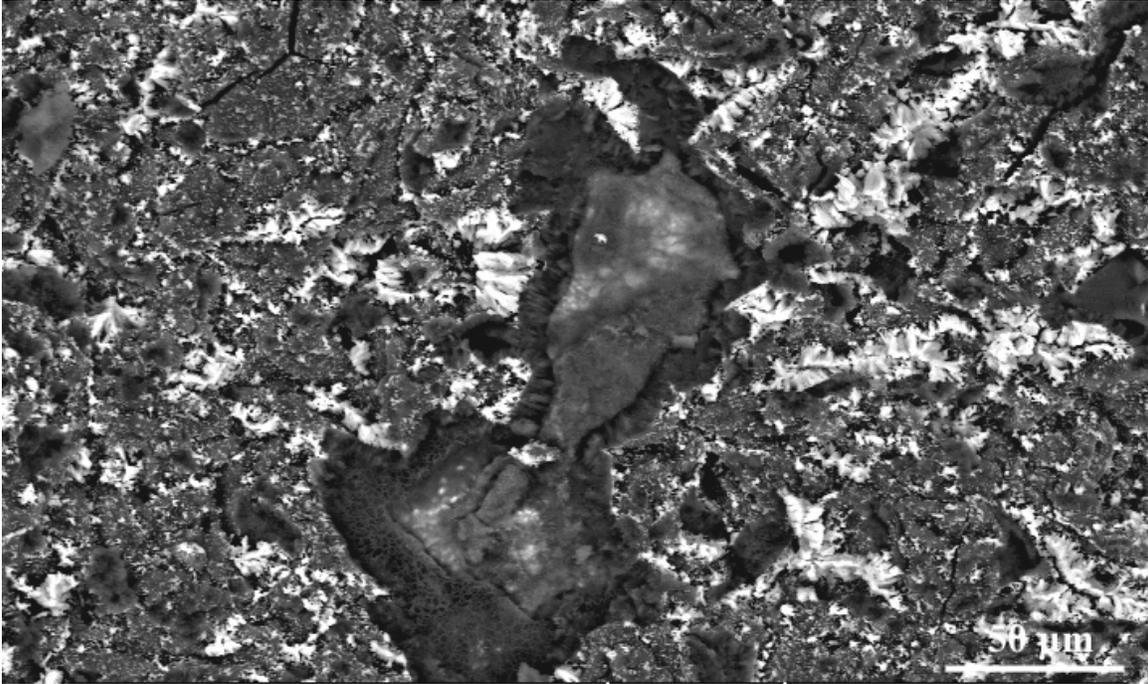
Figure 7.64 Reoxidized area seen only once on a CE8 specimen, other specimens did not show a bare or reoxidized area at all.
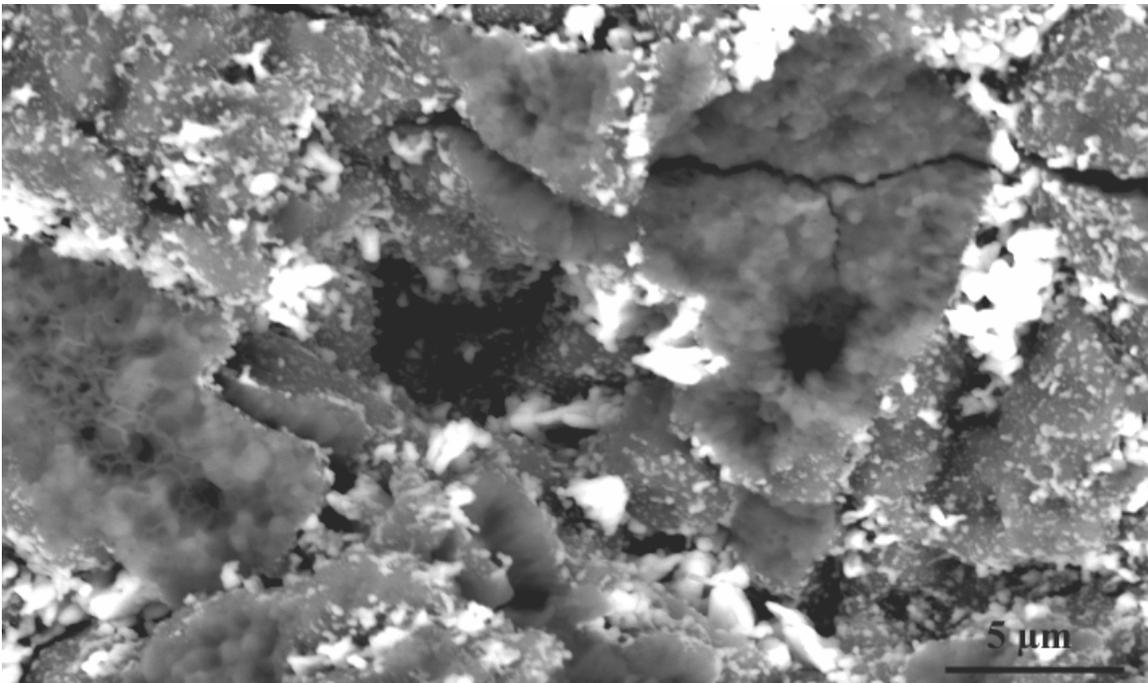
Figure 7.65 A closer look at the cracks and holes populating the TGO failure surface from a CE8 specimen.

A cross section representing the CE8 system is seen in Figure 7.66. Here it is possible to see that a weak interface between the YSZ and the TGO leads to failure. Moreover, the ratcheting effect is also seen to affect these specimens. The interdiffusion area also seems very dense, and involves the formation of Tantalum-Carbides. Other precipitates included are those seen in N5, ME2, CE1, and CE3. The TGO thickness did not exceed 4μm and can be seen in Figure 7.67. Another feature that is visible is the attachment of YSZ grains on the TGO after failure of the TBC system, see Figure 7.68. Figures 6.67 and 6.68 both display martensitic and gamma prime phases seen on the bond coats of the TBC system at failure. Some tantalum is found in the present martensitic phases. Nevertheless, the Ta concentration detected in the gamma prime phase is not as high as those found in the higher failure specimens.
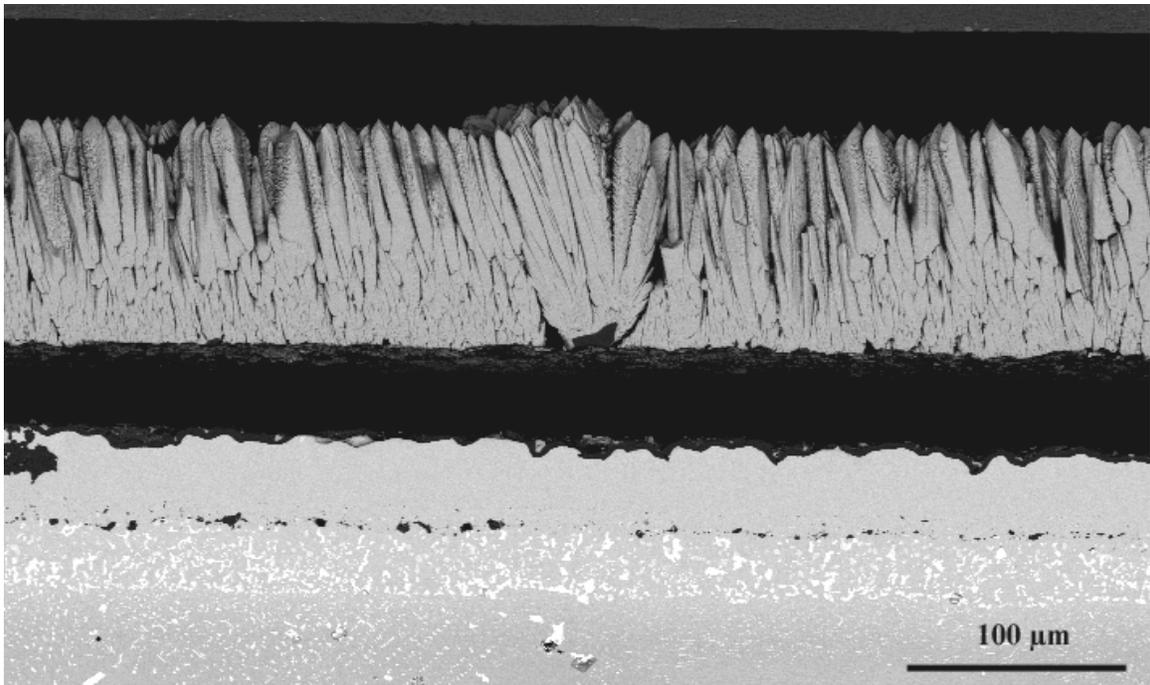
Figure 7.66 Cross section of the TBC system from a CE8 specimen after failure. Observe the rough surface, interdiffusion area and YSZ defect.
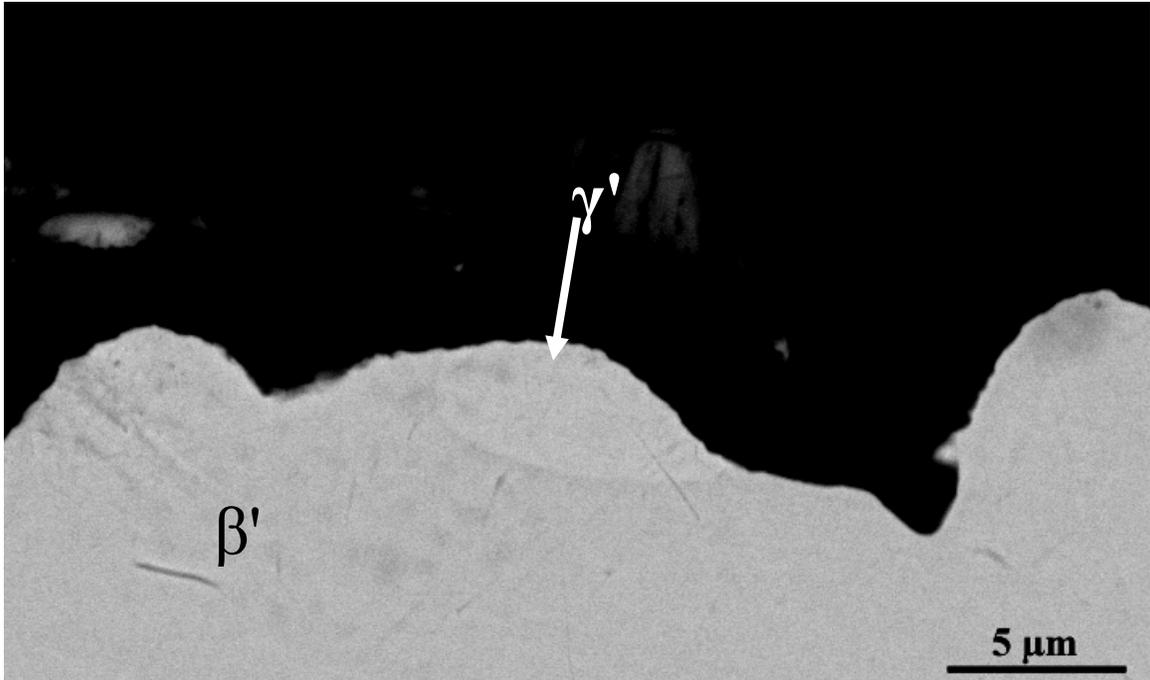
Figure 7.67 Ratcheting mechanism present in failure of CE8 specimens; noted in the back grains of the YSZ top coat. Martensite and gamma prime also present.
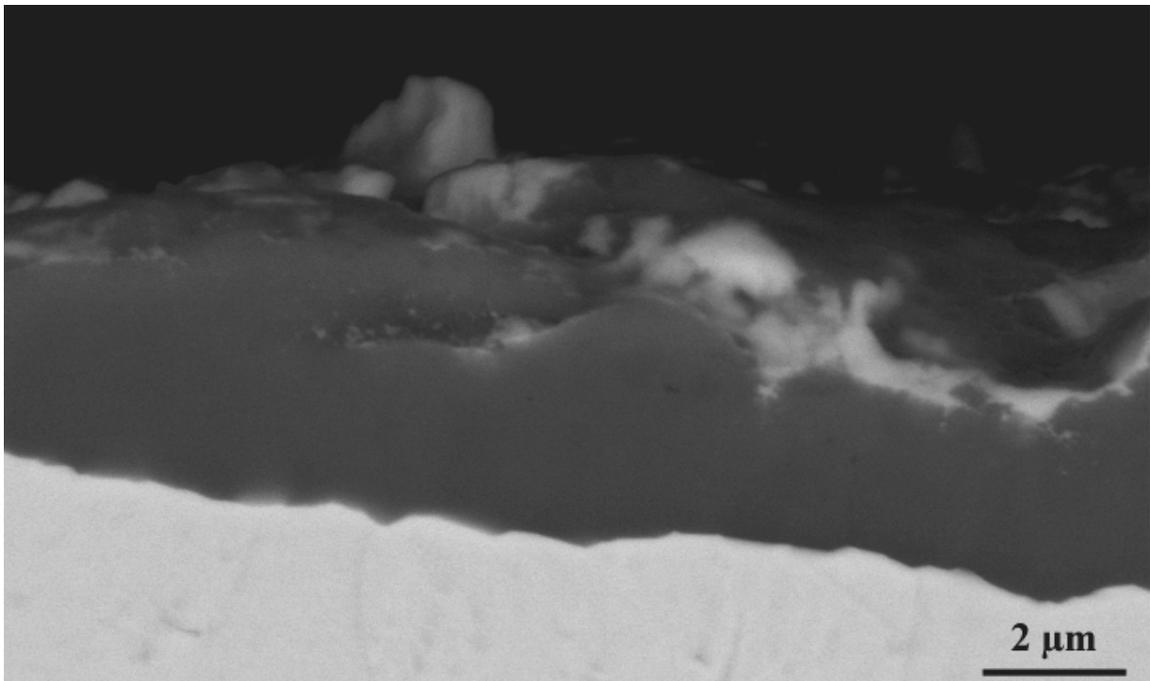
Figure 7.68 Thickness of the TGO did not exceed 4 μm. Martensite and gamma prime are also present.

7.4 LOW CYCLE FAILURE SPECIMENS

The last substrates to be reported in this study failed at percentages below 15% of N5. These alloys also contain carbon, a factor that precipitates the formation of Tantalum carbides. Not much is seen in the cross section of these substrates, with respect to bond coat phase transformations. The TGO thickness also remains below that of those that failed at higher cycles. The surface areas of the YSZ and the substrate show a clear and defined surface, which includes the YSZ and TGO interface. There are not any spalled surfaces which show the bare bond coat.

7.4.1 Performance of ME13

Specimens of the ME13 type failed at an average of 110 cycles per specimen or 13% of N5s total cyclic life. As seen from Figure 7.69, the failure of the TBC system occurred along the YSZ/TGO interface. The failure allowed for the retention of the TGO on the YSZ, while some YSZ also remained on the substrate protected by the TGO. Numerous holes were observed, even more so than for any of the mid range specimens or the high range failure specimens. The holes show traces of Ni, along with Al and O, nervertheless, it is not any sort of spinel. The second figure shows the attachment of the TGO onto the surface of the YSZ interface where it failed (Figure 7.70). Figure 7.71 shows a low magnification micrograph of the failure surface at the substrate, noting the YSZ as white area, gray areas as the alumina, and dark spots as the holes which develop in the surface. Figure 7.72 shows a high magnification micrograph of a group of YSZ grains that have been detached from the YSZ scale during deformation of the bond coat.
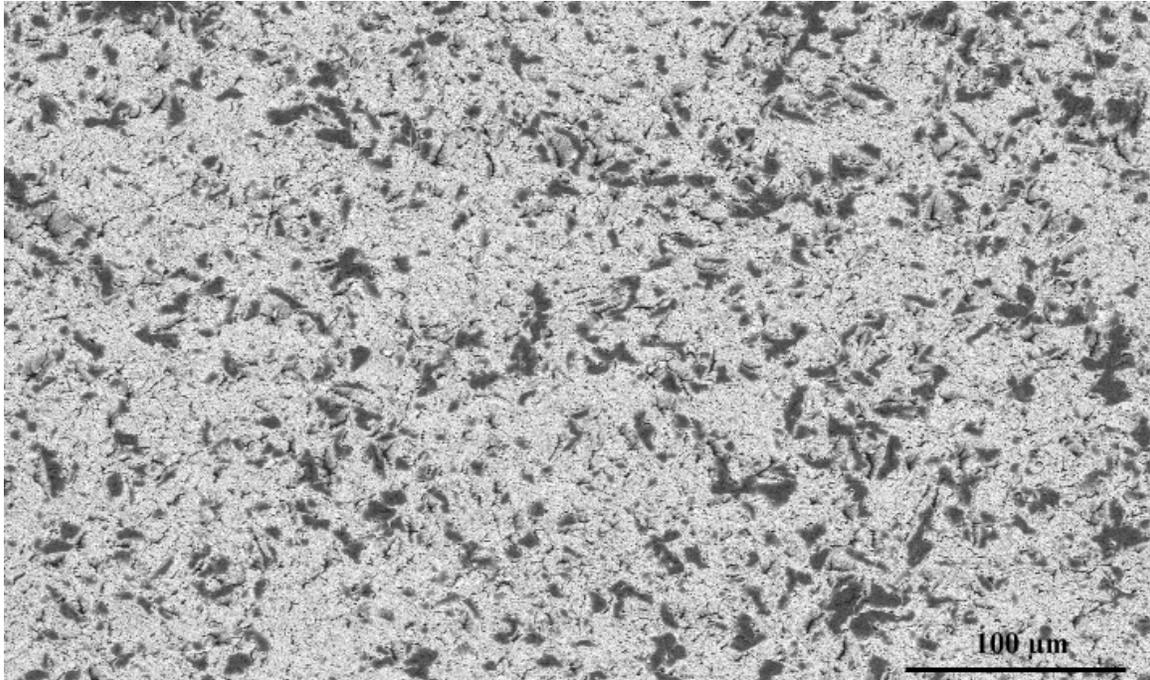
Figure 7.69 Standard failure surface of the YSZ from a ME13 specimen, dark area is the TGO and light area is the YSZ.
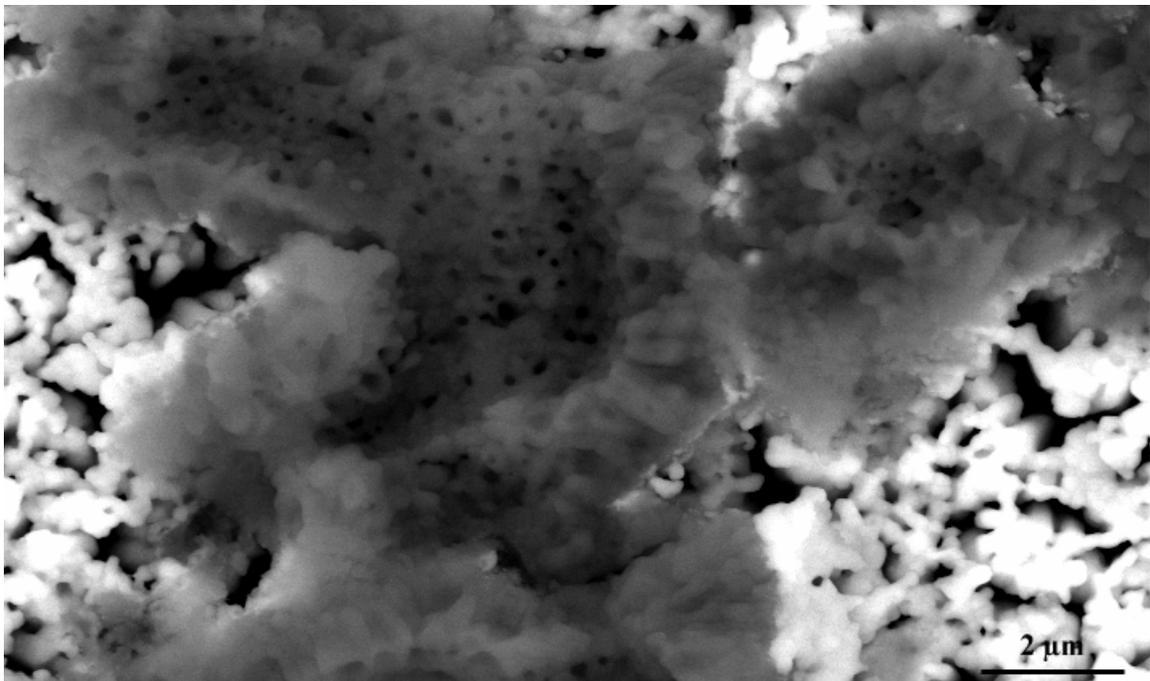
Figure 7.70 TGO bit on the YSZ surface after failure of a ME13 specimen.
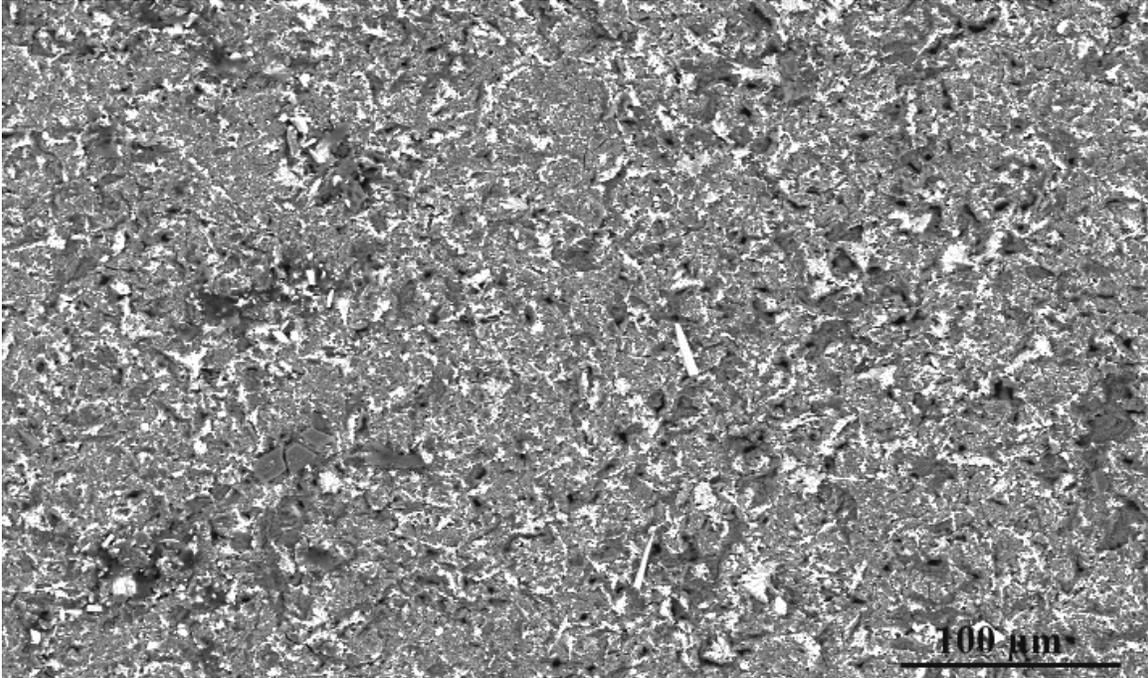
Figure 7.71 Failure surface of the substrate elucidates on the numerous holes, as well as the YSZ debris on the TGO, note there are not any spall areas.
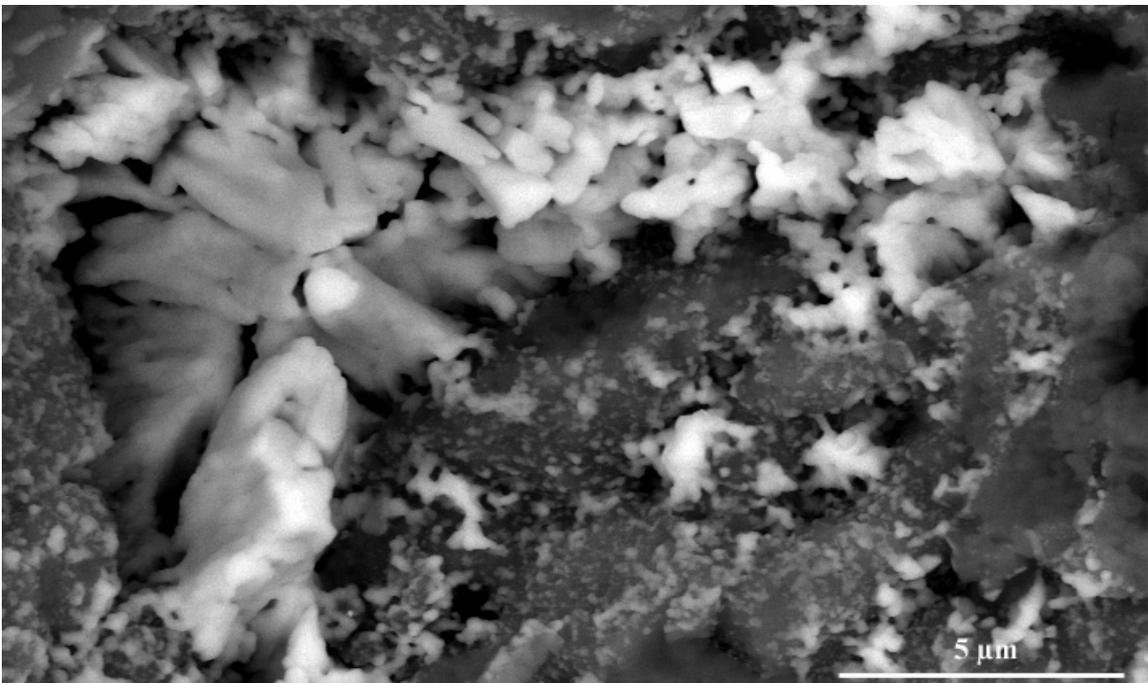
Figure 7.72 YSZ grains are swallowed by the TGO during deformation.

The cross sectional area of the specimens reveal a few features that are not clearly seen in the other specimens. Figure 7.73 shows the ratcheting mechanism which leads to the failure of the TBC system, deforming the bond coat surface even more and creating a weak interface for the YSZ and the TGO. A closer look in Figures 6.74 and 6.75 display the thickness of the TGO which does not exceed 3.5 microns. The micrographs also elucidate on a feature seen in mid-cycle failure specimens, an intra-TGO crack parallel to the YSZ/TGO surface. Additionally, numerous cracks also seem to propagate from the YSZ absorbed by the TGO where a interface occurs. The interdiffusion area (see Figure 7.76) is very similar to that of ME2, presenting a high density of precipitates formed by Re, Cr, W, and unlike ME2, tantalum carbides, identified by energy dispersive spectrometry. It should be noted that the lowest performers all formed tantalum carbides. The phase composition of the bond coat is mainly martensitic with a portion at the bottom formed by gamma prime with very little tantalum. Nevertheless, gamma prime does not have an interface with the TGO. Also visible is a very large amount of alumina particles, probably remains of the grit blasting process.
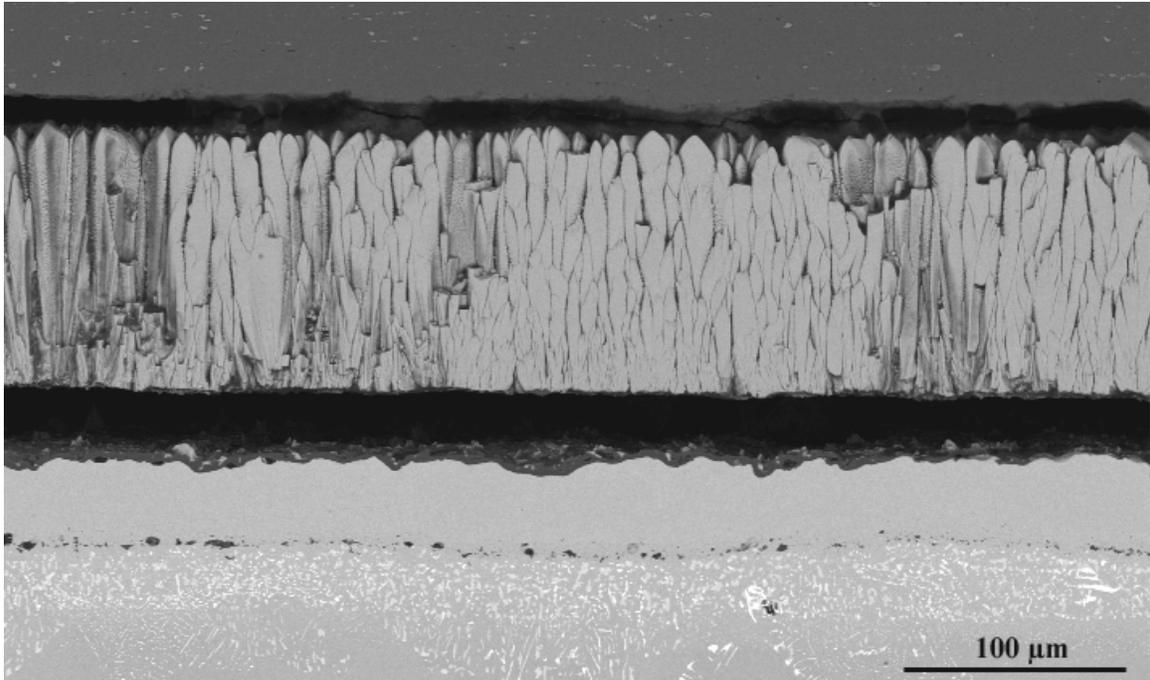
Figure 7.73 Cross sectional micrograph of ME13 shows ratcheting effect, bond coat, interdiffusion area and alumina particles in the bond coat.
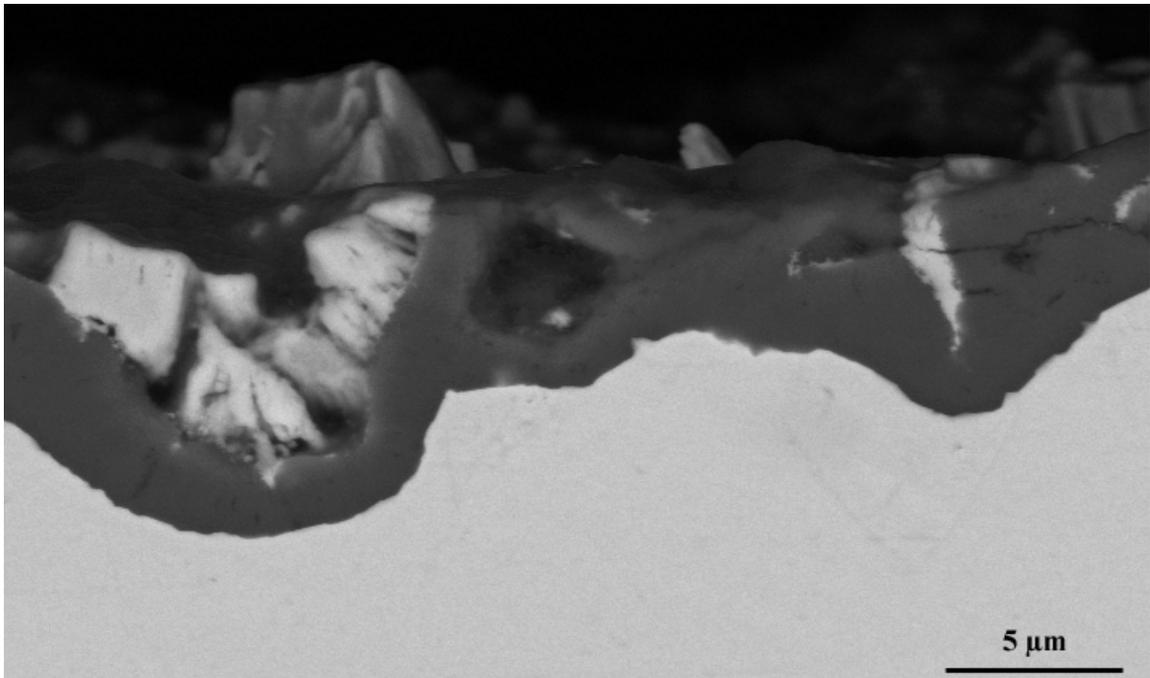
Figure 7.74 ME13 cross section shows YSZ debris remains attached to the TGO after failure. Note appearance of the TGO which is cracked laterally with heterogeneous thickness.
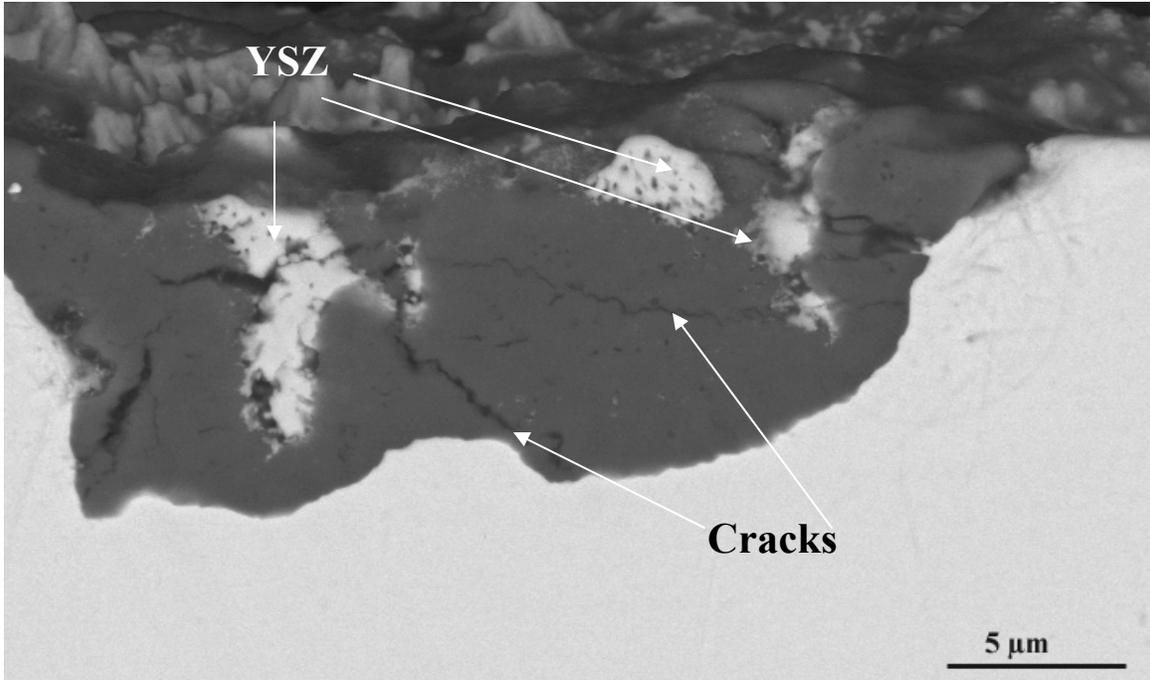
Figure 7.75 TGO on the ME13 shows cracks which appear to originate from the YSZ/TGO interface propagate.
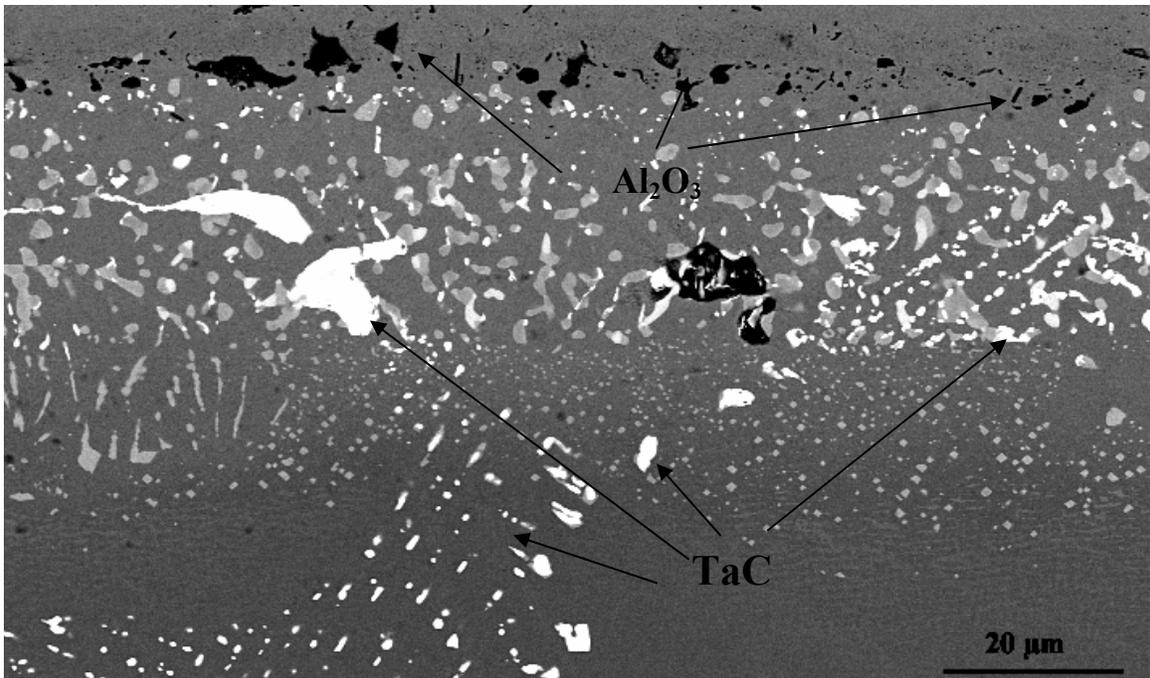
Figure 7.76 Interdiffusion are of a ME13 specimen after failure shows carbides and precipitates rich in Re, W, Cr, Co, and Ni.

7.4.2 Performance of CE6

CE6 failed along the YSZ/TGO interface at 65 cycles per specimen or 8% of N5s total average failure. The YSZ surface is seen in Figure 7.77, which shows again the numerous bits that remain attached to the YSZ TBC after failure of the TBC system. By taking a closer look in Figure 7.78, it is easy to see the holes created on the YSZ TBC after failure, along with the TGO bits which are larger than those on N5. The substrate surface on Figure 7.79 contains cracks, and YSZ bits, but not many holes are seen. Figure 7.80 also shows the amount of YSZ that remained on the TGO after failure of the TBC system.
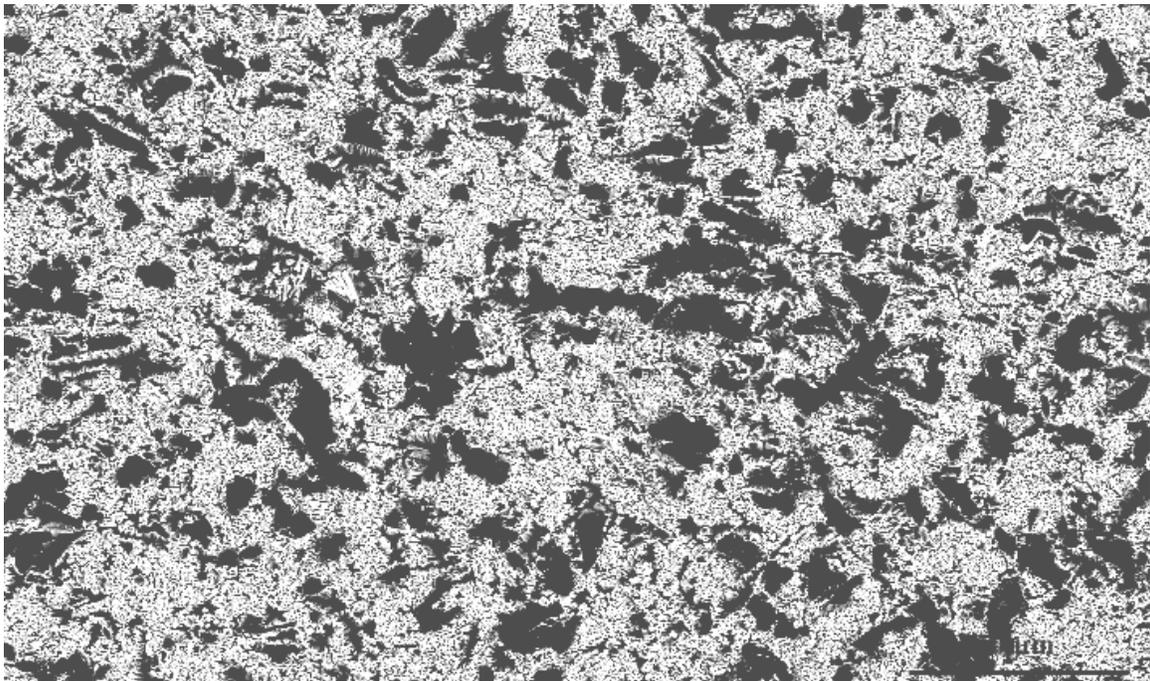
Figure 7.77 YSZ surface after failure of the the TBC system on a CE6 specimen.
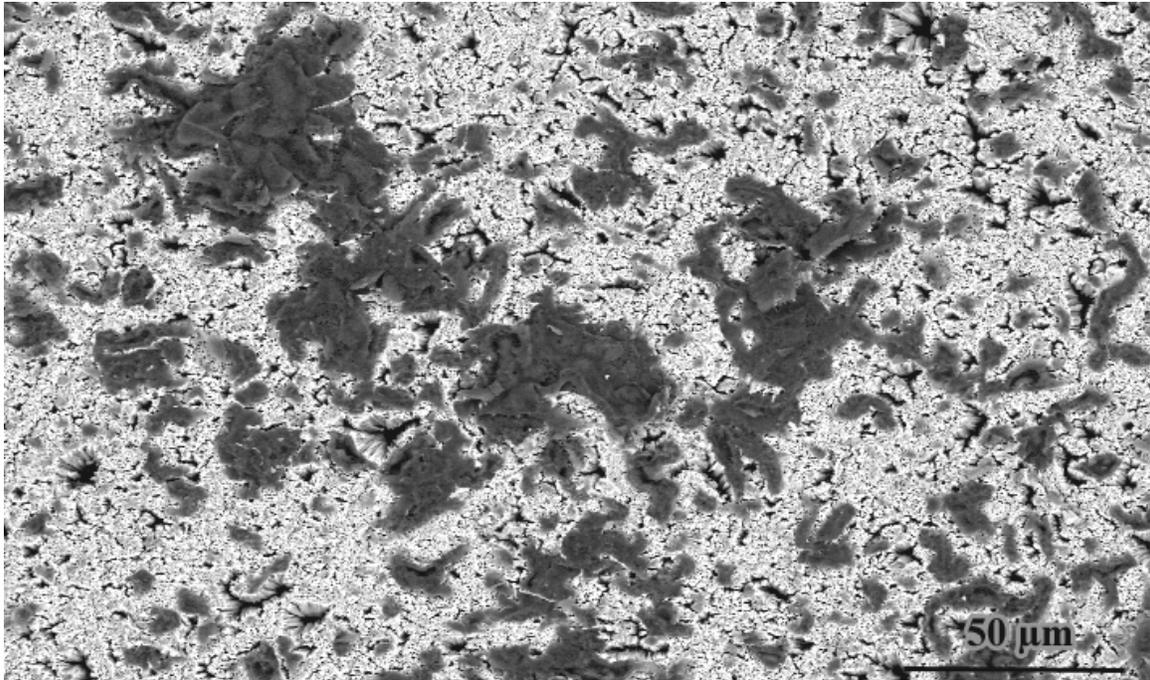
Figure 7.78 High magnification of the YSZ failure surface on a CE6 specimen shows holes on the YSZ and large scale TGO.
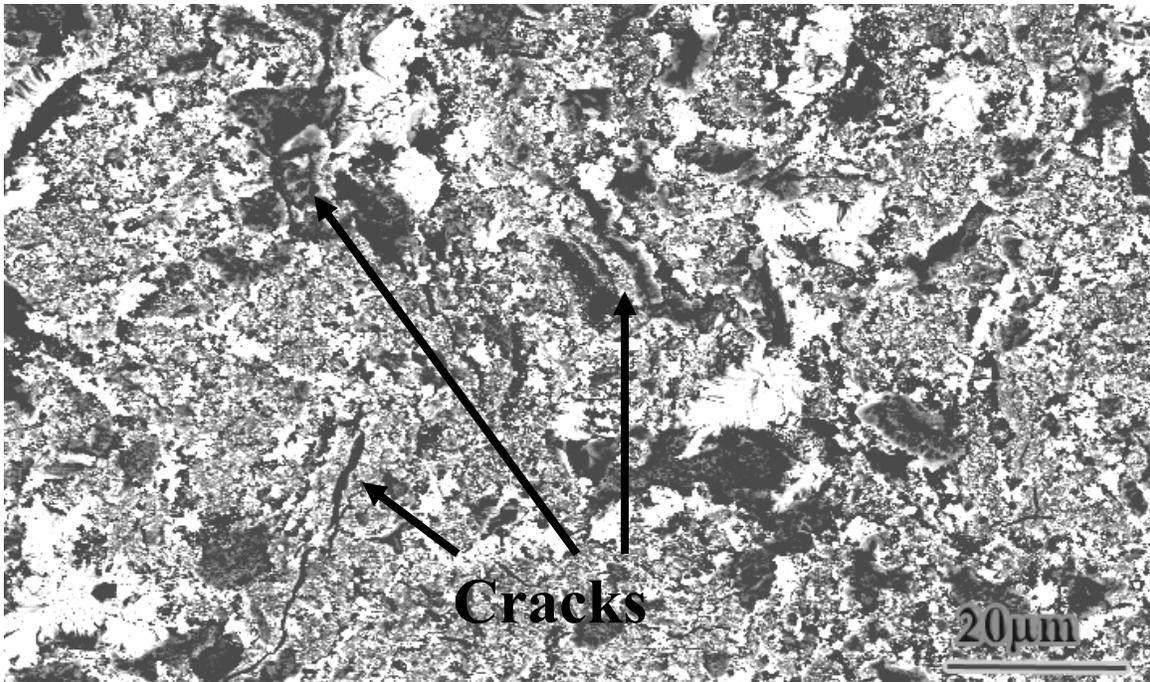
Figure 7.79 Substrate surface shows large amounts of YSZ on the TGO surface, also seen are numerous.
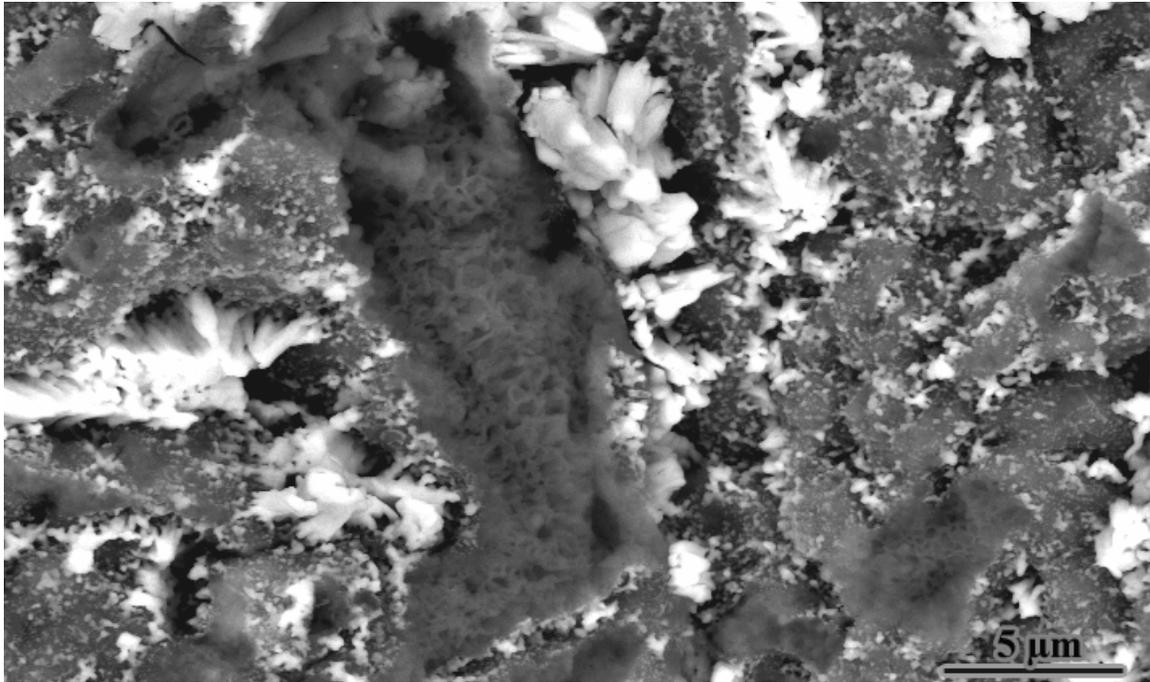
Figure 7.80 Substrate surface shows the TGO, and YSZ debris on the surface of a CE6 specimen.

The cross section of CE6 shows similar patterns to those of ME13, posing a large amount of precipitates, a relatively thin TGO, phase composition of the bond coat, and YSZ in the TGO, as well as ratcheting. Figure 7.81 shows the ratcheting effect expanding all along the YSZ/TGO interface. The thickness of the TGO, visible in Figure 7.82 has not exceeded 3 microns and yet contains remains of the YSZ inside. Figures 6.82 and 6.83 also elucidate on the bond coat phase, the bond coat has completely transformed to martensite, there is not any gamma prime. Other features from the cross section is the interdiffusion area. The interdiffusion area is not as thick as that of N5 and additionally forms tantalum carbides, already seen in ME13 and CE8. From Figure 7.84, it is possible to see the number of alumina particles above the interdiffusion area and a thin phase layer composed of gamma prime. Again, as for ME13, gamma prime does not form an interface with the TGO.
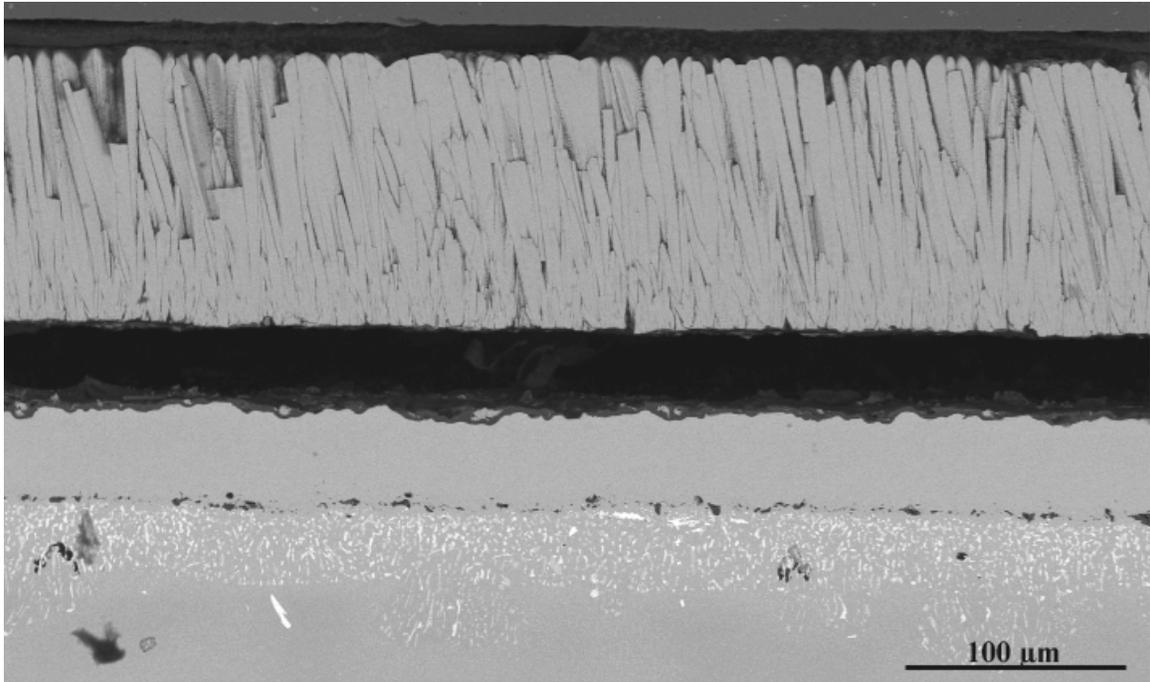
Figure 7.81 Cross sectional view of a CE6 substrate and its TBC system after failure.
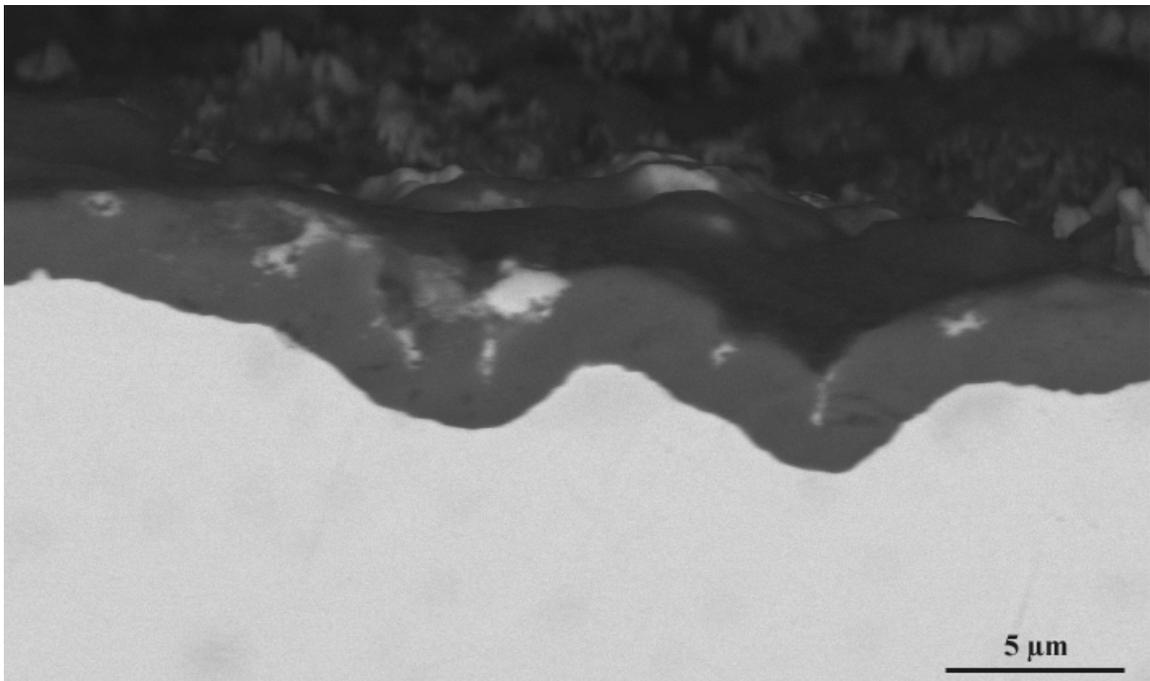
Figure 7.82 TGO thickness shows a relatively thin TGO and YSZ debris, note the homogeneous phase of the bond coat.
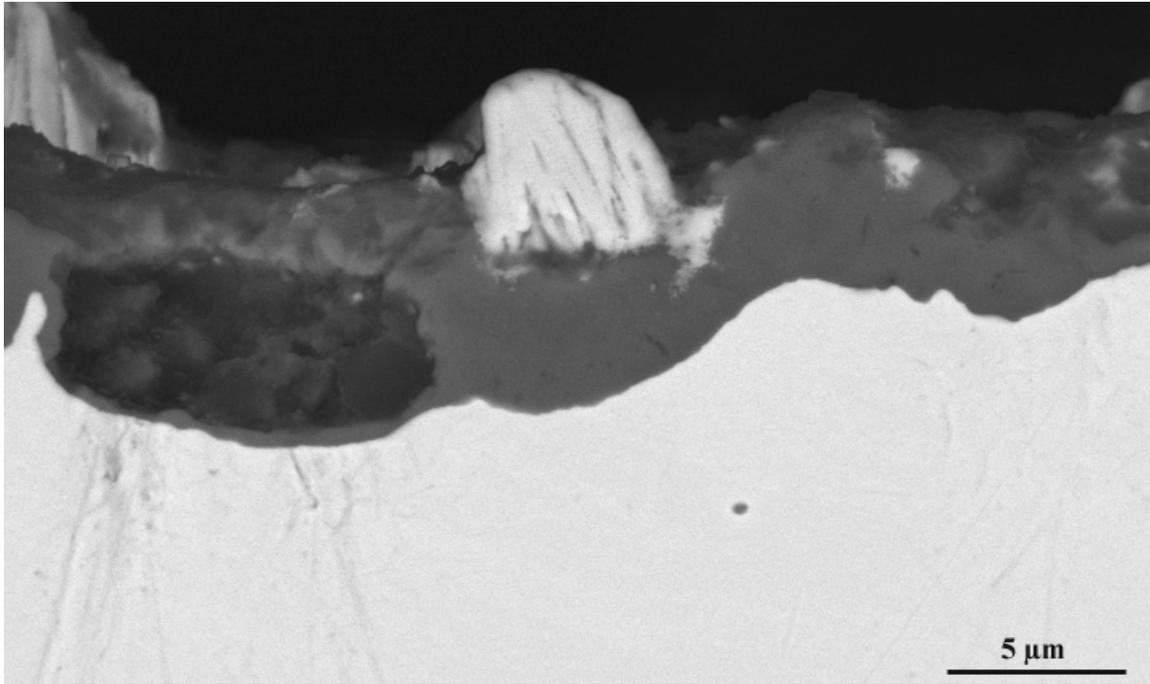
Figure 7.83 Bond coat on CE6 is homogeneous, while TGO shows expanded lateral cracks.
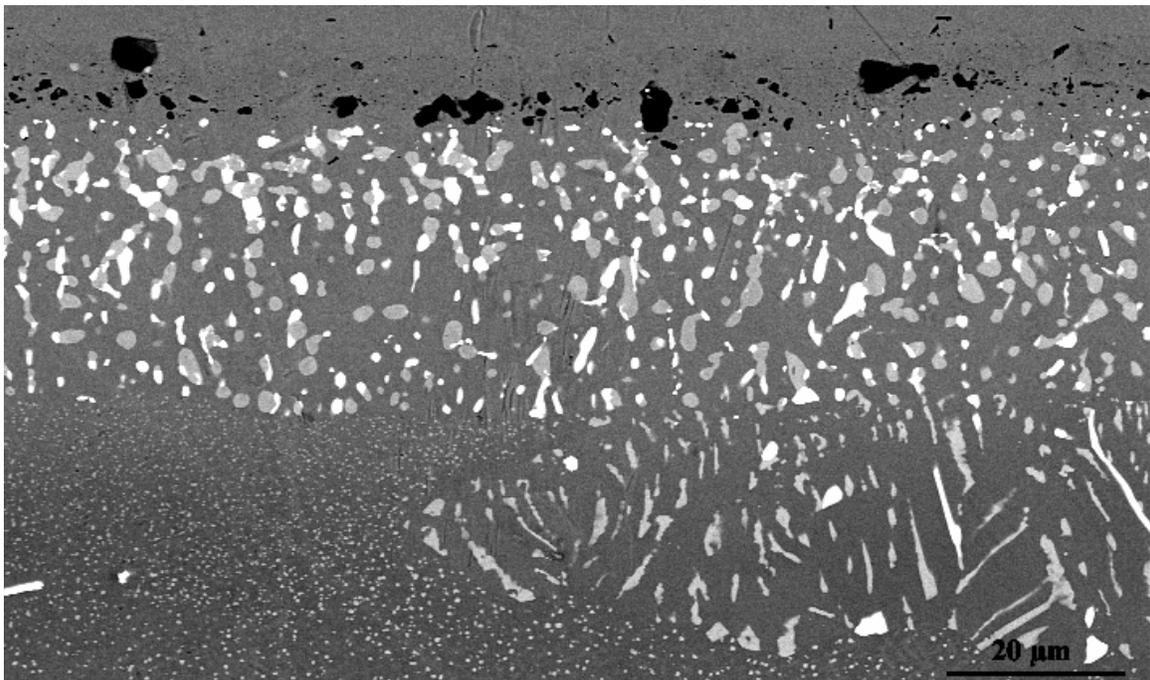
Figure 7.84 Interdiffusion area of a CE6 specimen shows numerous precipitates including the formation of carbides and other precipitates.

8.0 DISCUSSION

8.1 RATCHETING FAILURE

After examination of the specimens, it was concluded that all the specimens failed by ratcheting. During this deformation process, the bond coat surface is deformed by the compressive stresses produced by the coefficient of thermal expansion misfits between the TGO/bond coat and TGO/YSZ. The thermally grown oxide penetrates the bond coat while deforming it in an attempt to relax its stress level, and forms an axi-symmetric cone of extended oxide that expands and grows as the cyclic exposure continues. The formation of this undulation normally pushes downward on the bond coat at its center, while pushing upward at its ends, as mass from the bond coat gets distributed to the sides. See Figure 8.1, for a schematic of the evolution of the ratcheting effect. The mechanics easily create out of plane stresses that produce cracks capable of propagating with time along the TGO/YSZ interface, leading to failure. Nevertheless, additional factors exist along the YSZ/TGO interface that can influence the crack propagation rate.
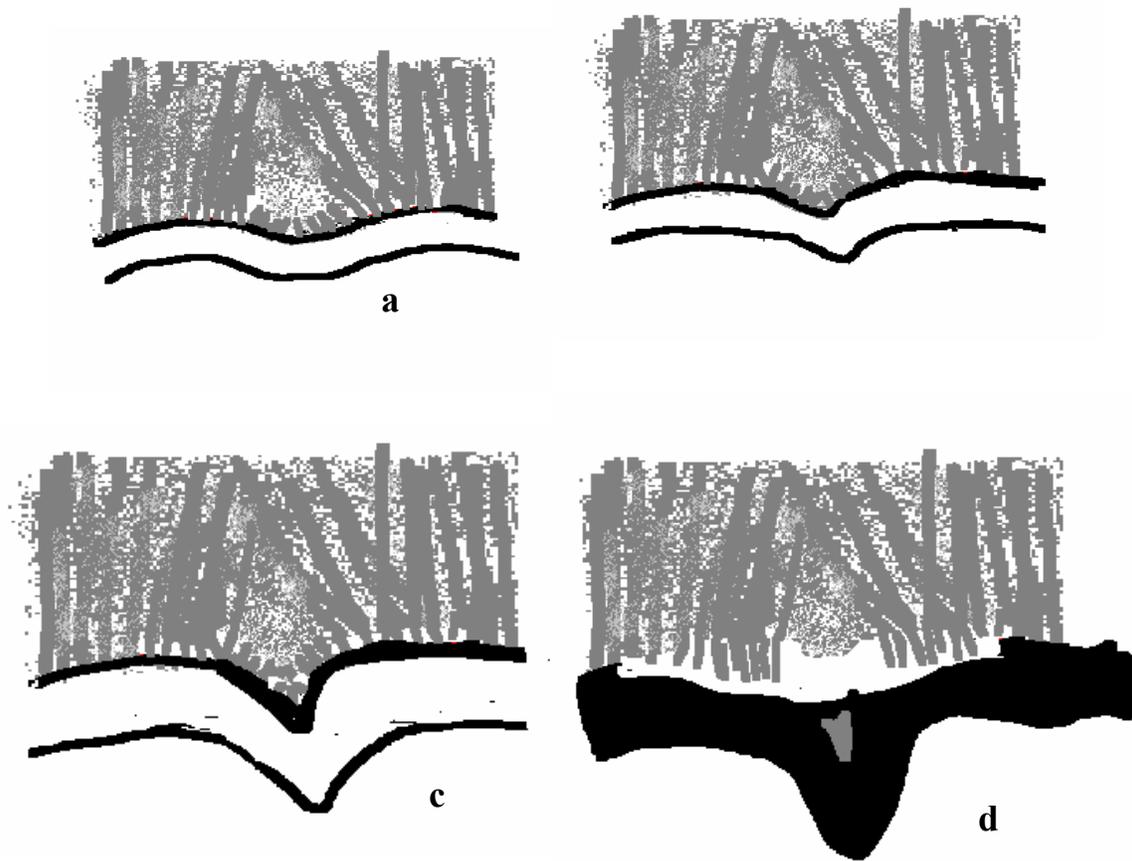
Figure 8.1 Evolution of the ratcheting effect: (a) Displays early deformation of the bond coat which deprives the YSZ grains from growing. (b) Deformation of the bond coat grows as the residual stresses appear compress the TGO. (c) Oxide scale deforms the bond coat and shapes undulation into a cone as the residual stresses continue to compress the TGO scale. (d) Thermally grown oxide detaches itself from the YSZ/TGO interface and a crack appears.

The TBC system experiences various forms of stresses mainly due to thermal misfits (residual stresses) and growth strains of the TGO. As the bond coat increases its cyclic life, there is a depletion of aluminum from the bond coat surface which triggers a phase transformation. As already seen in the figures presented in the results section, the classification of specimens is correlated to the phase transformations in the bond coats.

The high cyclic failure single crystal specimens displayed martensitic and gamma prime phases in the bond coat, the mid-range specimens displayed mostly martensitic and some gamma prime, while the low cycle failure specimens only displayed a martensitic transformation. It has been observed by Pan et al [7] that depletion of aluminum encourages the formation of a martensitic phase and eventually gamma prime. In his study on the mechanical properties of Pt modified NiAl bond coats, he noted that after 28% of the cyclic life of the bond coat had elapsed, the yield strength had increased from 300 to 500 MPa, when compared to the as received conditions at 600°C. Nevertheless, this yield strength decreased for temperatures greater than 800 °C, resembling the yield strength of β, the as received bond coat at such a temperature, a measurement of 25 MPa. It has been seen by Pan [7] and Karlsson [4] that the bond coat undergoes a transformation from martensitic ($L1_0$) to Beta (B2), and from B2 to martensitic after numerous cycles, having a transformation temperature between 600 and 800 °C. As mentioned earlier, Kainuma et al [6] found that the addition of alien elements to the bond coat lowers the martensitic transformation temperature, mainly by elements left to the group VIII in the table of elements and even more so by the heavier elements in these groups.

From this information by Pan [7] and Karlsson [4], it is suggested that most of the deformation of the bond coats takes place during high temperatures as the thermally grown oxide relaxes its compressive stresses. With cumulative cycles, the TGO extended into the bond coat deeper at elevated temperatures and deformed it until failure of the TBC system occurred. Such an effect is proven by observing cross sectional figures of the specimens. As the specimens decrease in cycles, it is possible to see a decrement in

the amount of segments where the oxide expands into the (Ni,Pt) Al bond coat. ME2 in

Figure 7.32, shows a high density of oxide areas, where the oxide extends into the bond

coat, while CE6 shows a highly deformed and undulated area. N5 in Figure 7.22 shows

a combination of deformation with segments of oxides extending into the bond coat.

8.2 FABRICATION EFFECT

Surface roughening appears to have a significant effect in the failure of these

specimens and it is believed to be the primary factor affecting the failure of these

specimens. Heavy grit blasting of the bond coat surface triggers a non-EB-PVD friendly

surface. As seen in Figure 7.7, numerous sub-micron holes exist for the as processed

condition, in addition to the amount of interfacial defects that are also found along the

YSZ/TGO interface. These holes are not expected to close or disappear during high

temperatures; on the contrary, it is assumed that such holes increase the creep rate.

Coalescence of these holes lead to large cracks and eventually spallation of the YSZ from

the TBC system. As seen through the spectrum of specimens studied, all specimens

failed along the YSZ/TGO interface, with the exception of the high cycle failure

specimens that showed some spallation of the TGO and reoxidation.

The sub-micron holes found along the YSZ/TGO interface represent just a small

part of the problem. There are other defects such as conical-shaped or pinched-off

segments in the YSZ, and stagnated growth columnar grains, as seen in Figures 6.7 and

6.8. These columnar grains shaped in the form of a cone are considered as traction-free

planes by Karlsson et al. [29]; hence, instabilities that lead to failure of the TBC system

and have no contact with the remaining YSZ. In the event of a thermal cycle that

oscillates continuously, it is assumed that the ratcheting mechanism draws these pinched

off areas of the YSZ inward as the TGO expands inward, creating a detached area or a

crack within the YSZ/TGO. This crack is able to propagate as the oxide deforms the

bond coat and further detachment between the YSZ and the TGO expands along the sub-

micron holes as they coalesce. Such loss to the infrastructure of the YSZ layer sends a

cataclysmic effect across the layer eventually creating a failure along the YSZ/TGO

interface.

8.3 SUBSTRATE EFFECT

With the failure of low cycle specimens, a handful of important aspects are

observed, i.e. several cracks that appear along the TGO of these specimens, as well as the

phase and composition of the bond coat. These cracks appear along the TGO/YSZ

interface along the TGO thickness, and can be responsible for the spallation of the TGO

and reoxidation of the bond coat as seen in high cycle specimens. It is possible that such

cracks propagate during thermal oscillation, as well as changing direction to interact with

other cracks, including those produced at the YSZ/TGO interface by ratcheting.

Additionally, these cracks may also be responsible for some of the wide gaps also seen in

the low and mid-range failure specimens. As seen in Figures 6.50 and 6.89, there seems

to be cracks forming which widened during thermal cycles, expanded and alumina

formed in them. This mechanism of cracks normal to the TGO thickness is an effect

produced by the growth strains. Nevertheless, the ratcheting/holes effect detailed in the previous section appears to have a larger effect in the failure of these TBC systems.

At 60 cycles per specimen, CE6 forms a TGO with a mean thickness of 3.5 μm, while N5 and ME2 at 800 and 765 cycles per specimen, respectively, form a TGO with a mean thickness of 5 μm. Hence a very thick TGO formed prior to the failure of low cycle failure specimens when compared to the high cycle failure specimens, indicative of a high oxidation growth rate constant. It is believed that this thermally grown oxide growth rate is affected by the active elements such as Cr and Ta.

IN738 shows traces of Ti, W, Cr, Co and though C is also a component of the substrate, no carbides were detected. Carbon segregates to the grain boundaries to strengthen the boundaries of the substrate at high temperatures and enhances the creep resistance of the alloy. For the rest of the specimens, it was a different story. Co and Cr were found in low cycle failure at a ratio of 2:1 respectively. Meanwhile, the high cycle failure specimens displayed a 1:1 ratio of these elements in the martensitic phase; when in the gamma prime phase, tantalum is added to create a Co:Cr:Ta ratio of the sort 5:4:3.

Platinum concentration across the specimens also depends on time exposure. It was seen that for high cycle failures, the amount of Pt was homogeneous throughout the cross section. On the other hand, the Pt concentration for lower cycle failures showed that most of the Pt was still at the bond coat, with very little inward diffusion towards the substrate. Hence, the diffusion of Pt to the substrate of low cycle failures was countered by the cycle time. Other elements such as Re, Hf, and W, were not found to influence the bond coat at all. Re and W along with Cr formed precipitates at the bond coat/substrate interdiffusion area that would not disperse regardless of the time seen in the specimens.

The content of Hf is not expected to have affected any of the high or mid range cycles and was found to also spread homogeneously across the cross section of the substrate. Nevertheless, Hf is expected to have formed HfC in CE8, and ME13 hence allowing some Ta to free itself and diffuse to the bond coat where it segregated at the TGO/ bond coat interface to the gamma prime phase. From Figure 8.2, it is possible to see the Gibbs free energy of formation of carbides for the refractory elements. CE6 specimens and IN738 do not contain any Hf.
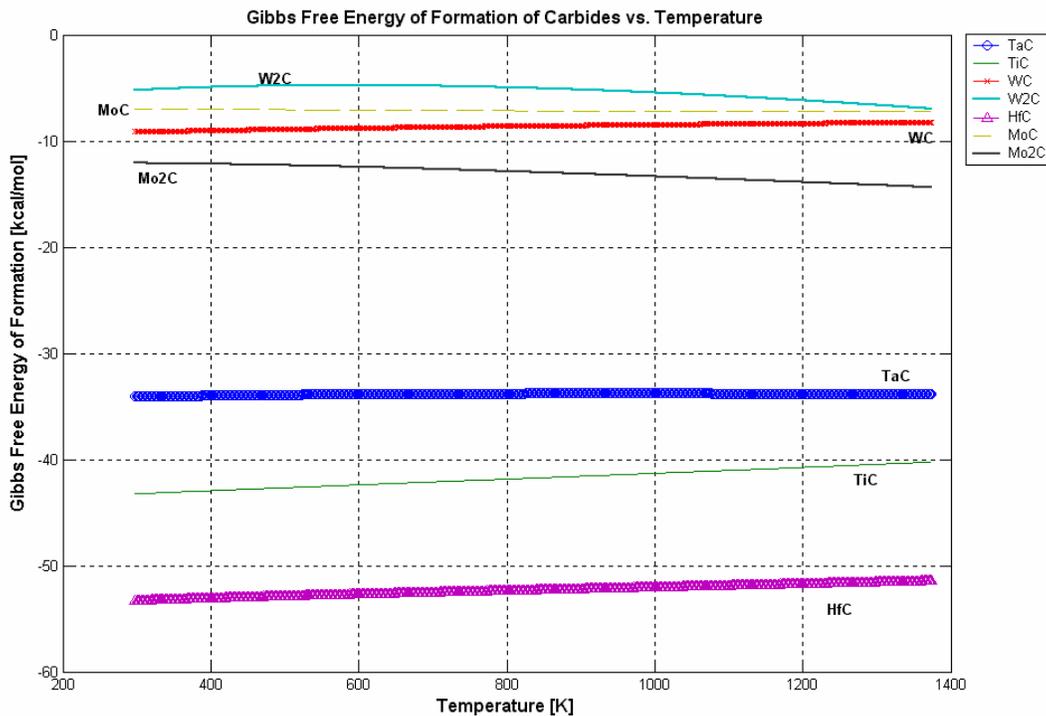
Figure 8.2 Gibbs Free Energy carbide curves for different refractory metals.

Diffusion of active elements in and from the bond coat can occur by both inward and outward diffusion through grain boundaries. Aluminum is depleted by selective oxidation and inward diffusion. Both adherence and growth rate are affected by substrate

elements. Tantalum traces are found in very minute amounts in the low cycle failures and found in higher failure specimens in greater amounts. The lack of tantalum in the bond coat of lower failure specimens is due to the formation of tantalum carbides at the interdiffusion area; hence, the entrapment of tantalum does not allow it to diffuse out to the bond coat. A special case is seen in CE8, for which case there is a similar amount of tantalum and carbon as seen in the LCF substrate compositions, nevertheless it also contains 0.14 wt% Hf, which forms a more stable carbide than tantalum. As a result, more tantalum is found in the bond coat cross secion of CE8, as well as a longer life time. Meanwhile, for higher failure specimens that do not contain carbon, tantalum is found at the bond coat and TGO/bond coat interface in high traces. Tantalum as it is known can substitute for aluminum in the $L1_2$ structure, and was found in high concentrations to segregate to those particular phases in the bond coats of high and mid range failures. Additionally, tantalum has been known to improve the adhesion of the protective layer. Moreover, it has been researched that certain elements such as Ta can lower the transformation temperature when present in NiAl alloys [6]. Chromium presence in the bond coat can be good news to the healing of the Al_2O_3 protective layer. As it is known, Cr is an oxygen getter, indicating that for conditions with low Al < 5%, Cr can become a aid to the formation of Al_2O_3.

9.0   CONCLUSIONS

- All specimens failed by ratcheting.

- A heavily grit blasted beta (Ni,Pt)Al bond coat was used in the thermal barrier coating system of the study and produced shorter lives of thermal barrier coating systems.

- Bond coat surface appears to be a primary factor that affects the cyclic life of the specimens. Substrate composition seems to be a secondary factor affecting the cyclic life of the TBC system.

- Numerous defects seen in the as-processed condition are accountable for the failure of the TBC system at such an early time, these include small holes produced by the deposition of YSZ TBC on the rough surface of the (Ni,Pt) Al bond coat. Other defects that also aided in creating a weak YSZ/TGO interface are the YSZ TBC stagnated growth grains. Short cyclic life specimens distinguished themselves by presenting a very porous YSZ/TGO interface.

- It is suggested that deformation of the bond coat occurred at elevated temperatures, while spallation of the YSZ from the TGO interface occurred at room temperature.

- Martensite as well as gamma prime phases were observed at room temperature for both high and mid range specimens with the exception of IN738, which formed

- gamma and gamma prime. CE6 specimens did not show a transformation of the bond coat to gamma prime.

- Refractory metals such as W, Re, Hf did not diffuse into the bond coat. These elements formed precipitates at the substrate/bond coat interdiffusion area.

- IN738 contained Ti, Cr, Co, and W at the bond coat; it did not form carbides.

- Single crystals without carbon outperformed single crystals with carbon.

- More studies of these TBC systems with smoother bond coat surfaces need to be conducted in order to observe whether substrate composition has a larger effect on the thermal barrier coating system.

REFERENCES

1. Bungardt, K., Lehnert, G., Meinhardt, H.W., "Protective Diffusion Layer on Nickel and/or Cobalt-Based Alloys", US Patent No. 3819338, 1974.

2. Zhang, Y., Haynes, J.A., Pint, B.A., Wright, I.G., Lee, W.Y., "Martensitic Transformation in CVD NiAl and (Ni,Pt)Al Bond Coatings", Surface and Coatings Technology, 2003, v.163-164, pp.19-24.

3. Chen, M.W., Glynn, M.L., Ott, R.T., Hufnagel, T.C., Hemker, K.J., "Characterization and modeling of a Martensitic Transformation in a Platinum Modified Diffusion Aluminide Bond Coat for Thermal Barrier Coatings", Acta Materialia, 2003, v.51, pp. 4279-4294.

4. Karlsson, A.M., "On the Mechanical Response in a Thermal Barrier System Due to Martensitic Phase Transformation in the Bond Coat", 2003, Transactions of the ASME, vol. 125, pp. 346-352.

5. Purvis, Andrew L., Warnes, B.M., "The Effects of Platinum Concentration on the Oxidation Resistance of Superalloys Coated with Single Phase Platinum Aluminide", Surface and Coatings Technology, 2001, v.146-147, pp.1-6.

6. Kainuma, R., Ohtani, H., Ishida, K., "Effect of Alloying Elements on Martensitic Transformation in the Binary NiAl(β) Phase Alloys", 1996, Metallurgical and Materials Transactions A, vol. 27A, pp.2445-2453.

7. Pan, D., Chen, M.W., Wright, P.K., Hemker, K.J., " Evolution of a Diffusion Aluminide Bond Coat for Thermal Barrier Coatings During Thermal Cycling", Acta Materialia, (2003), v. 51, pp. 2205-2217.

8. Evans, A.G., Mumm, D. R., Hutchinson, J. W., Meier, G. H., Pettit, F. S., " Mechanisms Controlling the Durability of Thermal Barrier Coatings", Progress in Material Science, (2001), v. 46, pp. 505-553

9. Warnes, M.B., Punola, D.C., "Clean Diffusion Coatings by Chemical Vapor Deposition", 1997, Surface and Coatings Technology, v. 94-95, pp. 1-6.

10. Haynes, A.J., "Potential Influences of Bond Coat Impurities and Void Growth on Premature Failure of EB-PVD TBCs", 2001, Scripta Materialia, v. 44, pp.1147-1152.

11. Vaidyanathan, K, Gell, M., and Jordan, E., "Mechanisms of Spallation of Electron Beam Physical Vapor Deposited Thermal Barrier Coatings With and Without Platinum Aluminide Bond Coat Ridges", Surface and Coatings Technology, 2000, v. 133-134, pp.28-34.

12. Sims, C.T, Stoloff, N.S., Hagel, W.C., Superalloys II, Wiley Interscience, New York, pp.12.

13. Wright, P.K., Evans, A.G., "Mechanisms Governing the Performance of Thermal Barrier Coatings", Current Opinion in Solid State and Material Science, (1999), v.4, pp.255-265.

14. Johnson, C.A., Ruud, J.A., Bruce, R., Wortman, D., "Relationships Between Residual Stress, Microstructure and Mechanical Properties of Electron Beam-Physical Vapor Deposition Thermal Barrier Coatings", Surface and Coatings Technology, 1998, v. 108-109, pp.80-85.

15. Xu, T., He, M.Y., Evans, A.G., "A Numerical Assessment of the Durability of Thermal Barrier Systems that Fail by Ratcheting of the Thermally Grown Oxide", Acta Materialia, (2003), v. 51, pp. 3807-3820

16. Sarioglu, C., Blachere, J.R., Pettit, F.S., Meier, G.H., Microscopy of Oxidation, v. 3, pp. 41-50

17. Pint, B.A., Wright, I.G., Lee, W.Y., Zhang, Y., Prüßner, K., Alexander, K.B., "Substrate and Bond Coat Compositions: Factors Affecting Alumina Scale Adhesion", Material Science and Engineering A, (1998), v. 245A, pp. 201-211.

18. Christensen, R.J., Tolpygo, V.K, and Clarke, D.R., "The Influence of the Reactive Element, Yttrium on the Stress in Alumina Scales Formed by Oxidation", Acta Materialia, (1997), v. 45, pp.1761-1766.

19. Pettit, F. S., Meier, G. H., "The Effects of Refractory Elements on the High Temperature Oxidation and Hot Corrosion of Superalloys", Refractory Alloying Elements in Superalloys, in J. K. Tien and S. Reichman (eds.) ASM, Metals Park, OH, (1984), p.165.

20. Miller, R. A., " Thermal Barrier Coatings for Aircraft Engines—History and Directions", (1995), NASA Conference Publication 3312, pp.17-34.

21. Strangman, T.E., "Thermal Barrier Coatings for Turbine Airfoils", Thin Solid Films, (1985), v.127, pp93-105.

22. Bartuli, C., Bertamini, L., Matera, S., Sturlese, S., " Investigation of the Formation of an Amorphous Film at the ZrO2-Y2O3/NiCoCrAlY Interface of Thermal Barrier Coatings Produced by Plasma Spraying", Materials Science and Engineering A, (1995), v. 199A, pp. 229-237.

23. Guessasma, S., Ghislain, Montavon, Coddet, C., " Modelling of the APS Plasma Spray Process Using Artificail Neural Networks: Basis, Requirements and an Example", Computational Material Science, (2004), v. 29, pp. 315-333

24. Schlichting, K.W., Padture, N.P., Jordan, E.H., Gell, M., "Failure Modes in Plasma Sprayed Thermal Barrier Coatings", Materials Science and Engineering A, (2003), v. A342, pp.120-130.

25. Straffor, K.N., Datta, P.K., and Googan, C., "Coatings and Surface Treatment for Corrosion and Wear Resistance", (1984), 1st Ed., pp. 187-189

26. Schulz, U., Schmücker, M., "Microstructure of ZrO2 Thermal Barrier Coatings Applied by EB-PVD", Material Science and Engineering A, (2000), v. A276, pp.1-8.

27. Tin, S., Pollock, T.M., King, W.T., " Carbon Additions and Grain Defect Formation in High Refractory Nickel Base Single Crystal Superalloys", Superalloys 2000, (2000), pp. 201-210.

28. Mumm, D.R., Evans, A.G., Spitsberg, I.T., "Characterization of a Cyclic Displacement Instability for a Thermally Grown Oxide in a Thermal Barrier System", Acta Materialia, (2001), v.49, pp. 2329-2340.

29. Karlsson, A.M., Xu, T., Evans, A.G., "The Effect of the Thermal Barrier Coating on the Displacement Instability in Thermal Barrier Systems", Acta Materialia, (2002), v.50, pp. 1211-1218.